7. Element Mapping & Staining Experiments

It has been shown in the previous chapter, that image processing procedures like color mapping, can dramatically improve the information content of the TEM images. However, when it comes to the analysis of the polymer electrolyte distribution inside the catalyst agglomerates or if the pore system is infiltrated by the embedding resin, this approach gives only limited information. In case, the pore system is infiltrated by the embedding resin, any information about the pore structure or the polymer electrolyte distribution is lost due to the highly similar scattering properties of the embedding resin and the electrolyte. Further, since the sample is viewed in transmission, the polymer electrolyte can only be identified in regions where it is the only component in the electron beam. Therefore, no information about the state of the polymer electrolyte in the interior of the agglomerates, where the polymer electrolyte overlaps with the catalyst particles, can be obtained by standard TEM bright field imaging.

However, in order to understand the transport processes in the electrode in detail, in particular those of protons and water, it is of fundamental importance, whether the polymer electrolyte can contact also internal catalyst sites inside the agglomerates.

To address these problems two approaches were evaluated:

- Contrast enhancement by selective staining of the polymer electrolyte with heavy metal salts.
- Mapping of the fluorine distribution using energy filtering.

7.1. Staining

The polymer electrolyte in a fuel cell is exposed to rather harsh chemical and electrochemical conditions. Therefore, the polymer backbone of the polymer electrolyte must possess a high chemical stability, i.e. it must have a low reactivity. This property is highly unfavorable for the incorporation of staining agents

into the polymer backbone itself. But staining can be realized via the ionic groups of the polymer electrolyte. The protonized form of the polymer electrolyte can be easily transferred to an ion exchanged form by exposing it to a solution containing a metal salt. It has been shown in literature that a wide variety of metal salts and even rather bulky organic cations like tetrabutyl ammonium (TBA^+) can be incorporated into PFSI polymer electrolytes [69,133], but other types of polymer electrolytes should behave similarly and therefore, this approach can be considered as a rather general approach, independent of the used polymer electrolyte.

In order to obtain a strong increase of scattering contrast, the metal ion used as staining agent should have a high electron density. Since the metal ion acts as a counter ion to the sulfonic groups, it should further be of low charge to introduce a large number of additional scattering centers. In the background of these considerations cesium appeared as an appropriate staining agent, as it possesses a high electron density and low charge. Further, the use of cesium had also been reported in the literature for marking the sulfonic clusters in Nafion membranes for examination with transmission electron microscopy [133].

7.1.1. Experimental

Thin-sections stained with heavy metal salts were obtained by placing the ultramicrotomed sections on a drop of water for about 30 minutes. Thereafter, the sections were removed and rinsed by dipping them several times into a drop of deionized water.

Two sets of samples were prepared, one stained with Cs^+ using a CsOH solution and another in which $Ba(OH)_2$ was used as staining agent.

7.1.2. Cesium (Cs^+) Staining

Figure 7.1 displays TEM bright field images of an unstained and Cs^+ stained MEA in comparison. Both images were taken at the interface between the membrane and the electrode, with the membrane being located at the right hand side of the images. A clear effect of the staining can be seen for the membrane of the cesium treated sample (bottom image). The membrane of this sample appears to

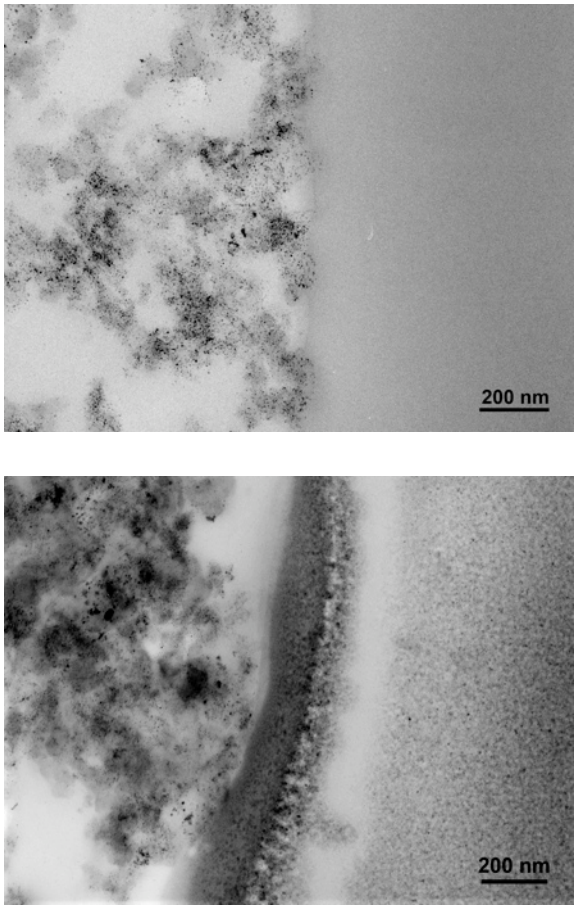

Figure 7.1. *TEM micrographs of the membrane electrode interface for an unstained sample (top) and a sample stained with Cs^+ (bottom).*

be speckled and stripes of more or less strongly contrasted regions can be seen close to the interface with the electrode. While less strong than for the membrane, also a darkening of the electrode can be observed. The staining of the electrode layer is most pronounced around the catalyst support particles suggesting that the Nafion ionomer is covering the catalyst support particles, but is not flooding large pores.

The differently contrasted regions in the membrane close to the membrane-electrode interface are most likely an artifact of the staining process and not a part of the inherent structure of the membrane. They are most probably caused

by dissolution and redistribution of the staining agent due to swelling of the membrane. When immersed into the staining solution, the membrane starts to swell due to the uptake of water in its hydrophilic clusters. Since the membrane is constrained by the embedding resin, it will distort to accommodate for its increased lateral dimensions. This distortion may then lead to contrast changes as observed in Figure 7.1 (bottom), by inhomogeneous drying and redistribution of the staining agent.

However, a different interpretation is possible, too. If not interpreted as an artifact, Figure 7.1 (bottom) suggests an enrichment of sulfonate groups at the membrane electrode interface. Such an enrichment might be caused by the membrane pretreatment process in H_2O_2 and H_2SO_4, which has been reported to cause changes of the sulfonate group concentration at the membrane surface [144]. Nevertheless, it appears unlikely that the pretreatment process effects such a large interface zone as shown in Figure 7.1 (right).

7.1.3. Barium (Ba^{2+}) Staining

The experiments with Cs^+ staining showed, that if heavy metal ions are used as staining agents to contrast the polymer electrolyte, one has to be aware of staining artifacts. These staining artifacts may be reduced by rinsing the specimen more thoroughly after the staining process. However, it was found that prolonged rinsing of the specimen significantly reduced the contrast improvement obtained by the staining, indicating that the cesium ions got washed out of the sample. Therefore, in order to reduce staining artifacts, it was tried to replace cesium by an ion being less likely to be washed out, i.e. one that binds more strongly to the sulfonate groups of the polymer electrolyte.

Since divalent ions attach more strongly to sulfonate groups, Barium was chosen as a possible candidate, due to its higher charge, which should provide a stronger coupling to the sulfonate groups of the Nafion. The barium staining was found to be more persistent to rinsing. Therefore, it was possible to stain the sample prior to the embedding process without draining the stain from the sample into the water trough of the diamond knife after sectioning (see chapter 3.5.3 for more details on the sectioning process).

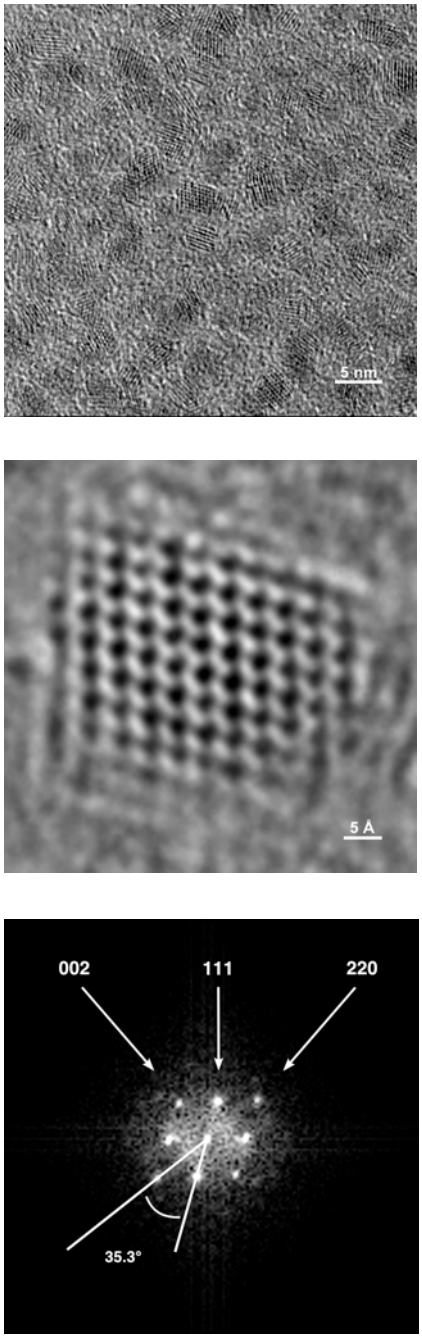

Figure 7.2. *High resolution TEM micrograph of the Nafion membrane stained with BaOH showing crystalline precipitates (top). Magnified and Fourier filtered image of a crystalline BaF_2 particle in the membrane (center). Fourier transform of the particle shown in the central image (bottom).*

Table 7.1. *Structural data of the BaF_2 crystals determined from the Fourier transform shown in Figure 7.2 (bottom).*

	Value from FFT	Tabulated values for BaF_2
d(111) / Å	3.56	3.58
d(220) / Å	3.07	3.09
d(200) / Å	2.23	2.19
∢(111)/(220)	35.3°	35.3°

Prestaining with Ba^{2+} significantly reduced artifacts and staining was found to be fairly more uniform than with Cs^{+}. However, the contrast improvement was weaker due to the higher charge of the barium ion (Ba^{2+}), which causes only half the amount of heavy metal ions to be incorporated into the polymer electrolyte, when compared to cesium.

A clear effect of staining was only observed for the membrane. At lower magnification the membrane appeared to be speckled, which turned out to be due to small nanometer sized crystals in the membrane (Figure 7.2 top). High resolution imaging (Fig. 7.2 center) combined with Fourier analysis (Figure 7.2 bottom) of the lattice fringes indicated that these crystals are BaF_2. (For a comparison of the structural data obtained by Fourier transformation and tabulated values for BaF_2, see Table 7.1).

Due to the instability of the sulfonic groups and fluorinated polymer backbone of Nafion towards ionizing radiation [144], it is most likely that the BaF_2 crystals form under the influence of the electron beam. Barium ions which are released from destroyed sulfonic groups may react with fluorine, as the side chains and the polymer backbone degrade in the electron beam. Although the size of the crystals fits well with the dimensions reported for ionic clusters in dried Nafion, the contrast caused by the BaF_2 crystals should not be confused with the structure of the sulfonic cluster network in the membrane. A simple calculation based on the size of the barium fluoride crystals shows that the average number of barium atoms contributing to the formation of a single BaF_2 crystal is significantly larger than the average number of sulfonate side chains reported for the

ionic clusters in Nafion. The mean barium fluoride cluster size determined from Figure 7.2 is about 2.9 nm. Assuming spherical symmetry for the barium fluoride clusters the average number of barium atoms in each cluster is about 215. As each side chain in Nafion contains only one sulfonate group and one barium ion bonds to two sulfonate groups for reasons of charge balance, the average number of side chains that contribute to the formation of the barium fluoride clusters is about 430. According to the results of Gierke et al., based on their cluster-network model of Nafion, the number of sulfonate groups per ionic cluster is about 27 for a completely dried sample [44]. This means that on average at least 16 ionic clusters contribute to the formation of one barium fluoride cluster. While this result is certainly a rough approximation, since it is based on several simplifications regarding the structure of Nafion and the structure of the barium fluoride crystals, it demonstrates, that significant structural rearrangement has to take place when the sample is exposed to the electron beam.

7.1.4. Phospho-Tungstic-Acid (PTA) Staining

Phospho-tungstic-acid (PTA) is frequently used to obtain a negative staining contrast for weakly scattering samples such as viruses, proteins or polymers. When dried, PTA forms an amorphous film with crystallite sizes below 1 nm and hence does not cause artifacts due to crystallization or diffraction. It is usually applied to the specimen deposited on a thin amorphous carbon film. The topography of the deposited sample causes the stain to distribute inhomogeneously on the carbon film, resulting in a negative imprint of the objects to be studied.

In contrast to the heavy metal salts used to stain the sulfonic clusters in the polymer electrolyte, PTA is an anionic stain. The anion of phospho-tungstic-acid is a rather bulky ion containing 12 tungsten and 40 oxygen atoms and a phosphorous atom in its center. Due to its negative charge it cannot act as a counter ion to the sulfonate groups of the polymer electrolyte, unlike the cationic stains described before.

The principal idea of using PTA as a stain for PEFC electrodes was to create a coating layer of high scattering contrast on the pore walls of the electrode to aid identification of the interface between the embedding resin and the polymer electrolyte.

Experimental

In order to obtain PTA contrasted samples, pieces of the MEA were immersed into an aqueous solution of PTA. Thereafter, the samples were dried, embedded in epoxy resin and sectioned using an ultra-microtome equipped with a diamond knife.

Results

Contrasting with PTA resulted in a considerable improvement of overall contrast of the sample (Fig. 7.3), indicating that PTA in fact forms a thin coating on the pore walls. The coating appears to be rather thin, as no clear interfaces between the sample and the PTA layer can be observed. Nevertheless, even pores in the electrolyte smaller than the section thickness, which were hardly visible in the unstained samples without image processing, can be identified more clearly.

Staining with PTA also revealed internal pore structures in larger extended polymer electrolyte regions as displayed in Figure 7.4, yielding another evidence that the polymer electrolyte distribution cannot be described by a simple pore filling or coating mechanism.

The PTA staining also confirmed the complex film like structure of the Nafion cast into the pore space between the catalyst agglomerates. Figure 7.5 shows an image of a pore, where up to 3 layers of Nafion films can be seen overlapping with each other. Considering that the average specimen thickness is less than 100 nm, this signifies, that the Nafion films found in the electrodes have thicknesses of less than 30 nm, despite their sometimes larger lateral expansion in the image plane.

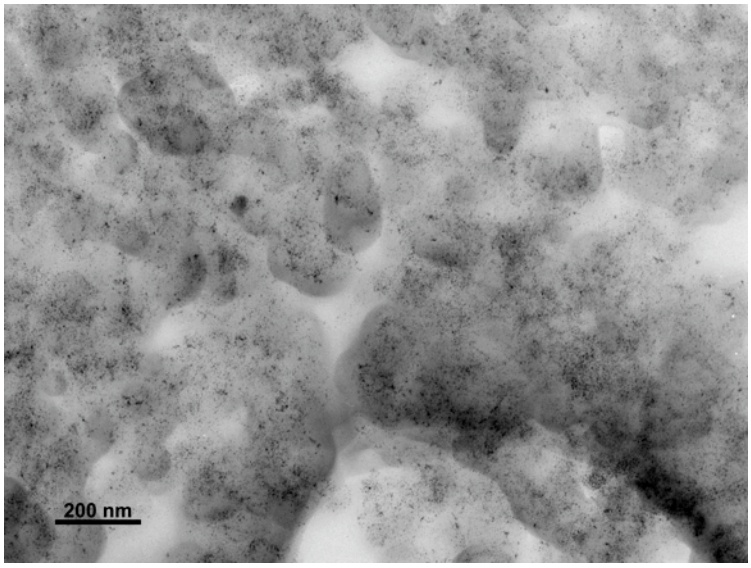

Figure 7.3. *TEM micrograph of an electrode demonstrating the contrast enhancing effect of negative electrode staining using PTA.*

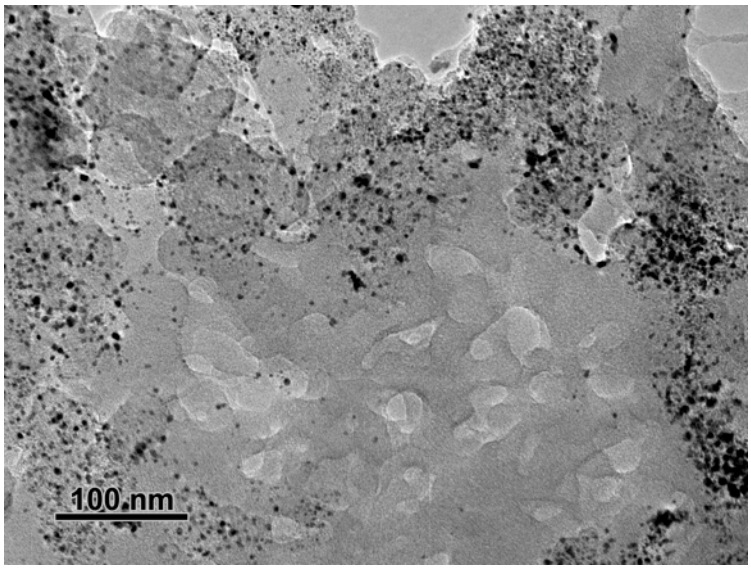

Figure 7.4. *TEM micrograph of an electrode stained with PTA showing pores in the polymer electrolyte.*

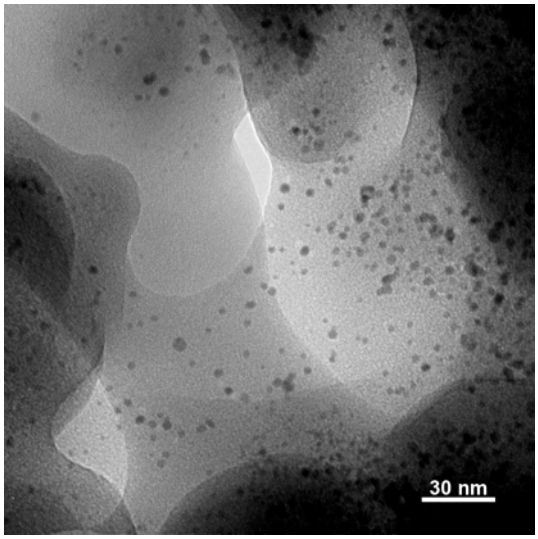

Figure 7.5. *TEM micrograph of thin Nafion structures inside a pore.*

7.2. Element Mapping

While staining improved the overall contrast of the sample, aiding the identification of structural details such as pores smaller than the section thickness, contrast enhancements were either too weak or prone to artifacts to obtain reliable information about the polymer electrolyte distribution inside the catalyst agglomerates.

Element mapping techniques are an elegant alternative to staining experiments, as they do not require the insertion of a staining agent and are therefore less prone to artifacts. Instead, differences in the chemical composition can be used to distinguish the polymer electrolyte from the resin. Therefore, element mapping adds additional information based on the chemical composition rather than the scattering of the sample, which should also allow identification of the polymer electrolyte at locations where it could otherwise not be distinguished from the catalyst agglomerates.

For PFSI polymer electrolytes, which are most commonly used in PEMFCs and DMFCs, the fluorine signal can be used to visualize the electrolyte distribution. The sulfur signal, which arises from the sulfonate groups, is less suitable for element mapping as the sulfur concentration is significantly lower than that of fluo-

rine. In addition, an overlap of the sulfur signal with the platinum $M_{\alpha 1}$ emission [145] as well as sulfur impurities in the carbon support may lead to miss-quantification of the polymer electrolyte distribution.

In the TEM elemental information can either be obtained by energy dispersive X-ray (EDX) mapping or energy filtered imaging (EFI). For the analysis of the fluorine distribution EFI was chosen due to its higher sensitivity for light elements and shorter acquisition times due to a parallel instead of serial recording of the elemental information in case of EDX mapping. Both issues should result in reduced beam damage of the sample and therefore result in more reliable information.

Elemental information can be obtained from energy filtered image data either by the so-called three- or the two-window-method [62]. In this work, the three-window-method was used, which was described in more detail in chapter 6. In short, for this method three energy filtered images are acquired. One at an energy corresponding to the characteristic loss feature of the element investigated (post-edge image) and two at energy losses slightly lower than the characteristic energy loss feature (pre-edge images). The latter images are used to construct a background image, which is subtracted from the post-edge image to obtain the elemental distribution.

Figure 7.6 a shows a part of an electrode structure prepared with a high polymer electrolyte content (60 vol. %, see also chapter 6.3.1). The image was obtained by the assembly of a 3 x 3 image series acquired with the software routine described in chapter 6. Catalyst agglomerates close to two larger pores separated by a string of Nafion are visible in the image. Comparison with the fluorine map (Fig. 7.6 b), shows that the polymer electrolyte is far more extended, covering also parts of the catalyst agglomerates, which was not visible in the unfiltered image.

A superposition of the fluorine map with the unfiltered TEM image is shown in Figure 7.6 c to aid the correlation of the fluorine, i.e. Nafion distribution, with the agglomerate structure of the electrode. A high polymer electrolyte concentration is found mainly in the boundary region between agglomerates. The walls of the large pores, which expose the most pronounced polymer electrolyte features in the unfiltered image, apparently do not contain the highest polymer

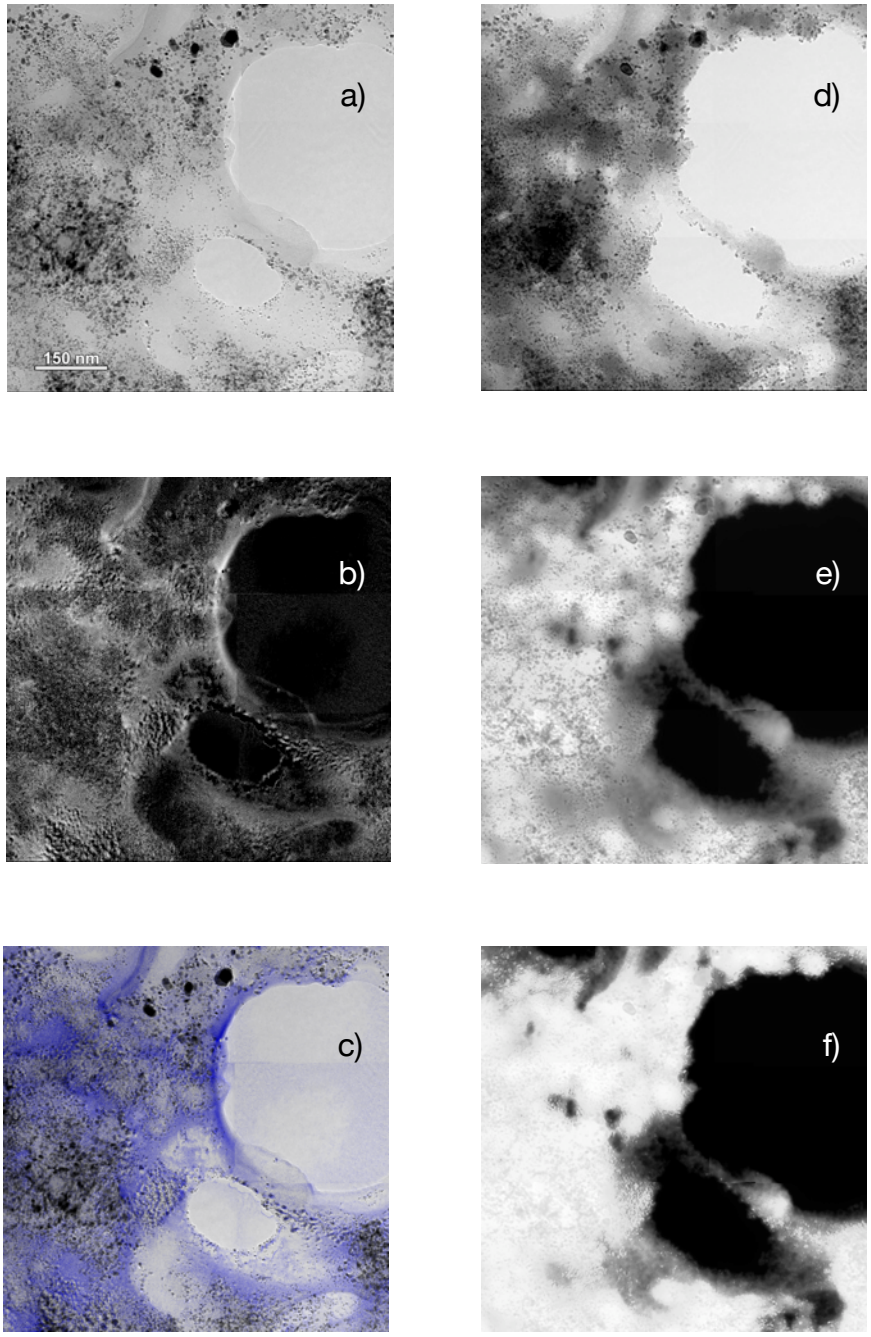

Figure 7.6. *Image of a Nafion filled pore (Nafion loading 60 vol. %). (a) unfiltered TEM image, (b) fluorine map, (c) superposition of (a) and (b) - fluorine distribution in blue, (d) zeroloss filtered image, (e) plasmon filtered image, (f) ratio of image (d) and (e).*

electrolyte content. This is due to a low thickness of these polymer electrolyte structures in the pores, as can be seen from the jump ratio image of the zero-loss (Figure 7.6 d) and the plasmon filtered image (Figure 7.6 b) recorded at the same sample position (Figure 7.6 f). The jump ratio image of the zero-loss and plasmon filtered image reflects thickness variations in the specimen. Therefore, regions of high image intensity correspond to relatively thicker parts of the specimen than dark ones. The jump ratio image shown in Figure 7.6 f) therefore confirms a low thickness of the polymer electrolyte structures coating the walls of the large pores in the lower right part of the image.

Fluorine distribution maps were also recorded for a specimen with lower Nafion concentration (40 vol. %). The maps resemble those obtained for the 60 vol. % sample, although less polymer electrolyte is found in large pores. Figure 7.7 shows a pore, partially covered with a thin Nafion layer. The polymer electrolyte film is of rather homogeneous thickness, but again significantly thinner than the section through the catalyst agglomerates surrounding the pore. As in Figure 7.7 a) several unsupported platinum particles can be seen at the fringe of the polymer electrolyte film. These platinum particles in the polymer electrolyte appear to be a repetitive feature, found in used as well as unused electrode samples. Since the platinum particles in the electrolyte are also found in unused samples, at least their initial deposition in the polymer electrolyte film is not linked to degradation phenomena of the catalyst. Therefore, they are most likely due to catalyst particles, which are mechanically sheared off from their support during the ink preparation process. Nevertheless, the platinum particles in the electrolyte may be involved in the degradation processes of the electrode, leading to an accelerated degradation of the polymer electrolyte [109,95] or may serve as nucleation centers for dissolved platinum [37,1].

The fluorine map of Figure 7.7 b) exhibits a stripe of high fluorine concentration in the upper part of the aggregated catalyst structure. A similar stripe is also found in the lower left part of the image. These stripes are most probably due to boundary regions between agglomerate particles, which are filled with polymer electrolyte. The fluorine signal detected from other parts of the electrode is significantly weaker. However, it is essentially uniform, indicating a thin but uniform layer of polymer electrolyte coating the catalyst and support particles, also in the inside of the catalyst agglomerates. Figure 7.8 shows a different part of the

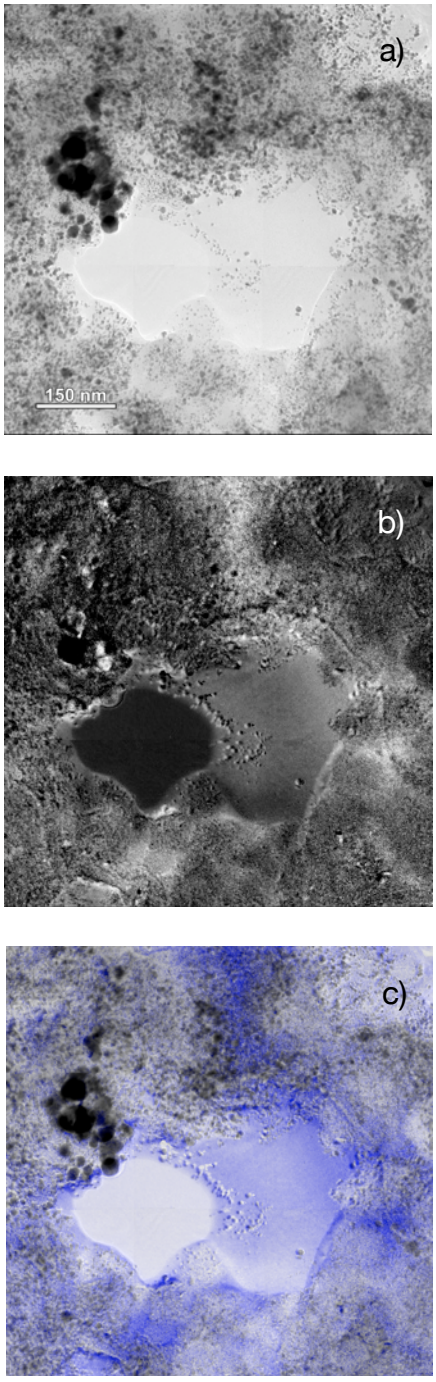

Figure 7.7. *Image of a pore partially filled with electrolyte (Nafion loading 40 vol. %). (a) TEM image, (b) fluorine map, (c) superposition of (a) and (b) - fluorine distribution in blue.*

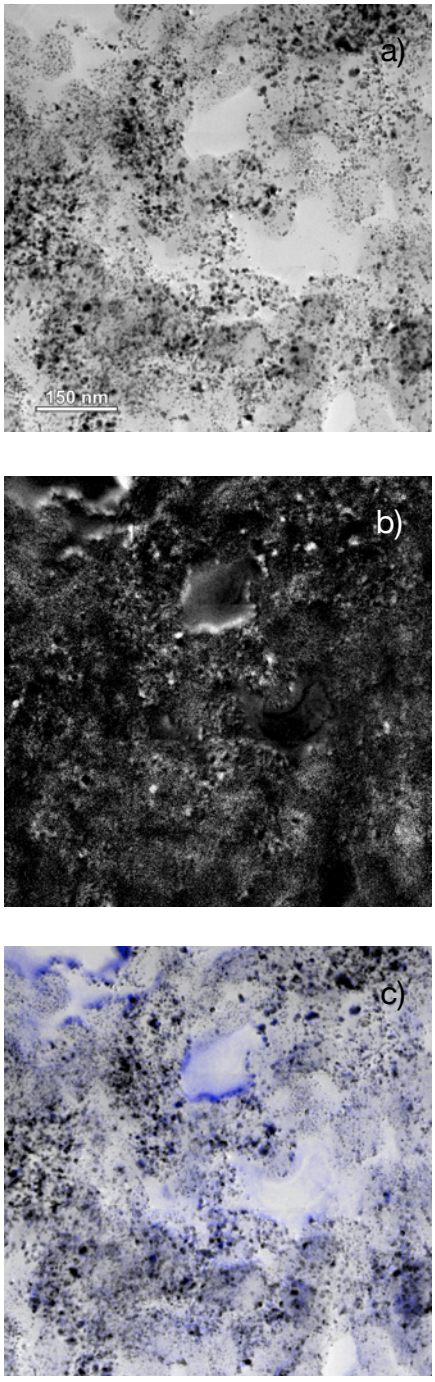

Figure 7.8. *Part of an electrode with no visible electrolyte features (Nafion loading 40 vol. %). (a) TEM image, (b) fluorine map, (c) superposition of (a) and (b) - fluorine distribution in blue.*

same electrode. Also in this image the polymer electrolyte is almost uniformly distributed, demonstrating that this is a consistent feature of the whole electrode.

These results partially contradict work presented by Song and coworkers [154], who claimed in a recent publication, that infiltration of the catalyst agglomerates is not possible with standard liquid ink processes but requires an auto-clave treatment to force the polymer electrolyte into the internal pores of the catalyst agglomerates. Song et al. derived this conclusion mainly from TEM images of samples stained with heavy metal ions to mark the polymer electrolyte. However, as has been shown in this chapter, this method is likely to produce artifacts. It is therefore most likely, that the authors interpreted an artifact of the staining process as polymer electrolyte distribution, coming to erroneous conclusions about its actual distribution. This concern seems to be even more justified, as the reported contrast improvements due to the Ag^+ staining significantly exceed those observed for the Cs^+ stained samples or what might be expected based on the concentration of sulfonate groups in the polymer electrolyte.

Infiltration of the catalyst agglomerates by the polymer electrolyte is further supported by data reported from Gode et al. [48]. Gode and coworkers determined pore surfaces for pores smaller than 10 nm, i.e. pores inside the agglomerates. Already at low polymer electrolyte concentrations the authors observed a tremendous decrease of the pore surface. The pores surface decreases further but to a lesser extent until reaching a polymer electrolyte concentration of about 30 wt. %. Further increase of the polymer electrolyte content resulted only in minor changes of the pore surface below 10 nm. In contrast, for pores larger than 10 nm an opposite trend was observed. The pore surface of these pores remained almost constant at polymer electrolyte concentrations below 30 wt. % and then started to decrease, when the concentration was further increased. These results agree very well with the TEM data presented. Therefore, based on the TEM measurements and the observations of Gode et al., the following structural model is proposed for the electrode of PEFCs:

In the ink polymer electrolyte adsorbs on the catalyst and support surface. Less aggregated polymer electrolyte rods may also diffuse into the interior of the agglomerates and adsorb to the internal pore walls. However, adsorption of poly-

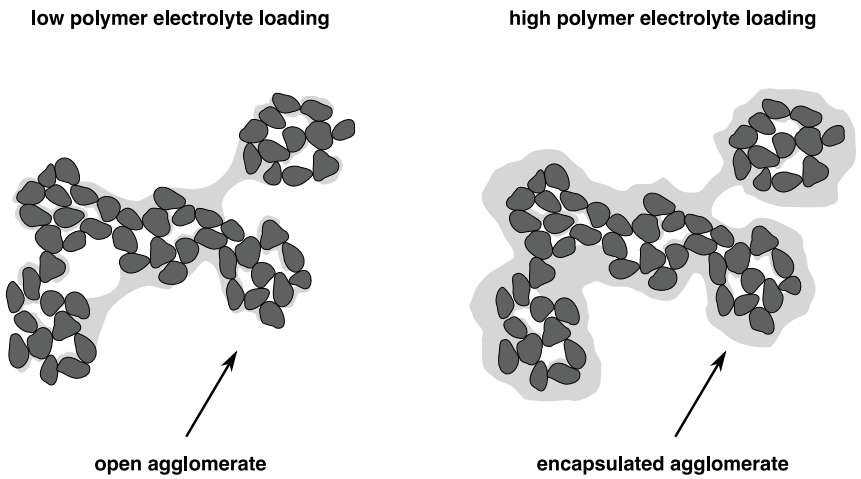

Figure 7.9. *Agglomerate models for electrodes prepared from polar (alcoholic) inks with low (left) and high (right) polymer electrolyte loading.*

mer electrolyte on the catalyst surface creates a negatively charged surface, which limits further adsorption on and diffusion of polymer electrolyte into the agglomerate particles. Therefore, excessive polymer electrolyte, that cannot adsorb on catalyst particles, will stay in solution at higher polymer electrolyte concentrations. This excess polymer electrolyte will then be cast into pores between the catalyst agglomerates during the drying process of the electrode. The TEM images suggest that the polymer electrolyte is not cast homogeneously onto the pore walls. Instead, it forms polymer films or fibers creating its own porous structure. At polymer electrolyte concentrations around 30 wt. %, the amount of polymer electrolyte cast into the pore space between the agglomerates is still low and reactant transport into or water removal from the agglomerates is not significantly impeded. At higher polymer electrolyte loadings the amount of polymer electrolyte in the secondary pores increases, causing a denser coating on the agglomerates, which can significantly impede reactant and water transport at higher current densities.

Therefore, the structure of the electrode may best be described by an aggregated network of catalyst agglomerates, having a thin but rather homogenous layer of adsorbed polymer electrolyte also on the interior pore walls, and a porous recast polymer electrolyte phase in the pore space between the agglomerates (Figure 7.9).

7.3. Conclusion

Staining of the polymer electrolyte with heavy metal salts resulted only in weak contrast improvements (Ba^{2+}) or was prone to staining artifacts (Cs^{+}). For samples stained with barium, small nanometer sized crystals, which were attributed to BaF_2 based on their lattice fringes, were found in the polymer electrolyte. The formation of the BaF_2 crystals is most likely linked to the degradation of the polymer electrolyte in the electron beam of the microscope. Their presence suggests, that significant structural changes occur in the polymer electrolyte on an atomic and molecular level during analysis in the electron microscope. However, microstructural changes of the electrode and membrane were not observed unless very high beam intensities were used, so that the results presented on the electrode structure should not be significantly affected by the polymer electrolyte degradation.

Contrasting with phospho-tungstic acid (PTA) yielded the most noticeable improvement of the specimen contrast and aided the identification of fine structural details, e.g. pores smaller than the section thickness. However, PTA staining is not selective and did not provide benefits for the characterization of the polymer electrolyte inside the catalyst agglomerates.

For this reason, energy filtered imaging was applied to obtain fluorine distribution maps of the electrode. The results of the fluorine mapping confirmed, that the polymer electrolyte, cast into the pores of the electrode, forms a complex porous structure. Further, fluorine mapping of agglomerate structures in the electrode strongly suggests an infiltration of the catalyst agglomerates by the polymer electrolyte.

Therefore, it was proposed, that in the liquid phase of the ink a thin layer of polymer electrolyte can adsorb on the catalyst surface including the inner pore walls of the agglomerates. Excessive polymer electrolyte, that does not adsorb, is cast into the pore space between the agglomerates forming a porous fibrillar structure.

8. Electrode Interfaces

Apart from the nanoscopic interfaces between the catalyst and the polymer electrolyte inside the electrode, the interfaces of the electrode layer formed with the membrane and the gas diffusion layer are of significant technical importance.

In this chapter the interface between the electrode and membrane will be studied more closely, using the energy filtered imaging approach already successfully applied to PEFC electrode structures. Furthermore, a new approach based on liquid metal infiltration of complete GDL-MEA structures will be presented for the analysis of the GDL electrode interface.

8.1. Membrane-Electrode Interface

At the membrane electrode interface protons must be transfered between the recast polymer electrolyte phase and the membrane. In general an intimate connection between the electrode and the membrane would be desirable to facilitate proton transfer as well as to provide sufficient mechanical integrity of the sample towards mechanical stress, caused by expansion and contraction of the membrane at different humidity levels [80,94].

Kim et al. investigated the effect of interface delamination using a two-dimensional anisotropic model. They could show that the ohmic resistance sharply increases in a nonlinear manner as interfacial delamination increases [80]. This effect was especially pronounced for the membrane electrode interface due to the low conductivity of the membrane. That a good contact between the electrode and membrane increases PEFC performance, was also recently demonstrated by Cho et al. [24]. The authors reported an ion beam treatment of the membrane surface, which led to a considerable increase of the cell performance.

8.1.1. Experimental

Analysis of the membrane-electrode interface was performed on an MEA prepared by hot-spraying a catalyst ink, consisting of a carbon supported platinum

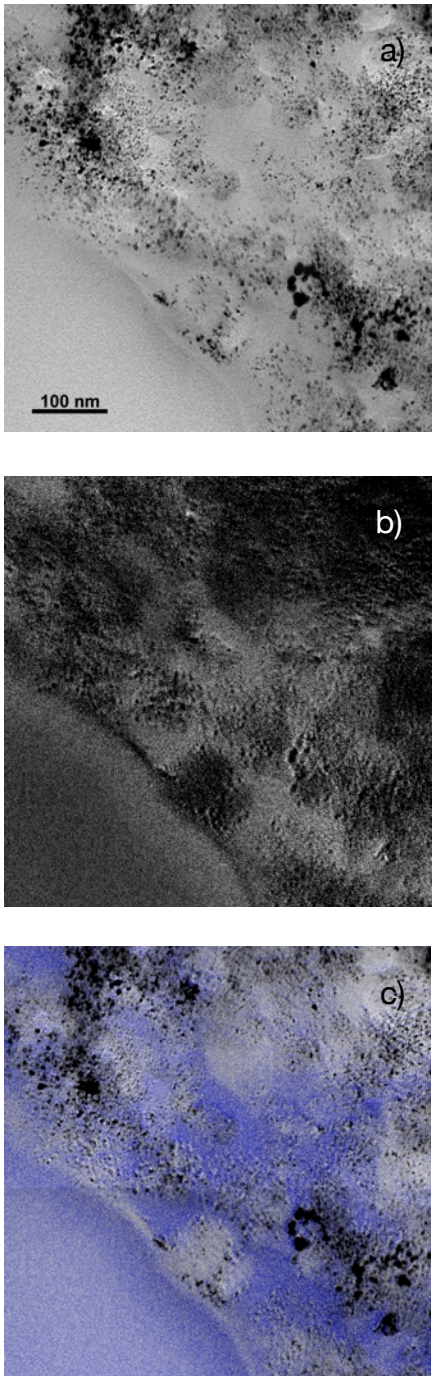

Figure 8.1. *Image of a membrane electrode interface (Nafion loading 50 wt. %).*
(a) TEM image, (b) fluorine map, (c) superposition of (a) and (b) - fluorine distribution in blue.

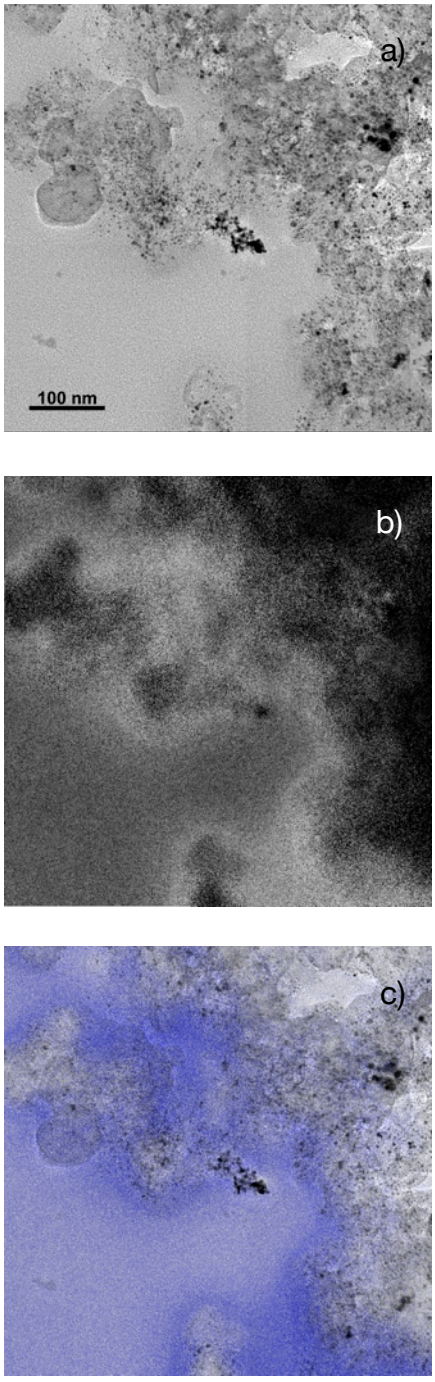

Figure 8.2. *Image of a membrane electrode interface (Nafion loading 50 wt. %).*
(a) TEM image, (b) fluorine map, (c) superposition of (a) and (b) - fluorine distribution in blue.

catalyst (ETEK, Pt 20 wt. %) and 50 wt. % Nafion, on a Nafion 117 membrane heated to 100 °C. After spraying the electrode layers onto the membrane the MEA was heat-treated at 140 °C for 45 min in a convection oven.

8.1.2. Results

Figures 8.1 and 8.2 show TEM images at two different positions of the membrane electrode interface and their corresponding fluorine maps obtained by energy filtered imaging. In each image the membrane is located at the lower left corner and the interface is almost diagonal to the images main axis. Although both figures belong to the same sample, the interface morphology differs considerably. The interface displayed in Figure 8.1 is sharp and the small gap in the fluorine distribution between the membrane and electrode indicates, that the recast polymer electrolyte of the electrode is not well connected to the extruded Nafion of the membrane. In contrast, the interface shown in Figure 8.2 is fuzzy and interpenetration of the catalyst and membrane can be observed. The interpenetration zone is about 200 nm large. Overlap of the fluorine distribution with parts of the catalyst agglomerates indicates that the agglomerates in the interpenetration zone are truly embedded in the polymer electrolyte matrix. The stronger fluorine signal at the boundaries of the agglomerates is most probably due to thickness variations of the specimen, indicating that the agglomerates slightly protrude out of the section.

Since both series of images were taken from the same sample within a spatially well confined region, local temperature variations are unlikely to be the cause for the observed structural differences. Figure 8.1 clearly demonstrates, that the recast Nafion of the electrode does not merge with the extruded Nafion of the membrane at the chosen heat-treatment temperature. Consequently, the Nafion seen in Figure 8.2 must be due to extruded Nafion of the membrane penetrating into the electrode. This means, that while the extruded Nafion is able to penetrate several hundred nanometers into the electrode to adapt to the interface morphology of the electrode, the recast Nafion is less able to undergo structural changes at the chosen heat-treatment temperature. This may be due to different structural properties of both types of Nafion. Moore and Martin reported, that temperatures of more than 160 °C are necessary to transform recast Nafion into

a structurally similar state as extruded Nafion [110]. This may explain, why under the chosen heat treatment conditions no interconnection between the recast and extruded Nafion is observed.

8.2. Electrode-GDL Interface

Apart from the electrode's interface with the membrane, the interface with the GDL is of considerable importance. At the electrode-GDL interface gas and water need to be transferred between the pore space of the GDL and the pores of the electrode. Therefore, a tight contact between the GDL and the electrode layer is desirable. This is achieved by hot-pressing the GDL with the MEA [40] or direct coating of the electrode onto the GDL [40,82,119].

While such a configuration is beneficial for gas and water transport as well as for the reduction of ohmic contact resistance, the tight connection between the GDL and electrode significantly complicates the structural characterization of these assemblies. This is due to the mechanical strength and comparatively large thickness of the carbon fibers generally used in the gas diffusion backings.

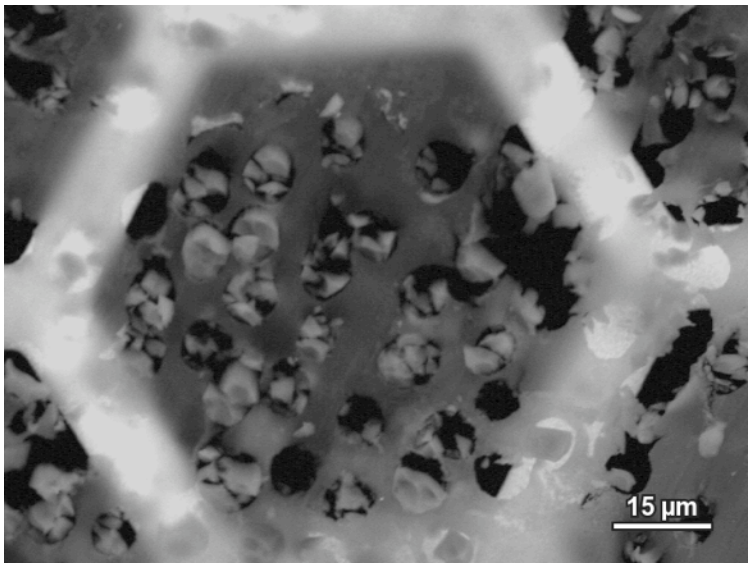

Figure 8.3. *SEM image of a thin section through a backing layer made of carbon fibers.*

Figure 8.3 shows, that sectioning of a gas diffusion backing, embedded in epoxy resin, leads to uncontrolled fracture and pullout of the carbon fibers from the epoxy matrix.

The pullout and brittle fracture of the carbon fibers as well as the largely different hardness of the electrode and backing layer result in a mechanical deterioration of the electrode layer. As a consequence, the characterization process, based on ultra-microtomed sections described in the previous chapters, could not be applied to complete MEA/GDL structures.

Therefore, in order to characterize the electrode-GDL interface, a method, which has been described by Cody and Davis for the analysis of the pore space in coals [25], was adapted to the examination of MEAs. The basic idea of this approach is to replace the epoxy resin used to embed the sample by an alloy with a low melting point.

Using a metal instead of epoxy resin has several advantages for the characterization of the fragile porous structure of the GDL and electrode by electron microscopy.

- Due to the large difference in atomic number between the metallic embedding media and the mostly carbonaceous materials of the MEA and GDL a high Z-contrast is obtained between the embedding media and parts of the sample.
- The high thermal and electric conductivity of the embedding media reduces charging and heating of the specimen, thus reducing specimen damage.
- The use of metals with high atomic number reduces the excitation volume for the collection of X-ray emission from the sample, which improves the lateral resolution for recording BSE images and element maps in the SEM.

Due to the presence of polymer materials such as the polymer electrolyte in the electrode or PTFE in the GDL, the melting point of the metallic embedding media should not exceed temperatures of about 120 °C. This limits the number of alloy systems to be considered. However, a number of bismuth based alloys

have melting temperatures low enough to be used as embedding media for PEFC MEAs and backings. Wood's metal, an alloy with a melting temperature of 70 °C, consisting of bismuth (50 %), lead (26.7 %), tin (13.3 %) and cadmium (10 %), is the most prominent of that kind. Due to its content of lead and cadmium concerns about its toxicity or environmental issues are justified. However, lead and cadmium free alternatives exist, such as Field's metal, which contains indium instead of cadmium and lead and has an even lower melting point temperature of 62 °C. Gallium might also be a possible alternative, as it liquifies at about 29.8 °C. However, the low melting point of gallium would require cooling of the sample during polishing and microscopy to avoid smearing or melting of gallium.

Despite environmental and toxicity concerns, Wood's metal was chosen for the first preliminary experiments, due to its wider availability and lower cost.

8.2.1. Experimental

The MEA investigated was a commercial MEA from E-TEK, consisting of a carbon supported platinum catalyst on both the anode and the cathode side, a carbon black based multi porous layer (MPL) and a woven carbon fiber backing on both electrodes.

For the infiltration with Wood's metal, a piece of the MEA was placed between two disk shaped parts of Wood's metal. In a second step the sample was evacuated in a sealed container and heated to about 80 °C to encapsulate the MEA in the metal. Thereafter, the sample was exposed to a hydrostatic pressure of 200 bar in a heated pressurizeable cell to infiltrate the pore space of the sample with the metal. After cooling to room temperature, the sample was cut and polished to obtain a sample suitable for microscopy.

8.2.2. Results

Figure 8.4 displays SEM images of the polished section recorded at different magnifications. The cut carbon fibers of the diffusion backing are clearly visible in the images as black disks of circular or elliptical shape, depending on their orientation to the sectioning plane. The woven structure of the fiber bundles is well preserved in the section. The fiber bundles approach and recede from the

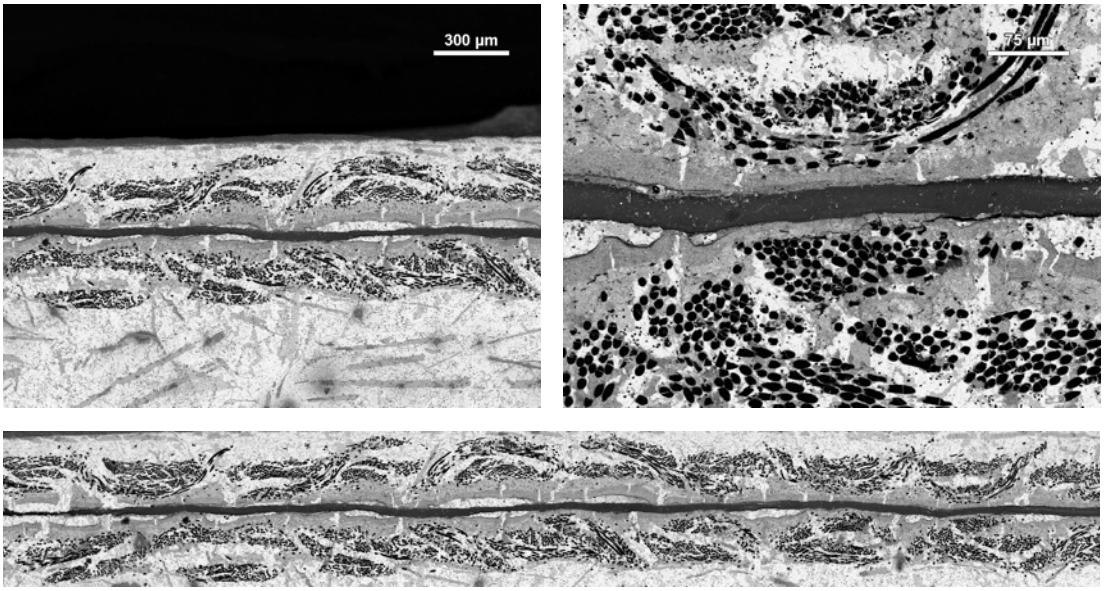

Figure 8.4. *SEM images of a commercial ETEK MEA with GDL and backing embedded in Wood's metal. The carbon fibers of the diffusion backing can be seen as black dots and the membrane is visible as a dark grey line running almost horizontally through the center of the images.*

membrane according to the texture of the fabric. The structure of the fabric apparently has a significant influence on the morphology of the catalyst and multiporous layer. In the left image of Figure 8.4 it can be seen, that the thickness of the electrode layer, sandwiched between the two gas diffusion backings and the membrane, is lowest, where the carbon fibers approach the membrane. On the lower side, the electrode layer becomes so thin, that some of the carbon fibers can be seen in direct proximity to the membrane, separated by a few micrometers only. At this position the MPL, visible in a slightly lighter grey as the electrode, appears to be completely absent. Instead, fragments of the MPL are located in the void space between the carbon fibers bundles.

In parts, where the carbon fibers recede from the membrane due to the texture of the fabric, the electrode often delaminates from the membrane and a gap filled with metal can be observed. This demonstrates that the woven structure of the GDL leads to a highly nonuniform contact pressure leading to a poor contact between the electrode and membrane at considerable parts of the electrode area.

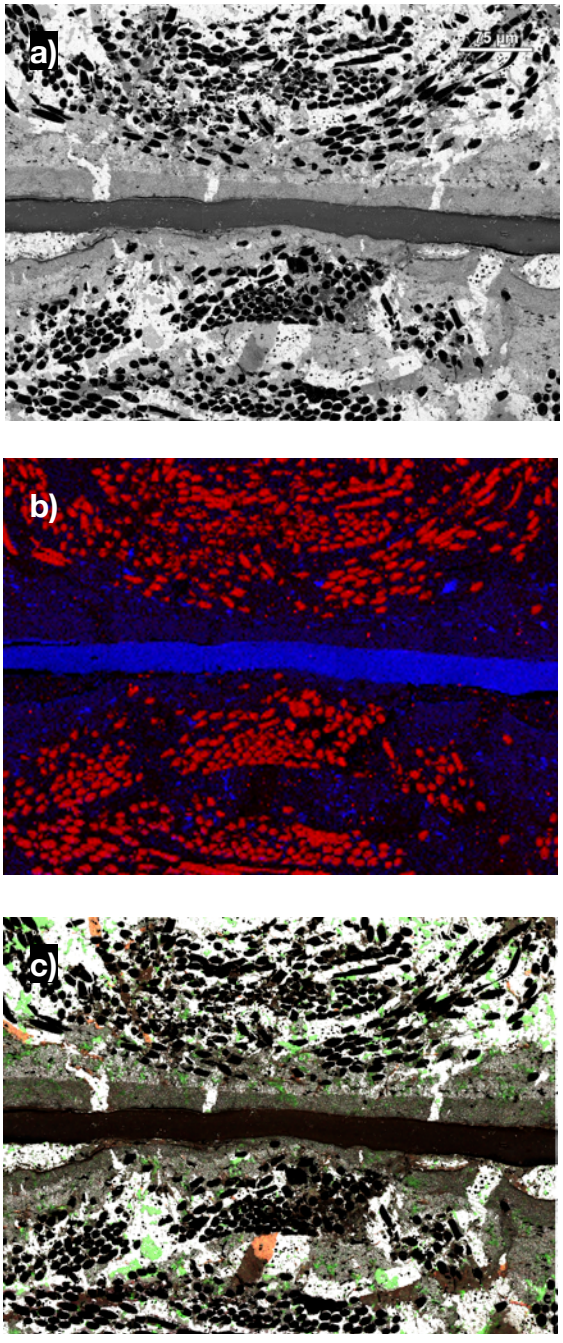

Figure 8.5. *Part of the Wood metal infiltrated MEA/GDL structure. a) BSE-image, b) EDX-mappings of carbon (red) and fluorine (blue), c) superposition of the BSE image and maps of tin (green) and cadmium (red).*

As one of the key functions of the GDL is the rapid removal of product water, it is often made water-repellent by mixing or coating the GDL with PTFE [151]. Therefore, in order to characterize the water-repellent properties of the GDL and to understand their effect on the water transport processes in the GDL, it is essential to know how the PTFE is distributed in the GDL.

EDX mappings of the carbon and fluorine signal (Figure 8.5 b) show, that the fluorine, i.e. the PTFE, is not homogeneously distributed in the GDL. Several larger PTFE-particles can be identified in the carbon fiber backing and the MPL. Most of these PTFE-particles can be found either in the MPL or in parts of the backing next to the MPL. This suggests, that the PTFE particles in the backing are most probably due to parts of the MPL penetrating into the backing. As a consequence, it can be concluded that the PTFE distribution in the backing is more uniform, with either considerably smaller PTFE particles or a homogeneous coating on the surface of the fibers, while the MPL contains large micrometer sized PTFE particles.

Maps of the alloying components tin and cadmium recorded along with the fluorine and carbon maps (Figure 8.5 c) showed, that not all the medium grey parts in the BSE image are due to fragments of the MPL, but that some of them have their origin in tin or cadmium rich precipitations. This slightly complicates direct interpretation of the BSE images, however, superposition of the element maps of cadmium and tin with the BSE image, as shown in Figure 8.5 c, can be used to distinguish the precipitations from MPL fragments.

8.3. Conclusion

A new promising approach for the characterization of complete MEA/GDL structures was presented. With this new embedding technique, it was possible to preserve the structure of the complete MEA including its GDL. It could be shown for a commercial E-TEK MEA, that the structure of the gas diffusion backing has a considerable influence on the electrode morphology and that penetration of the MPL into the carbon fiber backing occurs. Further, it was observed, that the way the electrode attaches to the membrane is significantly affected by the woven structure of the backing layer.

For routine characterization using only BSE and SE imaging, the presence of tin or cadmium rich precipitations was found to be a limiting factor, as this precipitations may be confused with parts of the MPL. However, EDX mapping of cadmium and tin can be used to distinguish precipitations from the MPL. In addition, improvements of the sample preparation process, like an accelerated cooling to reduce phase separation of the alloy, might improve the sample quality. Also the use of alternative alloys or pure gallium needs to be investigated and may improve the sample quality even further.

In this part, work, that has been carried out in a joint project between the Department of Chemistry at Tsinghua University, Beijing (China), the Bavarian Center of Applied Energy Research (ZAE), Garching (Germany), and the Institute for Materials Science at the Technische Universität Darmstadt is presented.

The focus of this project was to develop catalysts and electrode structures with improved mass and proton transport properties for direct methanol applications.

The catalysts characterized in this section were prepared at Tsinghua University, partially during a three month stay, which was part of the collaboration.

Part 5

Hydrous Ruthenium Oxide based Catalyst for Direct Methanol Fuel Cells

9. Catalysts for Direct Methanol Fuel Cells

9.1. Methanol Oxidation

Direct methanol fuel cells (DMFCs) are a special kind of PEFC using methanol instead of hydrogen as fuel. Due to the use of a liquid fuel, fuel storage is significantly simplified when compared to PEFC systems using pressurized or liquid hydrogen.

However, DMFCs suffer from considerably lower power densities, due to the sluggish kinetics of methanol oxidation. Nevertheless, the combination of low operating temperature, convenient fuel storage and high energy density of methanol (4.4 kWh/l) make DMFCs attractive candidates for small mobile devices such as mobile phones, smart phones and laptops.

The present section briefly illustrates the fundamentals of methanol oxidation, as the electrochemical reactions at the DMFC anode significantly differ from hydrogen fed cells described in chapter 2 and are fairly more complex. Subsequent sections will focus on the synthesis and characterization of hydrous ruthenium oxide supported catalysts and the structural analysis of MEAs prepared thereof.

The principles of methanol electrooxidation on platinum surfaces have been covered in a number of reviewing articles [56,68,140] and therefore will be summarized only briefly.

The electrooxidation of methanol on Pt surfaces in acid electrolytes takes place according to the following electrochemical reaction:

$$CH_3OH + H_2O \longrightarrow CO_2 + 6H^+ + 6e^- \qquad (9.1)$$

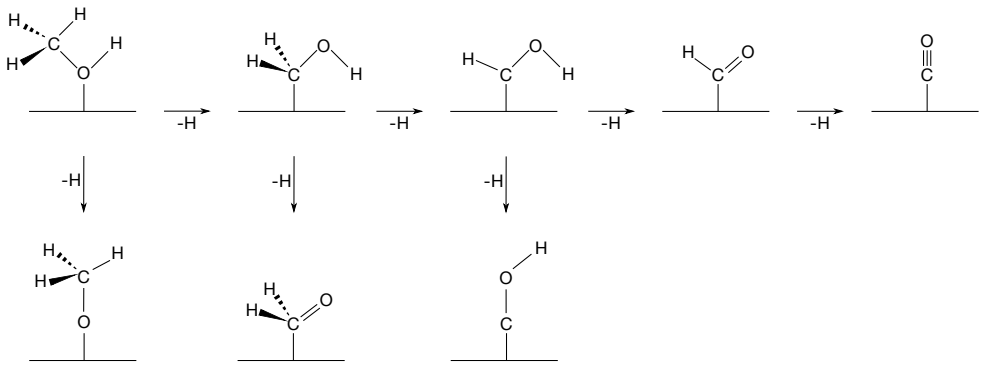

Figure 9.1. *Proposed adsorbate species involved in the electrochemical oxidation of CH_3OH according to Bagotzky et al. and Ishikawa et al. [9, 67]*

The reaction proceeds by a stepwise dehydrogenation of methanol. According to a reaction scheme proposed by Bagotzky et al. [9] shown in Figure 9.1, the reaction involves as many as eight different intermediates. In addition to the adsorbate species shown in Figure 9.1, formaldehyde and formic acid may form by oxidative desorption of some of the reaction intermediates.

Among the various adsorbate types CO is the most stable and has been found to be the predominant adsorbate species at low electrode potentials and high methanol concentrations. CO adsorbs strongly on platinum surfaces, having a binding energy of 1.81 eV on Pt(111). As a consequence, it can only be removed from the platinum surface by oxidation to CO_2. In aqueous electrolytes CO oxidation occurs by the reaction:

$$CO_{ads} + OH_{ads} \longrightarrow CO_2 + H^+ + e^- \qquad (9.2)$$

where OH_{ads} refers to an reactive adsorbed water species:

$$H_2O \longrightarrow OH_{ads} + H^+ + e^- \qquad (9.3)$$

On platinum the latter process requires electrode potentials exceeding 0.5 V vs. NHE leading to a large overpotential for methanol oxidation.

To promote water activation also at lower potentials platinum is either alloyed or decorated with ruthenium in current methanol oxidation catalysts. The activation of water on ruthenium sites, which promote the oxidation of CO adsorbed on platinum sites to CO_2 is frequently referred to as bifunctional mechanism.

Since methanol adsorbs poorly on Ru sites and dissociative electrosorption of methanol is very demanding of Pt sites, oxidative removal of CO at Ru sites competes with adsorption of methanol on Pt sites. Therefore, the optimum Ru coverage is shifted towards lower values for methanol oxidation when compared to electrooxidation of pure CO, for which according to experiment and theoretical considerations a surface coverage of 0.5 by Ru gives optimal catalytic performance. This was confirmed in a fundamental study of Gasteiger et al. using well-characterized Pt/Ru alloys, showing that a 10% Ru containing alloy performed considerably better than a 50 % one for DMFC operation [42].

9.2. Hydrous Ruthenium Oxide Based Catalysts

For nano-particle catalysts of platinum and ruthenium, there is a still ongoing discussion concerning the governing factors of the bifunctional mechanism. Since it was recognized that PtRu catalysts are actually not single-phase materials, but rather consist of mixtures of alloyed and non-alloyed platinum and ruthenium as well as hydrous or anhydrous oxides [137], several papers have been published concerning the function of ruthenium oxides in the process of methanol oxidation [5,14,50,100,86,137,152,156]. However, the results of these papers concerning the most active oxidation state of ruthenium for methanol oxidation are contradictory. While Long et al. report an increased methanol oxidation activity in the presence of hydrous RuO_2 whereas alloying of platinum and ruthenium should be avoided [100], Sirk et al. demonstrate that the catalyst is in its most active state when ruthenium is reduced to its metallic form [152]. Arico et al. even report an impeding effect of RuO_x species on the catalytic activity of unsupported PtRu catalysts [5]. On the other hand, an enhancement effect for

methanol oxidation was reported for platinum particles dispersed on calcined RuO_2 [170]. However, Lasch et al. [86,87], who studied the electrochemical activity of calcined and hydrous RuO_2 supported PtRu catalysts, found no enhanced catalytic activity for catalysts supported on calcined RuO_2 compared to Vulcan XC-72. When deposited on freshly precipitated hydrous RuO_2, the catalytic activity was even found to be several orders of magnitude lower. However, electron and proton conductivity of hydrous RuO_2 highly depend on the incorporated amount of water and only hydrous RuO_2 of the composition $RuO_2 \cdot 0.5\ H_2O$ provides both good proton and electron conductivity [30]. The poor performance of the hydrous RuO_2 catalyst prepared by Lasch et al. may therefore be due to a to strongly hydrated support, having poor electron conductivity. Furthermore, the catalyst prepared by Lasch et al. contained a significant fraction of reduced ruthenium. Therefore, another explanation of the poor catalyst performance might be a considerable decrease of free platinum sites for methanol adsorption, due to metallic ruthenium deposited on the platinum particles. This would also be in agreement with a recent report by Bock and coworkers [13], which states that the major factor determining the methanol oxidation activity is the Pt to Ru surface site distribution. Furthermore, experimental data was presented in the report indicating, that ruthenium oxides can be partially reduced to Ru metal in the electrochemical environment of methanol oxidation. Therefore, metallic Ru sites for catalytic water activation may be created also in unalloyed Pt/RuO_2 catalysts.

However, in all these reports, model electrodes have been used and measurements were carried out in liquid electrolytes, where intrinsic proton conductivity of the hydrous RuO_2 is playing an insignificant role. Reports about the effect of hydrous RuO_2 on catalyst utilization and proton conduction in MEAs are therefore limited. For unsupported Pt-Ru catalysts a beneficial effect of hydrous RuO_2 has previously been described by Thomas et al. [161]. According to their observations hydrous ruthenium oxide always present in the Pt-Ru black provides a proton conductivity sufficiently high to allow for electrodes without an additional proton conductor at least for thin layer electrodes.

Consequently, the use of Pt nanoparticles supported on $RuO_2 \cdot xH_2O$ as anode catalyst in particular for DMFC applications was studied. The ruthenium oxide applied as support material should provide intrinsic proton conductivity so that

the connection of all Pt nanoparticles to the proton conductor is ensured. On the other hand, reducing a certain amount of the ruthenium oxide in-situ might create the Pt-Ru catalyst desired for efficient oxidation of methanol or CO. Thorough structural investigations using X-ray diffraction (XRD), transmission electron microscopy (TEM) and X-ray photoelectron spectroscopy (XPS) of this catalyst as well as first fuel cell tests will be reported.

9.2.1. Hydrous Ruthenium Oxide as Catalyst Support for DMFC

Hydrous ruthenium dioxide, $RuO_2 \bullet xH_2O$ or RuO_xH_y, is a mixed electronic – protonic conductor and has an excellent electrochemical stability over a large potential range [163]. The combination of these properties makes it a very interesting support material for DMFC, because, due to its intrinsic proton conductivity, the polymer electrolyte in the electrode could be at least partially replaced, improving mass transport and proton conductivity at the same time. In addition, it may act as an active support, promoting CO oxidation by supplying activated water molecules.

In contrary to structural characterization of hydrous and anhydrous RuO_2 by extended X-ray absorption fine structure which suggested a truly amorphous state for highly hydrated samples, [107] a more recent publication by Dmowski et al. using X-ray scattering demonstrated that even in highly hydrated samples a local order similar to the rutile structure of bulk RuO_2 is maintained [30]. According to the authors the structure of hydrous RuO_2 is composed of a network of rutile-like RuO_2 clusters (with extensions in the sub-nanometer range for highly hydrated samples) and physi- and chemisorbed water in its grain boundary regions. In this model proton transport is provided by the hydrous grain boundary regions while electron transport takes place inside the network of RuO_2 clusters. Proton conductivity is therefore optimized for a high water content. However, electronic conductivity of these samples is low since most of the RuO_2 clusters are electronically insulated by hydrous grain boundaries. As water is removed, the RuO_2 clusters grow in size and the grain boundary regions become narrower and interconnections form. This model is consistent with electrochemical impedance spectroscopy data reported by Sugimoto et al. [157] and with experi-

mental results that show the highest pseudocapacitance for an intermediate water content of x = 0.5 in $RuO_2 \bullet xH_2O$ [30].

9.2.2. Catalyst Preparation

The hydrous RuO_2 supported catalyst was prepared as described by Chen et al. [19]. In short, hydrous RuO_2 was obtained by an oxidant-aided co-precipitation technique. In a first step, the pH of an aqueous $RuCl_3$ solution was adjusted to 4. Then an appropriate amount of hydrogen peroxide was added to the reaction solution by a constant-flow pump within 1 h. During this time the pH of the solution was constantly controlled and stabilized at 4 by addition of a sodium hydroxide solution. Thereafter, the pH was raised to 5.5 and a solution of $H_2PtCl_6 \bullet 6H_2O$ was added dropwise. To assure complete reduction of the platinum salt, $NaBH_4$ was added in excess. Finally, the catalyst was filtered and dried in air at 80°C for about 1h.

9.2.3. MEA preparation

The MEA was prepared using a hot-spraying technique. As electrolyte a Nafion NE 105 membrane was used. Commercial Pt-black catalyst HiSpec 1000 by Johnson & Matthey was used as cathode catalyst at a loading of 4 mg/cm^2 and a Nafion fraction of 9 wt%. On the anode side the hydrous RuO_2 supported platinum catalyst was used. 9 wt.% Vulcan XC-72R carbon black was added to the anode side to enhance its electronic conductivity. A comparatively low amount of Nafion of only 5 wt.% compared to about 15 wt.% with standard PtRu black catalyst was used. The ink for spraying the electrode was prepared by dispersing the carbon black in ethanol. Subsequently about the same amount of water was added followed by the appropriate amount of DuPont™ Nafion dispersion DE2021 with 20 wt.% Nafion. Finally, the pre-ground catalyst was added. The mixture was then dispersed for 10 minutes in an ultrasonic bath and subsequently stirred for three days using a magnetic stirrer. A catalyst loading of about 2 mg/cm^2 was applied.

9.2.4. Structural Characterization

To achieve a high proton conductivity in the catalyst, the supporting RuO_2 phase should be in a highly hydrated amorphous form. In low resolution TEM images the supporting RuO_2 phase is barely visible due to the high platinum loading of the catalyst (Pt/Ru ratio of 1). Figure 9.2 shows that the Pt particles are densely distributed on the new support material. In spite of the dense distribution the platinum particles seem to be hardly agglomerated. Based on 150 measured particles the average particle size was determined to be 4.9 nm with a standard deviation of ±1.1 nm.

At high resolution the supporting RuO_2 can be clearly identified as amorphous phase surrounding the platinum particles. However, high resolution imaging also shows that the hydrous RuO_2 phase is not only supporting the platinum particles, but also covers them (Figure 9.3). The origin of this amorphous hem on top of the platinum particles is yet unclear. It is possible that parts of the hydrous RuO_2 have not completely solidified and are still in a kind of solubilized state when the deposition of platinum particles is carried out. This solubilized hydrous RuO_2 may then deposit on the platinum particles that have been formed in the reduction step.

The XRD pattern of the as-prepared catalyst (Figure 9.4) shows only diffraction peaks for platinum confirming the amorphous state of the hydrous RuO_2 as it was observed by TEM. Evidence for the presence of hydrous RuO_2 can only be found by a slight increase of the background where the strongest diffraction peaks of tetragonal RuO_2 would be expected (Figure 9.4, arrow). Rietveld refinement of the pattern with a single platinum fcc phase resulted in a lack of intensity between the platinum (111) and (200) reflection in the simulated pattern.

The position of reduced intensity corresponds well with the peak position of the (001) reflection of metallic ruthenium. A small fraction of metallic ruthenium would also account for the small bump observed between the platinum (200) and (220) peak (2θ ~25°). For the platinum phase a cell constant of 3.912(6) Å and a particle diameter of 3.37 nm was determined by Rietveld refinement. The ob-

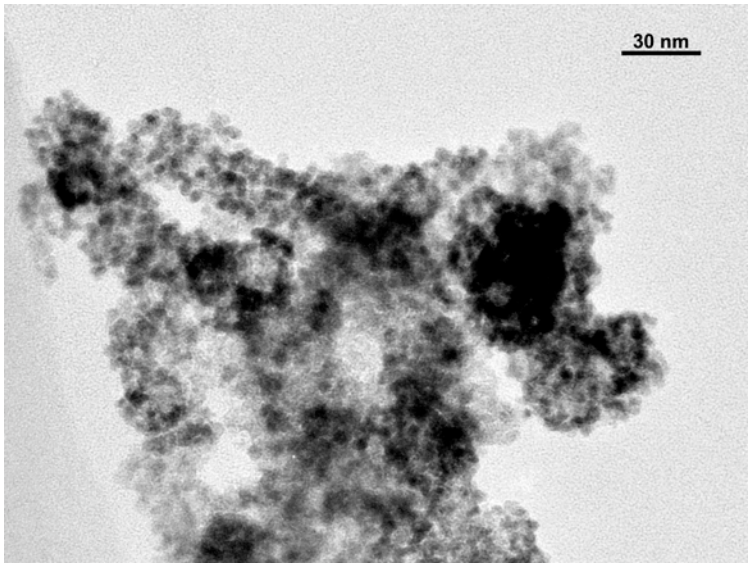

Figure 9.2. *TEM image of a platinum catalyst supported by hydrous RuO_2. The image shows highly agglomerated platinum particles. Individual RuO_2 particles from the support can hardly be distinguished, which is most probably due to the high platinum loading.*

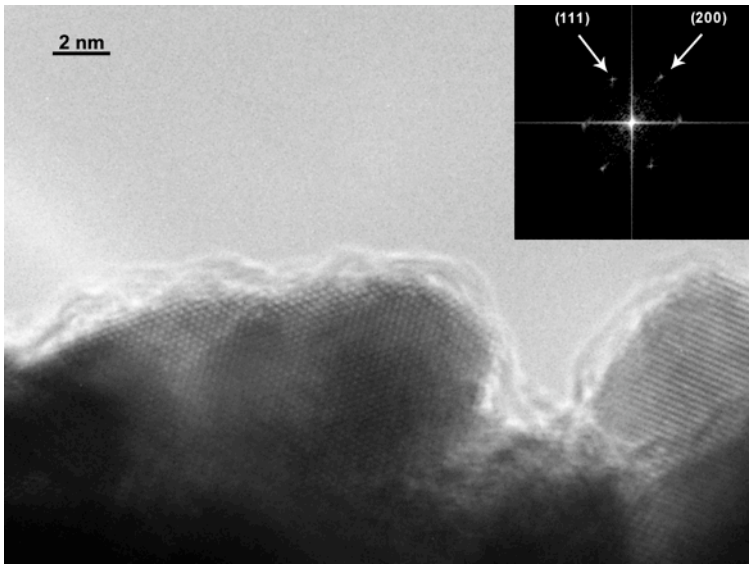

Figure 9.3. *High resolution TEM micrograph of the catalyst shown above. An amorphous hem, which is most probably due to RuO_2, was found to cover the platinum particles, which could be clearly identified by Fourier transformation of their lattice fringes (see inset in the image).*

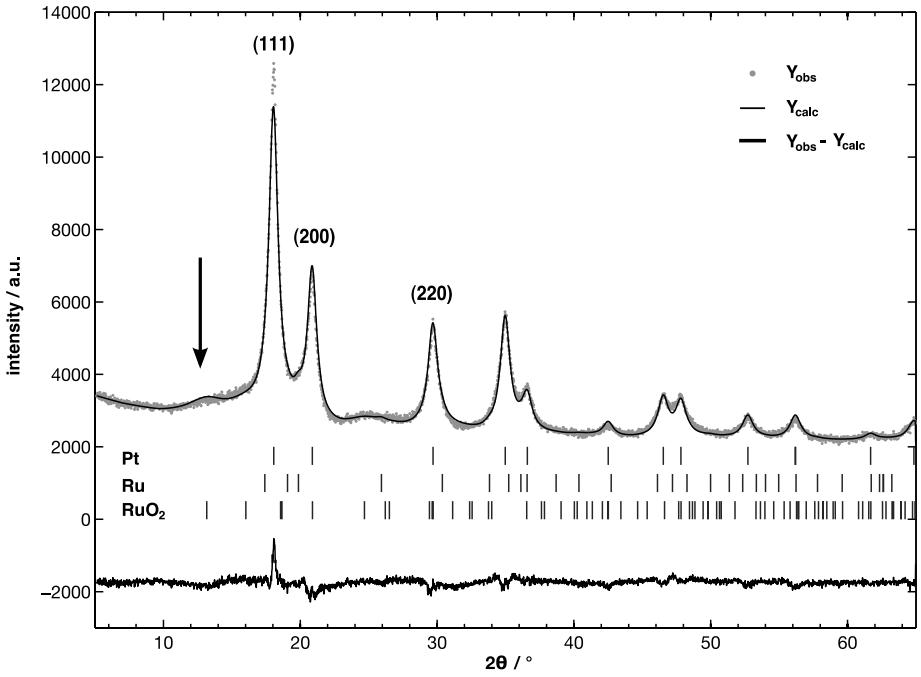

Figure 9.4. *XRD pattern of the hydrous RuO_2 supported catalyst. Measured* (Y_{obs}) *and calculated data* (Y_{calc}) *obtained from Rietveld refinement are displayed in the plot. Vertical lines indicate the peak positions of the platinum (fcc), ruthenium (hcp) and RuO_2 phases included in the refinement. The main platinum peaks have been labeled by their corresponding Miller indices.*

served cell constant is slightly smaller than that of bulk platinum (3.924 Å). However, alloying seems to be unlikely under the chosen experimental conditions. The cell constant is in good agreement with that reported for carbon supported platinum nanoparticles (3.916 Å) [3]. The smaller cell constant may therefore be attributed to size effects and particle support interactions rather than alloying of platinum and ruthenium.

XPS was carried out on the as-prepared catalyst to analyze the oxidation state of the supporting hydrous RuO_2 phase. A detailed scan of the Ru 3d region is shown in Figure 9.5. The spectrum was deconvoluted into three components with binding energies (BE) at 280, 280.8 and 282.7 eV for the Ru $3d^{5/2}$ spin-orbit contribution and the corresponding Ru $3d^{3/2}$ spin-orbit contribution

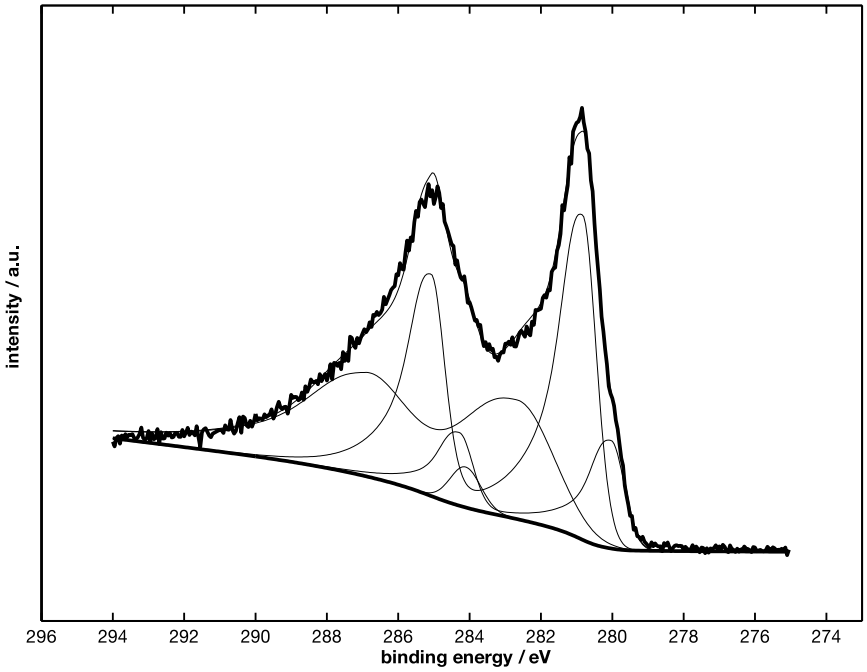

Figure 9.5. *Ruthenium 3d XPS spectrum of the as prepared hydrous RuO_2 supported catalyst. The spectrum has been fitted using one metallic (low binding energy) and two oxide components (higher binding energies). Carbon impurities were taken into account by an additional component at around 284 eV.*

shifted to 4.2 eV higher binding energies. An additional component with no counterpart at higher BE was added at 284.1 eV to account for adventitious carbon contaminations of the sample.

The first component at 280 eV corresponds well with the tabulated value for ruthenium metal (279.9 – 280.1 eV [172]). The XPS measurement therefore confirms the results of the XRD analysis that some of the ruthenium in the catalyst is present as Ru metal. However, the contribution of metallic ruthenium is low compared to the contributions of oxidic ruthenium species at binding energies of 280.8 and 282.7 eV, confirming that most of the ruthenium is in an oxidized state. The assignment of the oxidic contributions at higher binding energies is not as straight forward. It is generally agreed that the component at lower bind-

ing energies arises from rutile like coordinated RuO_2 species [137,53,78] while the origin of the higher binding energy component has been vigorously disputed. Some researchers have assigned the contribution to higher oxidation states of ruthenium such as RuO_3 and RuO_4 [77]. This assignment is questionable since these species are known to exist only in the vapor phase [147]. Other assignments include final-state screening effects [28,135] and hydrous RuO_xH_y species [137]. However, theoretical considerations by Reuter et al. [132] suggest that final state screening effects cannot account for the large shifts observed for the high binding energy component. Assignment to RuO_xH_y species therefore seems the most plausible.

Determination of the surface composition of the catalyst from Ru 3d and Pt 4f orbitals resulted in a Pt:Ru ratio of about 1:2. This result differs strongly from the Pt:Ru ratio in the bulk which has been determined by X-ray fluorescence analysis to be 60:40. Considering that the TEM analysis showed a dense coverage of platinum particles on the hydrous RuO_2 support and that the mean free path length of photoelectrons from Pt 4f is only about 1.6 nm [199] rather a reversed Pt:Ru surface ratio should be expected. The increased Ru concentration on the surface therefore suggests that the platinum particles are indeed covered by a layer of hydrous RuO_2, as inferred from the TEM analysis of the catalyst.

9.2.5. Electrochemical Measurements

Electrochemical characterization of the catalyst was done both for thin films on planar model electrodes and for anode gas diffusion electrodes in a technical DMFC membrane electrode assembly (MEA).

Model electrodes were prepared for the hydrous RuO_2 supported platinum catalyst and pure hydrous RuO_2 prepared by the same method. 1 mg of catalyst was dispersed in 25 µl Nafion solution (20 %) by ultrasonic treatment for 20 seconds. The ink was readily applied to a planar gold electrode and dried in air at 80 °C for about 1 hour.

Catalyst characterization was carried out by cyclic voltammetry at room temperature in a three-electrode cell. 1 M $HClO_4$ was used as electrolyte for all

measurements. Potentials were measured against a standard calomel electrode (SCE) but are referenced to the normal hydrogen electrode (NHE).

Figure 9.6 shows cyclic voltammograms (CV) of the catalyst in pure $HClO_4$ electrolyte before and after the electrode has been exposed to 1 M methanol solution for 1 hour. Comparison of the two CVs demonstrates that exposure to

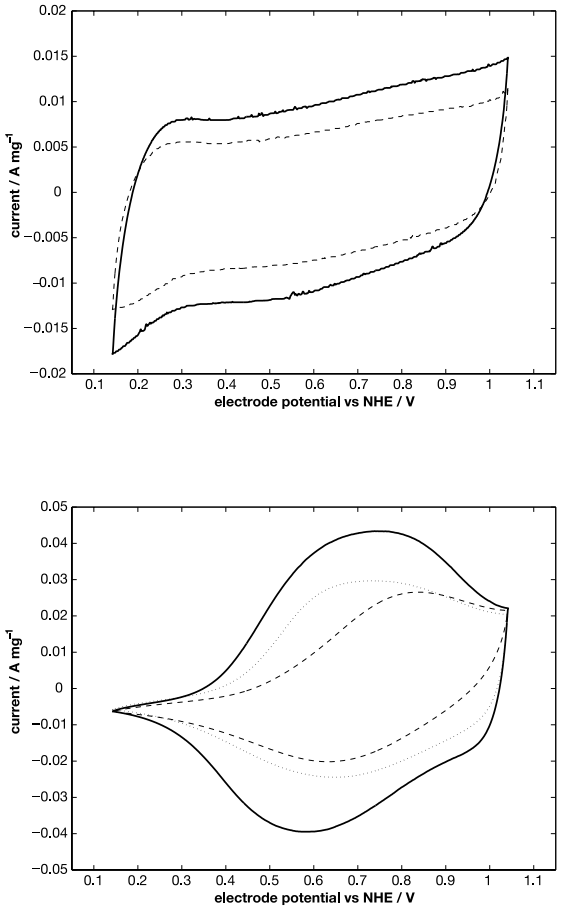

Figure 9.6. *Top graph: Cyclic voltammograms of the catalyst in 1 M $HClO_4$, before (solid line ——) and after (dashed line - - -) exposure to 1 M methanol solution for 1 hour. Bottom graph: Cyclic voltammograms of pure hydrous RuO_2 in 1 M $HClO_4$, as prepared (solid line ——), after exposure to 2 M methanol solution (dashed line - - -), and sample annealed at 70 °C (dotted line ····). All cyclic voltammograms were recorded at a scan rate of 50 mV s^{-1}.*

methanol solution strongly affects the capacitance of the hydrous RuO_2 phase. Both CVs exhibit almost rectangular shape characteristic for the pseudo-capacitive behavior of hydrous RuO_2. However, the area under the CV curve of the electrode previously exposed to methanol is smaller indicating a decrease in capacitance due to methanol exposure. This decrease can either be caused by a reduction of hydrous RuO_2 to metallic ruthenium or a decrease in proton conductivity due to partial replacement of structural water by methanol.

In the former case an increase in pseudo-capacitance should be observed by repeated cycling due to reoxidation of the metallic ruthenium [152]. Yet, no increase in pseudo-capacitance could be observed even after extensive cycling.

Evidence that the decrease in capacitance is due to diffusion of methanol into the hydrous regions of the RuO_2 is also given by cyclic voltammetry of pure hydrous RuO_2. Figure 9.6 (bottom) shows that the pseudo-capacitance of the hydrous RuO_2 can be recovered to a certain degree after exposure to methanol solution by annealing the sample at 70 °C for 1 hour. However, the recovery process is not complete. This might be due to an incomplete removal of methanol as well as a depletion of water of the hydrous RuO_2.

The CV measurements indicate that diffusion methanol into the hydrous regions of the RuO_2 may causes a decrease of proton conductivity in the hydrous domains due to partial replacement of water by methanol molecules.

9.2.6. Fuel Cell Tests

A number of tests were performed on the MEAs prepared with the hydrous RuO_2 supported catalysts. To obtain an indication of the active surface area compared to carbon supported PtRu catalysts, CO stripping measurements were performed. Methanol oxidation was studied both in half-cell and full cell setup using an Autolab PGSTAT30 potentiostat with installed 20 A booster module. Finally ohmic resistance was determined by electrochemical impedance spectroscopy using an Autolab PGSTAT20 potentiostat with installed FRA2 impedance module. For the half-cell measurements, the CO-stripping experiments, and the impedance spectroscopy measurements the cathode of the MEA was fed

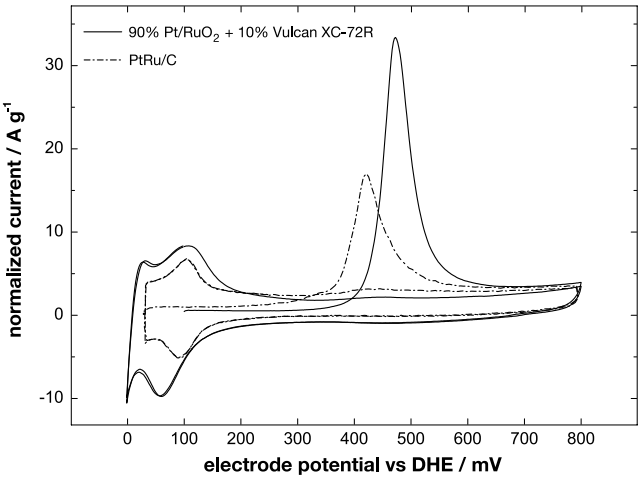

Figure 9.7. *CO stripping voltammograms of gas diffusion electrodes. Pt/$RuO_2 \cdot xH_2O$ catalyst (——solid line) and a commercial PtRu/C (20 wt. % on Vulcan XC-72R) catalyst (--- dashed line) for comparison.*

with 50 ml/min (STP) hydrogen and used as dynamic hydrogen electrode for counter and reference electrode in a pseudo-three electrode setup.

Half-cell measurements

CO-stripping experiments carried out as half-cell measurements at a complete MEA using the cathode side as a dynamic hydrogen electrode showed surprisingly high activity towards CO oxidation (Figure 9.7). In comparison to a carbon supported PtRu catalyst with 20 wt.% noble metal fraction, the RuO_2 supported catalyst displays a much higher mass activity. The onset and peak potential for CO oxidation are shifted to higher potentials, when compared to the carbon supported catalyst, but still significantly lower than those of pure platinum.

Assuming that CO does not adsorb on RuO_2 but only onto Pt and reduced Ru particles, the area under the CO oxidation peak can be used to calculate the

electrochemically active platinum surface area of the catalyst according to the following equation:

$$A_{EC} = \frac{Q_{CO_{ads}}}{420(\mu C cm^{-2})} \tag{9.4}$$

where A_{EC} is the electrochemically active catalyst surface area and Q_{COads} the background corrected charge under the CO oxidation peak. The active platinum surface was then related to the BET surface area of the catalyst (84 m^2/g) to obtain a measure for the catalyst utilization in the MEA. Catalyst utilization determined by this method resulted in an unreasonably high value exceeding 125%.

The reason for this high catalyst utilization has not been understood completely yet. It is possible that the hydrous RuO_2 obscures CO stripping results due to its pseudo-capacitive effect. However, a purely capacitive effect appears unlikely, as also other PtRu catalysts contain significant amounts of hydrous RuO_2 and have never been reported to have a catalyst utilization exceeding 100% [137]. Therefore, two other explanations are presented to account for the extremely high catalyst utilization:

- The electrochemical active platinum surface is larger than the catalyst surface determined by BET. It has been demonstrated that methanol is potentially able to diffuse into the hydrous regions of RuO_2. CO which is an even smaller molecule than methanol might therefore diffuse into the hydrous regions as well and adsorb to platinum particles covered by RuO_2. Those particles may then give an additional contribution to the CO oxidation current. But CO may not only adsorb onto the platinum particles, some CO may also remain in the channel network. Since diffusion paths from the hydrous RuO_2 to the platinum particles are comparatively short for the examined catalyst due to its proposed core-shell structure, this CO might as well be oxidized during the potential sweep of the CO stripping experiment. The amount of oxidized CO would therefore be larger than in the case when CO is only adsorbed at the platinum particles.

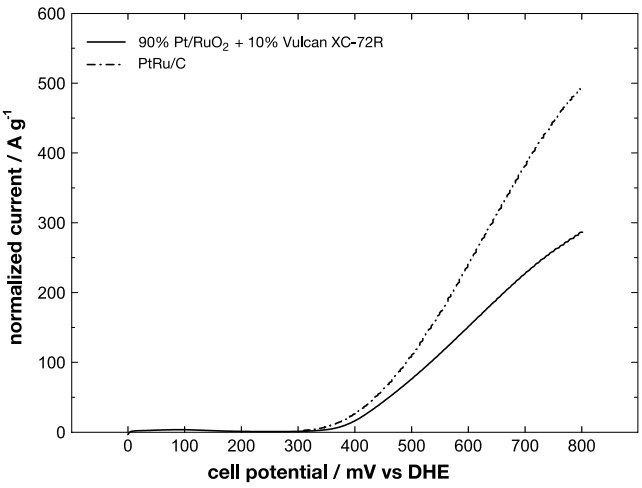

Figure 9.8. *DMFC half-cell measurement for methanol oxidation. Pt/RuO_2 xH_2O electrode (—— solid line), PtRu/C (20 wt. % on Vulcan XC-72R) catalyst (--- dashed line). Measurements were carried out at 50 °C with the cathode used as dynamic hydrogen electrode.*

- Hydrous RuO_2 may be partially reduced to metallic ruthenium. There is evidence that ruthenium oxides can be reduced to metallic ruthenium under the conditions used for CO adsorption [14,171,115]. Since CO is able to adsorb on metallic platinum as well as metallic ruthenium sites, reduction of RuO_2 would lead to the formation of new CO adsorption sites as long as no free platinum surface is lost during this process.

However, regardless of the exact origin of the high catalyst utilization CO stripping shows that, in spite of the low Nafion content in the electrode of only 5 wt.%, the catalyst utilization in the MEA is high. This indicates that, at least in the case of CO oxidation, when no methanol is present, the hydrous RuO_2 contributes significantly to the protonic and electronic connection of the catalyst particles.

In half-cell measurements for methanol oxidation the situation is inverted. Here, the PtRu catalyst supported on Vulcan XC-72R has the higher mass activity than the RuO_2 supported catalyst (Figure 9.8). The reversed CO and methanol oxida-

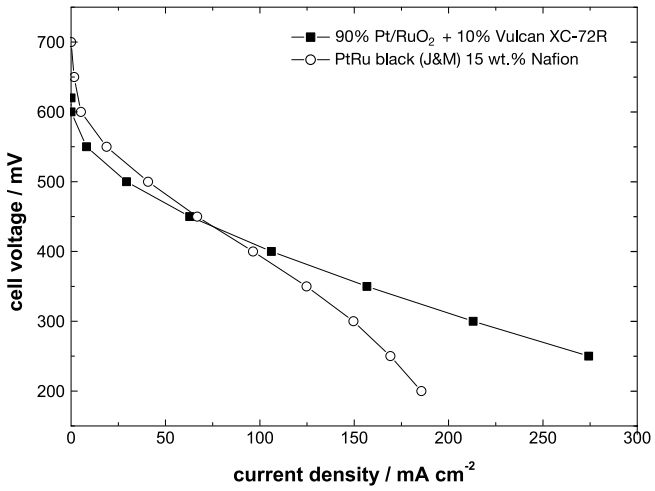

Figure 9.9. *Current-voltage curves for methanol oxidation in a DMFC full-cell arrangement. The curve of the hydrous Pt/RuO_2 catalyst is shown in comparison to an MEA prepared with a standard PtRu black catalyst (Johnson Matthey). Both measurements were carried out at 50 °C with 1 M methanol fed at 6 ml min^{-1} and an air flow of 500 ml min^{-1} (STP).*

tion behavior of the two catalysts may be due to differences in their Pt:Ru surface ratio. Since methanol electrooxidation is more demanding of free Pt adsorption sites than that of CO [42], the result may indicate that the surface of the hydrous RuO_2 supported catalyst is richer in Ru sites due to partial reduction of RuO_2 to metallic ruthenium.

Full-cell measurements

In DMFC full-cell measurements a mixed picture of the MEA performance was obtained. At low current densities the MEA prepared with the hydrous RuO_2 supported catalyst was inferior to that of a standard PtRu black catalyst from Johnson Matthey. The poorer performance is caused by a larger voltage loss in the electrokinetically controlled regime of the curve, indicating slower electrode kinetics of the Pt/RuO_2 catalyst. This is consistent with the DMFC half-cell measurements, also attributing a lower methanol oxidation activity to the hy-

drous RuO_2 supported catalyst. However, at current densities larger than 75 mA/cm^2 the MEA with the Pt/RuO_2 catalyst outperforms the MEA with PtRu black catalyst (Figure 9.9). This is mainly attributable to a very low ohmic resistance of 210 $m\Omega \cdot cm^2$ compared to about 725 $m\Omega \cdot cm^2$ for the PtRu black MEA. It is generally agreed, that the ohmic resistance of an MEA is mainly controlled by its proton conductivity, except for very high polymer electrolyte loadings where the polymer electrolyte may lead to electronic insulation of the catalyst particles [139,48]. The ohmic resistance of the MEA is therefore even more remarkable, since its Nafion content was reduced in comparison to that of the PtRu black reference electrode. This indicates, that the hydrous RuO_2 indeed contributes to the proton conductivity inside the electrode, leading to a much reduced ohmic resistance.

9.3. Conclusion

Pt nanoparticles supported on hydrous RuO_2 were prepared by $NaBH_4$ reduction. TEM analysis of the catalyst showed, that the platinum particles were surrounded by an amorphous hem of hydrous ruthenium oxide. Full- and half-cell measurements indicated, that the hydrous RuO_2 gets partially reduced to metallic ruthenium, leading to platinum particles decorated with metallic ruthenium. Nevertheless, the methanol oxidation activity of the catalyst was lower than that of a standard PtRu black catalyst. This was attributed to a PtRu surface site ratio less favorable for methanol oxidation than that of the PtRu black catalyst. Despite the lower methanol oxidation activity, the catalyst outperformed the PtRu black catalyst in full-cell measurements at higher current densities. A low ohmic resistance, i.e. high proton conductivity, of the electrode prepared of the hydrous RuO_2 supported catalyst was identified to be responsible for the improved performance at high current densities.

The results demonstrate that hydrous RuO_2 used as a catalyst support may reduce mass and proton transport related performance losses, by creating a reaction environment for methanol oxidation possessing high intrinsic proton conductivity without significantly impeding the transport of reactants.

10. Catalysts Supported on Hydrous Ruthenium Oxide Coated CNTs

In the previous chapter it has been shown that hydrous RuO_2 is a promising support material for catalysts being used for methanol oxidation, as it is both electron and proton conductive and may act as an active support material providing activated water for CO oxidation. However, the use of pure hydrous RuO_2 as catalyst support has several shortcomings:

- The catalyst supported on hydrous RuO_2 exhibited a high degree of aggregation or agglomeration, which is unfavorable for fast mass transport of reactants and CO_2 which is generated during fuel cell operation. Agglomeration of the catalyst may further reduce the accessible catalyst surface, leading to inefficient use of the noble metal catalysts.
- Ruthenium is a precious metal and its commodity prices have risen in recent years to levels comparable to platinum. However, the use of pure hydrous RuO_2 requires large amounts of ruthenium and is therefore economically undesirable.

To overcome this problems a new approach using a hydrous RuO_2/carbon nanotube composite material is presented. This approach addresses most of the mentioned shortcomings by providing (i) a microstructure more suitable for mass transport and (ii) by applying only a thin coating layer of hydrous RuO_2 on the tube surface by which the total amount of ruthenium can be reduced.

Carbon nanotubes (CNTs) have been chosen as substrate material, as this carbon material possesses a couple of interesting properties, which make it an ideal candidate for future DMFC and PEFC catalyst supports:

- CNTs form a three-dimensional network structure, which is favoring the flow of reactants, therefore providing a large reaction zone when fabricated into electrodes.
- They possess a more defined crystalline structure than carbon blacks, which grants higher electric conductivity and improved chemical and thermal stability.

As the fibrous CNT structure is thought to improve mass transport, CNTs should have the largest benefit if applied as cathode catalyst in PEFCs or as anode catalyst in liquid feed DMFCs, where mass transport limitations can lead to considerable performance losses.

Recently, several publications indeed reported that higher performances can be obtained with CNT supported catalysts as compared to standard carbon blacks [93,72,126,159]. For methanol fuel cells Prabhuram et al. presented fuel cell measurements showing 35-39 % higher power densities for multiwalled carbon nanotubes (MWNT) supported PtRu catalysts compared to a standard PtRu/C on carbon black catalyst [126]. Tang et al., who used a CNT supported platinum catalyst as PEFC cathode catalyst, even achieved power densities of 431 mW/cm^2 and 613 mW/cm^2 for ultra-low loadings of platinum of only 6 µg Pt/cm^2 and 12 µm Pt/cm^2, respectively [159]. These values are among the highest currently reported for PEFCs, both in respect of absolute power density as well as specific mass activity.

On the search for optimized catalyst supports even more complex CNT based structures have been proposed. Several authors examined the use of CNTs grafted onto carbon fibers or carbon paper [98,175,176], while He et al. prepared PtRu decorated CNTs grafted on different titanium oxide supports to be used for methanol electrooxidation [61]. However, although initial fuel cell tests of these structures showed somewhat higher performances when compared to conventional catalysts [176], benefits over plain CNT supported catalysts still need to be proven.

As fuel cells are getting closer to commercialization, increasing attention is being payed to the durability of fuel cell catalysts. Catalyst corrosion in fuel cells can either proceed by dissolution and growth of the noble metal particles [1,52,196] or by degradation of the carbon support material [47,52,131,177]. Both processes lead to premature failure of the device and should be reduced as far as possible. Recent reports about the degradation stability of CNT supported catalysts indicate that CNTs not only show lower carbon corrosion compared to conventional carbon black supported catalysts, but also exhibit lower platinum surface area losses and decreased particle sintering [148,177]. This has been attributed

to an interaction of the delocalized π electrons of graphene sheets, which can interact with and thus stabilize the platinum particles [26,136].

Further, the modified catalyst support interaction appears to have a beneficial influence on the catalytic activity towards methanol oxidation. In a comparative study of carbon black with defective and defect free CNTs Yoo et al. reported that catalysts supported on defect free CNTs were superior to defective and carbon black supported ones in both methanol electrooxidation and DMFC measurements [200]. The better performance of the defect free CNT supported catalyst was explained by an increase of CO oxidation activity and attributed to carbon surface states present on the defect free CNTs. The influence of the CNT support structure was further examined by Wu et al., showing that platinum catalysts supported on single wall carbon nanotubes (SWNTs) may even be superior to ones supported on MWNTs [191,192]. Their measurements showed a decreased onset potential for methanol oxidation as well as lower charge transfer resistances for catalysts supported on SWNTs. Another support based approach to increase the catalytic activity of CNT supported platinum catalysts towards methanol oxidation was presented by Maiyalagan et al. [102]. CNTs containing different amounts of nitrogen were synthesized by the decomposition of nitrogen containing organic precursor materials. When used as support materials for Pt catalysts, a higher catalytic activity towards methanol oxidation was observed for the nitrogen doped materials compared to undoped CNTs, indicating an influence of the nitrogen on the catalytic properties of the deposited platinum particles.

10.1. Catalyst Synthesis

Due to the quite hydrophobic surface of the CNTs and the low amount of surface groups, CNTs generally need to be activated before deposition of the catalyst particles to obtain uniform dispersions of noble metal particles on the surface of the tubes. Frequently an oxidative pre-treatment in concentrated HNO_3 or a mixture of HNO_3 with H_2SO_4 is used as surface activation step [51,92,126]. The oxidative treatment generates functional groups, such as OH, COOH, CO on the surface, which are believed to act as metal-anchoring sites

and to facilitate metal nuclei formation [22]. However, the oxidative treatment partially destroys the surface of the CNTs and as a consequence may lead to accelerated carbon corrosion and a deterioration of their electric conductivity.

Other approaches to create anchoring points for metal particle deposition consist in a chemical functionalization of the tube surface or the use of surfactants. Waje et al. described a functionalization of CNTs by reduction of diazonium salt on the tube surface [173]. In a second step the aryl functional groups were sulfonated with H_2SO_4 to form sulfonic acid groups, where Pt ions can adsorb. The use of a combined oxidation and surfactant treatment with tetraoctylammonium bromide as surfactant for the synthesis of MWNT supported PtRu catalysts by $NaBH_4$ reduction was recently described by Prabhuram et al. [126]. However, application of surfactants for catalyst synthesis is rare. In contrast, several authors reported the effective use of surfactants to obtain homogeneous coatings of CNTs with inorganic oxidic or sulfidic materials, such as TiO_2 or ZnS [33,34,74,204]. For the coating of CNTs with TiO_2 Eder et al. reported the use of benzylalcohol, which can adsorb to the CNTs by π–π interaction between the aromatic CNT surface and the benzyl ring of benzylalcohol [34]. However, Zhao et al. proved by zeta potential measurements that sodium dodecyl sulfate (SDS), although containing no aromatic parts, also forms a rather stable adsorbate on the CNT surface over a wide pH range [204].

Coating of CNTs with ruthenium oxide has also been reported in literature [4,79]. However, those coatings were intended for supercapacitor applications rather than fuel cells. The coating techniques described include the adsorption of hydrous ruthenium oxide from a solution of $RuCl_3 \cdot 3H_2O$ in isopropanol and water on CNTs pretreated with HNO_3 [4] and electrodeposition, also from a $RuCl_3$ solution [79]. Coating by the former method appeared to be highly ineffective as the authors report that only about 1 wt. % of Ru was deposited onto the CNTs, while a weight ratio of 1:0.5 (CNT to Ru) was used in solution. For this reason and to keep the synthesis close to that of the non-CNT supported hydrous RuO_2 catalyst, a modified controlled precipitation process was used to coat the CNTs with hydrous RuO_2.

Since $NaBH_4$ reduction, which was previously used to deposit platinum on the hydrous RuO_2, had been described by several authors to yield only poor particle

dispersions with a high degree of agglomeration on carbon supports including CNTs [22,65], an alternative reduction method was applied for platinum deposition on the hydrous RuO_2 coated CNTs. Ethylene glycol was chosen for this purpose, as this rather simple method is well known to produce uniformly distributed catalyst particles with narrow size distributions [116]. Further, ethylene glycol is a rather mild reducing agent which cannot reduce Ru ions at the same reaction conditions as platinum [22].

10.2. EXPERIMENTAL

Pretreatment of the Carbon Nano Tubes

Multi walled carbon nano tubes, obtained from a lab at Tsinghua University, were purified by refluxing in 2 M HCl for 48 hours to remove impurities from residual growth catalysts. The purified CNTs were ultrasonically dispersed in a 1% sodium dodecyl sulfate (SDS) solution for about 1 hour and stirred overnight to obtain well dispersed, functionalized tubes. Thereafter, the tubes were filtered and washed two times with deionized water and were dried at 70 °C for 24 h.

Coating with $RuO_2 \cdot x\, H_2O$

The same oxidant-aided co-precipitation technique, described in section 9.2.2 was used to coat the SDS functionalized CNTs with hydrous RuO_2.

CNTs coated with different amounts of hydrous RuO_2 were prepared by this technique to obtain catalysts with various Pt to $RuO_2 \bullet x\, H_2O$ ratios.

Platinum deposition

Platinum deposition onto the hydrous RuO_2 coated CNTs was carried out with two different reducing agents. The first set of catalysts was prepared by reducing H_2PtCl_6 in aqueous solution by dropwise addition of $NaBH_4$, as described for

the catalyst supported on pure hydrous RuO_2 in section 9.2.2. Ethylene glycol reduced catalysts were obtained by suspending the as-prepared RuO_2 coated CNTs in 50 mL of ethylene glycol. Then 410 µl of 0.2 M H_2PtCl_6 was added under vigorous stirring to the mixture. The resulting slurry was refluxed at 140 °C for 3h to ensure complete reduction of H_2PtCl_6. The solid product was rinsed with deionized water repeatedly. Finally, the product was dried in vacuum at 70 °C for 10h.

All catalysts were prepared with the same nominal amount of platinum with a platinum to CNT mass ratio of 20 %. Using CNTs coated with various amounts of $RuO_2 \bullet x\ H_2O$ catalysts with molar Pt:Ru ratios of 1:2, 1:1 and 1:0.5 were synthesized. In addition, a Pt/CNT catalyst containing no hydrous RuO_2 coating was prepared as a reference by ethylene glycol reduction.

10.3. Structural Characterization

The catalysts prepared by $NaBH_4$ reduction of H_2PtCl_6 were analyzed by X-ray diffraction and transmission electron microscopy. The XRD patterns of the as-prepared catalysts were similar to those obtained for the catalysts supported on pure hydrous RuO_2. However, in addition to diffraction peaks of platinum, weaker diffraction peaks were observed, which could be attributed to the graphite like structure of the CNTs. Diffraction peaks of RuO_2 were not detected, indicating that the RuO_2 coating layer is mostly amorphous as expected for hydrous RuO_2. For all catalyst samples the average Pt particle size was determined by Rietveld refinement of their respective XRD patterns. The results of the Rietveld refinements are summarized in Table 10.1. The data reflect a clear dependence of the Pt particle sizes on the amount of hydrous RuO_2 used to coat the CNTs. The platinum particle size determined by XRD was largest for the CNTs coated with only a low amount of RuO_2. For higher RuO_2 contents a steady decrease of the Pt particle size was observed.

However, TEM analysis of the catalysts showed that the platinum particles were only poorly dispersed on the CNT support and that a large amount of platinum was highly agglomerated (Figure 10.1). The dispersion and agglomeration was

Table 10.1. *Average Pt particle sizes for the $NaBH_4$ reduced Pt/RuO_2/CNT catalysts determined by Rietveld refinement of XRD data.*

Pt:Ru ratio	*Particle size / nm*	*Lattice constant / Å*
1: 0.5	3.4(4)	3.91(3)
1: 1	3.2(2)	3.91(8)
1: 2	2.9(4)	3.91(0)

found to be largely independent of the hydrous ruthenium oxide content in the sample.

In contrast, the hydrous RuO_2 coating appeared to be rather homogeneously distributed, as can be seen by the light grey speckling of the CNTs in Figure 10.1. Higher resolution shots of the catalyst at parts, where the platinum particles were more homogeneously dispersed (Figure 10.2) showed mostly facetted particles of about 4-5 nm. The hydrous RuO_2 coating is barely visible at this magnification as it forms only a very thin granular film of about 1-2 nm.

Although the decrease of Pt particle size determined by XRD suggests the creation of additional nucleation sites by the hydrous RuO_2 coating, an improved dispersion of the Pt particles could not be observed by TEM. But the poor dispersion of the Pt particles seems not to be linked to an equally poor dispersion of hydrous RuO_2 on the CNTs, since the hydrous RuO_2 was observed to be fairly well distributed. The strong tendency for agglomeration of the Pt particles seems therefore solely linked to the reduction by $NaBH_4$, even more, since strong platinum agglomeration has also been reported by other authors for $NaBH_4$ reduced platinum catalysts on carbon [22,65]. Very recently, Hyun et al. reported a strong dependence of platinum agglomeration on the amount of $NaBH_4$ used during synthesis [65]. In their study, well dispersed catalysts were only obtained if the molar ratio of $NaBH_4$ to metal ions was raised above 5. The poor dispersion of platinum particles observed for the RuO_2/CNT supported catalysts therefore is most probably due to an insufficient amount of $NaBH_4$ used for the platinum deposition.

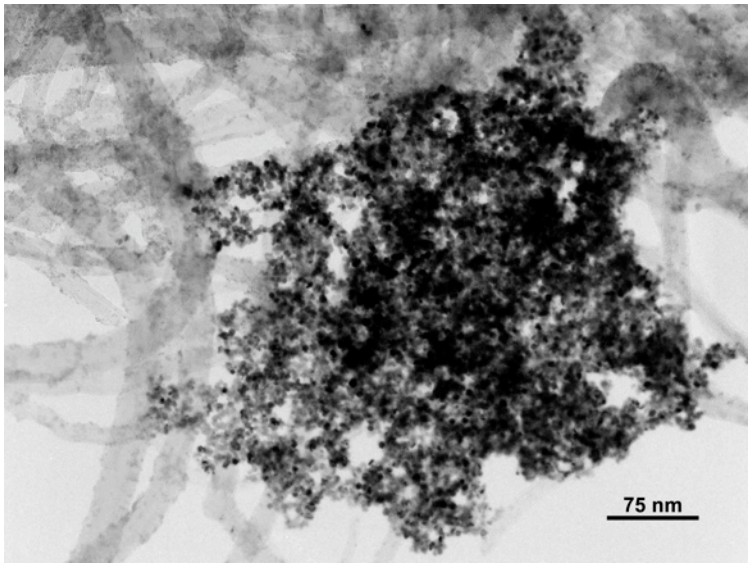

Figure 10.1. *TEM image of a Pt/RuO_2/CNT catalyst having a Pt:Ru ratio of 1:2 with platinum deposited by $NaBH_4$ reduction. The platinum particles are poorly distributed on the CNT support and have a high tendency for agglomeration.*

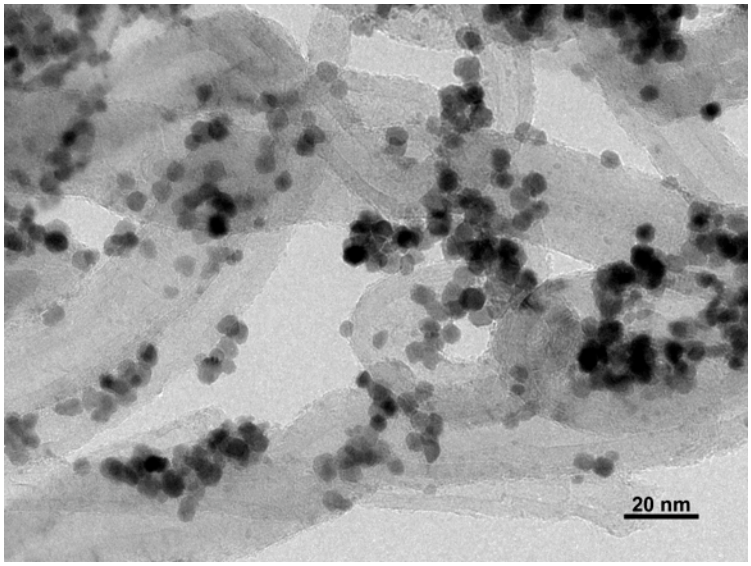

Figure 10.2. *TEM image of a Pt/RuO_2/CNT catalyst prepared by $NaBH_4$ reduction having a Pt:Ru ratio of 1:0.5. The platinum particles are about 4-5 nm in size and strongly facetted.*

Table 10.2. *Average Pt particle sizes for the ethylene glycol reduced Pt/RuO_2/CNT catalysts determined by Rietveld refinement of XRD data.*

Pt:Ru ratio	*Particle size / nm*	*Lattice constant / Å*
1 : 0	3.5(6)	3.91(9)
1 : 0.5	2.7(1)	3.92(8)
1 : 1	2.3(9)	3.91(4)
1 : 2	2.3(3)	3.91(0)

By XRD analysis of the ethylene glycol reduced catalysts the same trend of particle size reduction as reported for the $NaBH_4$ reduced catalysts, was observed. However, average particles sizes for the ethylene glycol reduced catalysts were 0.7-0.8 nm smaller than those obtained by $NaBH_4$ reduction (Table 10.2).

Also for the ethylene glycol reduced catalysts no diffraction peaks corresponding to RuO_2 or metallic Ru were observed. And although the XRD data reflects a slight decrease of the platinum lattice parameter with increasing RuO_2 content, this decrease is to small to be caused by significant alloying of Ru with Pt. Therefore, the XRD data suggested that the hydrous RuO_2 stays in its oxidized form also during platinum deposition with ethylene glycol. However, in order to verify the oxidation state of Ru in the sample, X-ray photoelectron spectra were recorded for the Pt/RuO_2/CNT catalyst containing platinum and RuO_2 in a molar ratio of 1.

Due to a very pronounced carbon 1s signal from the CNT support and carbonaceous impurities superimposed on the Ru 3d doublet, the Ru 3p signal had to be used for the analysis of the Ru oxidation state. Since the amount of RuO_2 on the tubes is rather low and the Ru 3p signal is considerably weaker than that of the Ru 3d orbitals, only a rather noisy Ru 3p signal was obtained. Due to the high noise level results obtained by fitting the spectra were ambiguous. Therefore, the spectrum was smoothed and the obtained peak profile was compared to Ru 3p

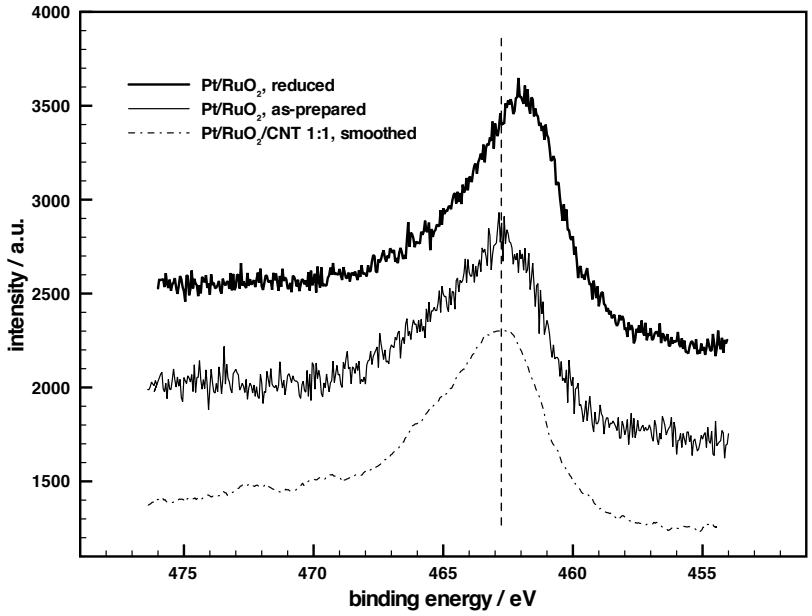

Figure 10.3. *Ru 3p XPS spectra for a ethylene glycol reduced $Pt/RuO_2/CNT$ catalyst and for an as-prepared and partially reduced Pt/RuO_2 catalyst prepared by $NaBH_4$ reduction.*

spectra recorded for the Pt catalyst supported on pure hydrous RuO_2 in its as-prepared and a partially reduced state. The partially reduced catalyst was obtained by treating the as-prepared catalyst in a stream of hydrogen at 100 °C for about 1 hour.

As can be seen from Figure 10.3, the Ru 3p profile of the ethylene glycol reduced catalyst strongly resembles that of the as-prepared catalyst obtained by $NaBH_4$ reduction, but not the reduced one. Hence, the XPS measurement confirms that Ru in the sample is mostly in an oxidized state and that alloying of Pt and Ru, if present, is low.

In contrast to the $NaBH_4$ reduced catalysts the platinum dispersion was found to improve considerably with the amount of hydrous RuO_2 coated on the CNTs. Figures 10.4 shows TEM images of two ethylene glycol reduced catalysts supported on plain CNTs and on hydrous RuO_2 coated CNTs, respectively. While

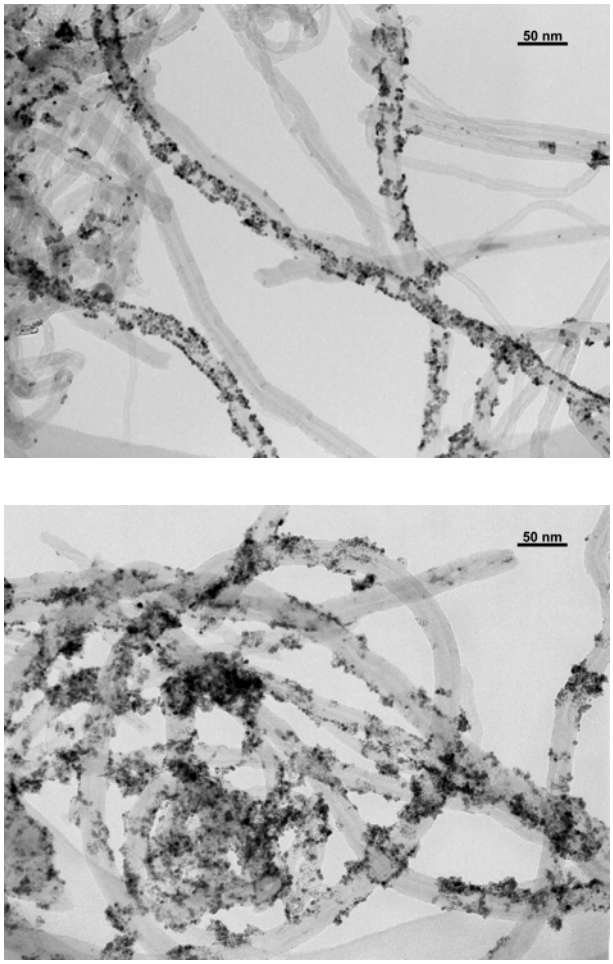

Figure 10.4. *TEM image of the pure Pt/CNT catalyst showing strong preferential deposition of platinum on single tubes (top); Pt/RuO_2/CNT catalysts (Pt:Ru ratio of 2:1) with significantly more uniform dispersion of the platinum particles (bottom).*

the platinum particles deposited on the uncoated tubes show highly preferential deposition on single tubes, deposition on the coated CNTs is much more homogeneous. However, also in this case agglomeration of the platinum particles is observed to a certain degree. High resolution imaging of single nanotubes indicated that this clustering of platinum particles might be caused by growth defects of the nanotubes (Figure 10.5).

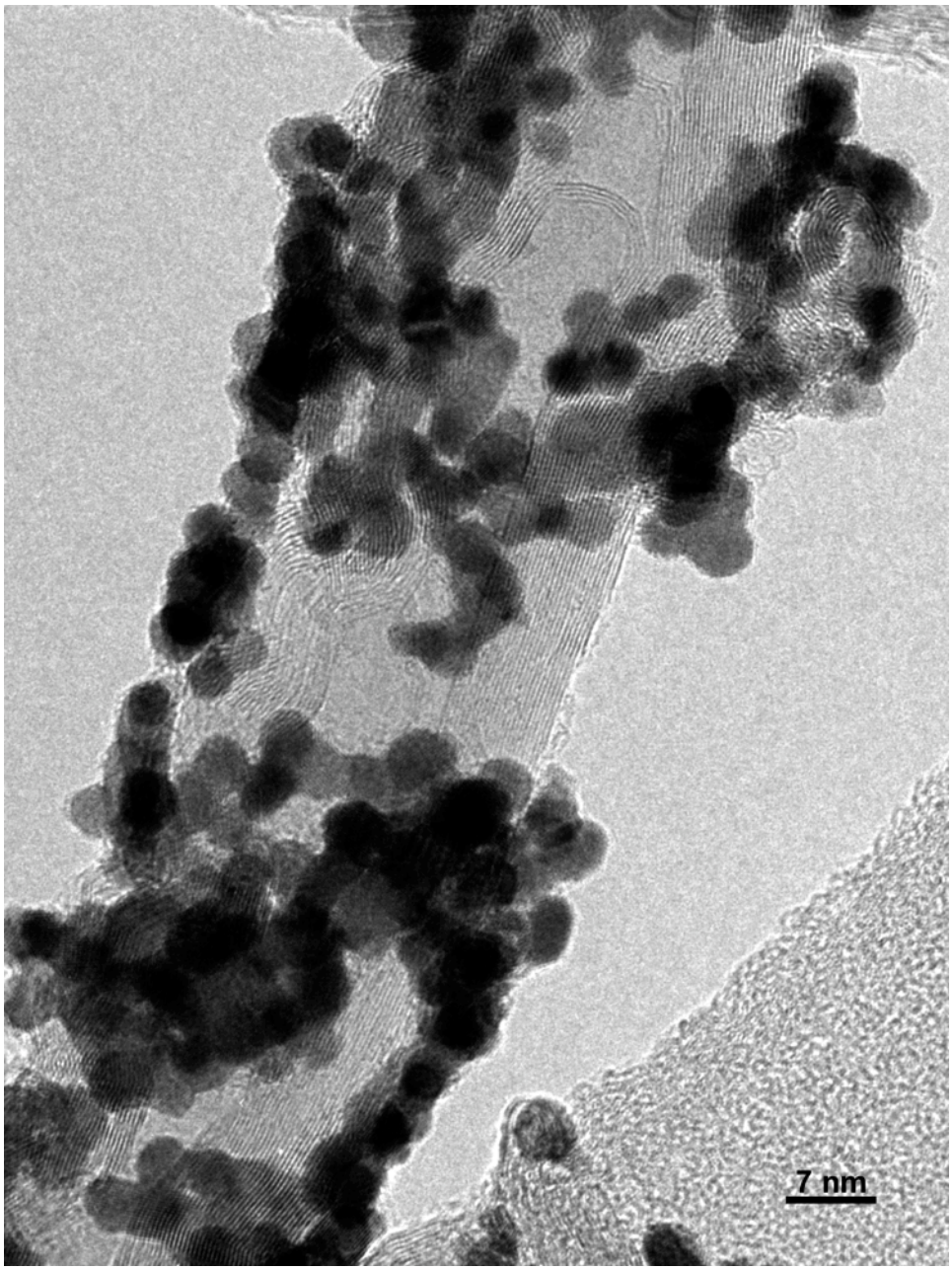

Figure 10.5. *High resolution TEM image of a single carbon nano tube coated with RuO_2 and platinum (Pt:Ru ratio of 2:1). The carbon nano tube contains a large number of growth defects. The image suggests that platinum deposition occurs preferentially at defect sites.*

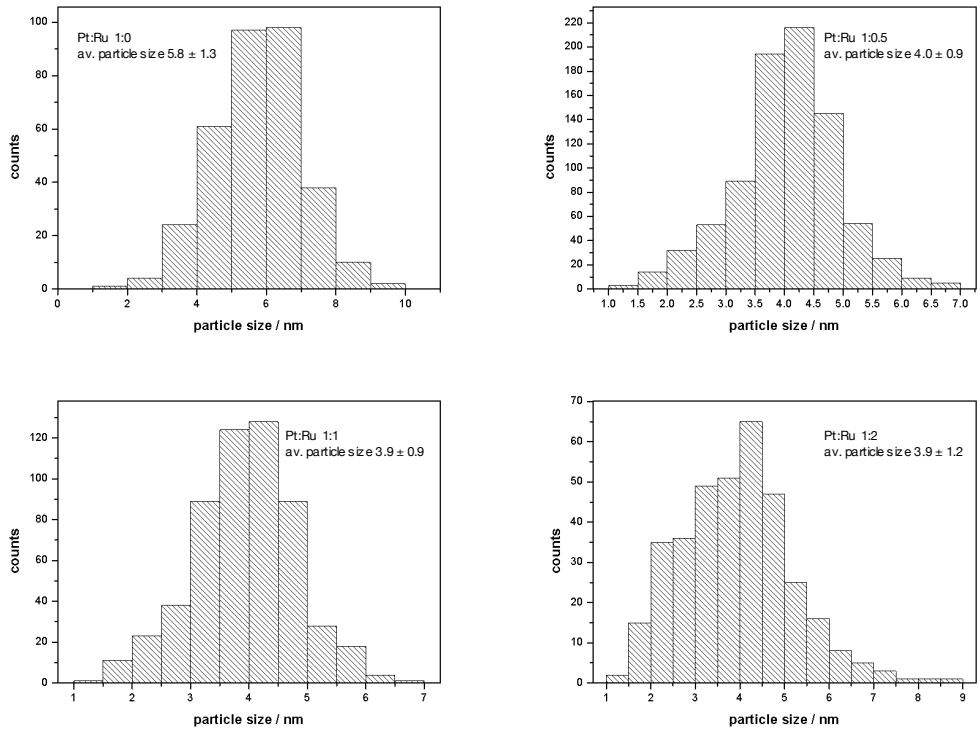

Figure 10.6. *Particle size distributions for the Pt/RuO_2/CNT catalysts reduced in ethylene glycol.*

The preferential deposition of platinum particles at sites of growth defects can be justified by the low amount of nucleation sites on perfectly grown CNTs. Nucleation sites on the nanotube surface are generally created by partially destroying the closed structure of the graphite layers by strongly oxidizing agents like HNO_3. Defect sites on the tube surface are easier to oxidize and consequently contain a higher number of nucleation sites.

Evaluation of particle sizes obtained from measuring individual particles in TEM images reproduced the same trend of decreasing average particle sizes with increasing RuO_2 content as was obtained by the XRD measurements.

The determined particle size distributions were largely symmetric, except for the catalyst with the highest RuO_2 content, whose particle size distribution becomes slightly asymmetric at the lower end (Figure 10.6).

The particle shape of the platinum particles differed from that obtained for the $NaBH_4$ reduced catalyst, being more round shaped without visible faceting. Most particles deviated slightly from a perfect spherical shape, having one slightly elongated axis. To determine the average aspect ratio of the particles, the width and height of the particles was determined independently for about 600 particles. An average aspect ratio of 0.83 with a standard deviation of 0.08 was obtained for these particles. Comparison of aspect ratios obtained for catalysts with different amounts of RuO_2 yielded highly similar values and showed no correlation with the RuO_2 content.

Since the hydrous RuO_2 is supposed to provide a proton conducting path along the tube surface as well as a promotion of the methanol oxidation by supplying OH species to the platinum catalyst, a homogeneous coating on the CNT surfaces is desired. The catalyst containing the lowest amount of RuO_2 showed only incomplete coating of the nanotube surfaces and little to no hydrous RuO_2 was visible on sites occupied by clusters of Pt particles (Figure 10.5).

The catalysts having molar ratios exceeding 1:1 showed an almost complete coverage of the tube surface. Further, a considerable amount of Pt particles covered by a thin layer of amorphous RuO_2 can be observed (Figure 10.7). This means, that either the hydrous RuO_2 is not a completely solid phase and is able to „creep“ onto the Pt particles after the deposition step or, that nucleation and growth of the Pt particles occur beneath the RuO_2 coating. In either case, the hydrous RuO_2 coating on the platinum particles may play a significant role for the electrooxidation of methanol, either by directly providing OH species for CO oxidation or by becoming electrochemically reduced to metallic ruthenium creating Ru decorated platinum particles, which provide OH species by water activation according to the bifunctional mechanism.

The TEM analysis of the dispersed catalyst powder samples indicated a rather homogeneous distribution of both hydrous RuO_2 and platinum particles on the tube surface. However, it should be noted, that TEM on dispersed powder samples can only be used to analyze a rather small fraction of the sample. More ex-

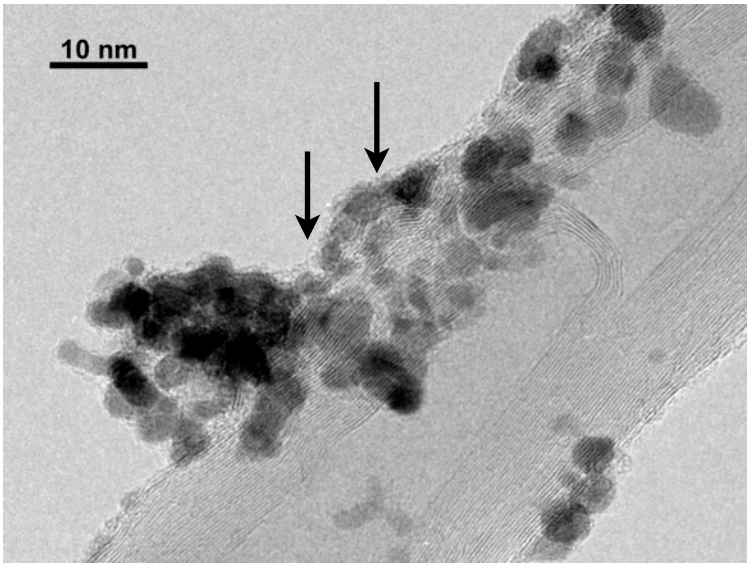

Figure 10.7. *High resolution TEM image of the ethylene glycol reduced Pt/RuO_2/CNT catalyst (molar Pt:RuO_2 ratio 1:2). The platinum particles and the CNT surfaces are almost completely covered by a thin amorphous layer of RuO_2 (indicated by arrows in the image).*

plicitly, due to particle agglomeration and restrictions for the maximum sample thickness imposed by scattering and absorption of the electron beam, usually only at some exterior parts of the catalyst agglomerates can be analyzed by TEM.

Also the CNT supported catalysts possessed a considerable tendency for agglomeration forming large coiled aggregates, which frequently exceeded 1 µm (Figure 10.8). To verify, whether the Pt and RuO_2 distribution inside the agglomerated CNTs parallels the rather homogeneous distribution observed in the TEM images of the dispersed powder samples, the thin-section approach, used for the characterization of PEFC electrodes, was adapted to the dispersed catalyst samples. To the author's knowledge, there are no other sources in literature reporting a similar approach for the characterization of dispersed catalyst samples.

To obtain thin-sections of the catalyst, a mixture of the catalyst powder and the embedding resin was prepared and cured at 60 °C for 16 hours. Thereafter, the polymerized sample was trimmed and sectioned using an ultra-microtome.

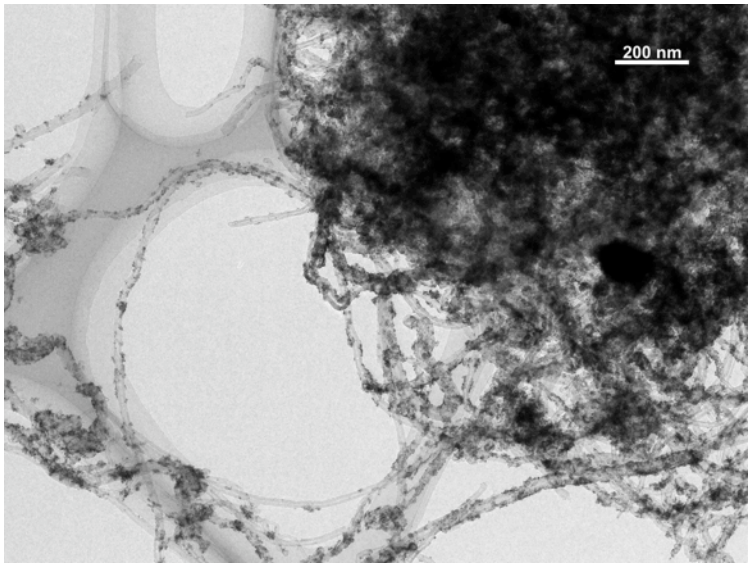

Figure 10.8. *Low resolution TEM images of a CNT supported platinum catalyst. The CNTs of the catalysts are strongly coiled together to form beads of up to several micrometer in diameter.*

SE and BSE images (Figure 10.9) of the thin-sections revealed that the catalyst distribution inside the catalyst agglomerates and in the exterior parts differs considerably. From the BSE image of the catalyst thin-section it is clearly visible that the agglomerate cores contain significantly less noble metal catalyst. The more uniform SE signal, obtained from these agglomerate cores, gives a first indication that the preferential deposition of the noble metal catalyst to the outer parts is due to a denser packing of CNTs.

Since the separate deposition steps for RuO_2 and the Pt may result in different distributions on the supporting CNTs, element maps for platinum and ruthenium were recorded by EDX (Figure 10.10). Both distributions are largely similar, with platinum and ruthenium mostly located in the outer parts of the agglomerates. However, ruthenium or rather the hydrous RuO_2 penetrates slightly deeper into the CNT coils and a weak Ru signal can also be detected from some agglomerate cores, while platinum seems to be exclusively located in the outer parts.

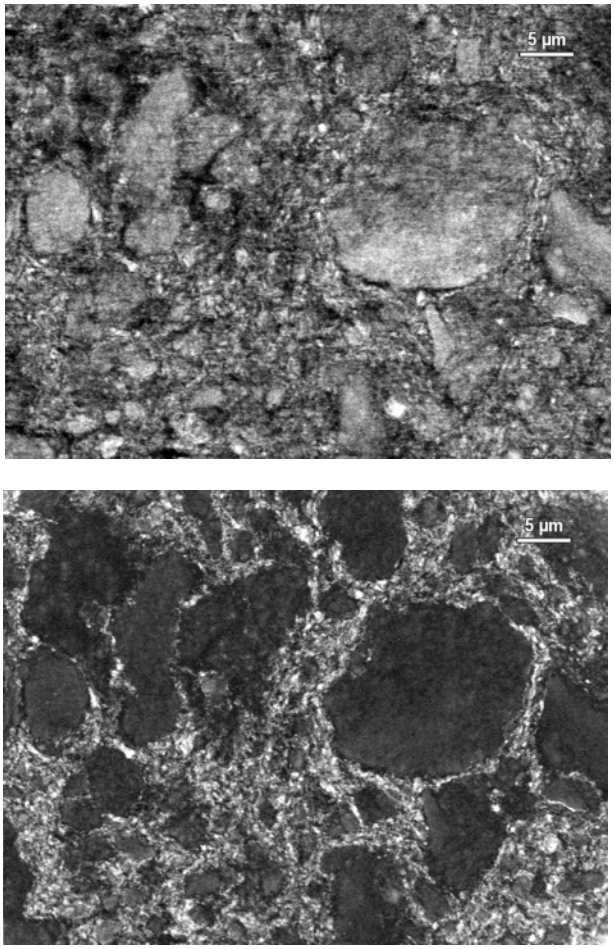

Figure 10.9. *SE (top) and BSE (bottom) image of a thin-section through a Pt/RuO_2/CNT catalyst embedded in epoxy resin.*

As a consequence, it must be concluded, that the sonication and SDS treatment were not sufficient to fully disperse the CNTs and that their strong agglomeration resulted in a highly preferential deposition on the outer parts of the agglomerates.

Despite the preferential deposition of platinum and RuO_2, electrochemical measurements performed by the project partners and published recently [17] yielded excellent electrochemical activities for both methanol and CO oxidation

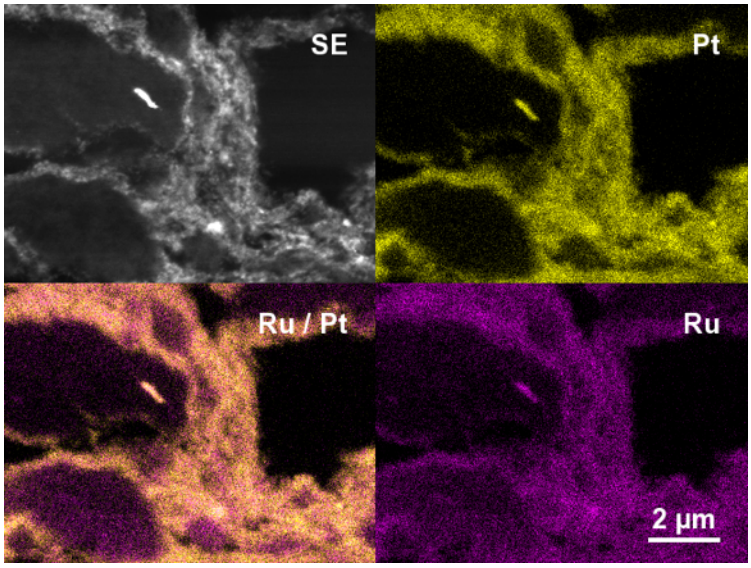

Figure 10.10. *Element maps of platinum and ruthenium obtained by EDX mapping of a thin-section through a Pt/RuO_2/CNT catalyst embedded in epoxy resin.*

when compared to a commercial PtRu/C catalyst (E-TEK) with a similar noble metal loading and Pt:Ru ratio. Onset potentials for methanol oxidation were rather similar for both catalysts, demonstrating that the hydrous RuO_2, used to coat the CNTs, takes part in the electrochemical oxidation of methanol.

10.4. Conclusion

Platinum catalysts supported on hydrous RuO_2 coated CNTs were prepared by two different reduction methods and analyzed by XRD, TEM, XPS and SEM. The hydrous RuO_2 was found to coat the CNT surfaces rather homogeneously. However, strong agglomeration of platinum particles was observed for the $NaBH_4$ reduced catalyst, while reduction with ethylene glycol resulted in a more uniform dispersion. For catalysts prepared by ethylene glycol reduction an improvement of the catalyst dispersion was observed with increasing RuO_2 content. Slightly smaller platinum particle sizes were obtained by the ethylene glycol

method than by $NaBH_4$ reduction. It could be shown that at hydrous RuO_2 contents exceeding a molar ratio of Pt:RuO_2 of 1:1, a thin layer of hydrous RuO_2 was covering the platinum particles. This observation may explain the high activity of the catalysts for the electrooxidation of methanol, which was similar or even superior to alloyed PtRu/C catalysts.

However, analysis of embedded catalyst thin-sections revealed a „core-shell"-like structure of the catalyst agglomerates, having a considerably higher amount of catalyst deposited on the outer parts of the agglomerates.

II. MEAs Made of Pt/RuO_2/CNT Catalysts

II.I. Structure of the catalyst network

To examine influences of the preparation process on the electrode structure, MEAs prepared of an ethylene glycol reduced Pt/RuO_2/CNT catalyst with a molar Pt:RuO_2 ratio of 1:1 by the project partner from the ZAE Bayern, where analyzed by scanning and transmission electron microcopy of thin and ultra-thin sections obtained by microtomy. The MEAs were prepared by dispersing the catalyst in a mixture of isopropanol, water and Nafion solution (5 wt. %) for 3 days using a magnetic stirrer. The catalyst inks were then directly sprayed onto a heated Nafion membrane (100 °C) and cured at 145°C for about 1 hour.

SEM micrographs of two electrode thin-sections (Figure 11.1) demonstrate a strong influence of the ink concentration on the electrode structure. The electrode shown in the left image was prepared with a significantly lower amount of solvent resulting in a more viscous ink than the electrode displayed in the image on the right. Also in the electrode structure the „core-shell"-like structure of the catalyst agglomerates is partially maintained. However, the size of the agglomerate particles is considerably reduced for the electrode from the ink of lower viscosity, demonstrating that the catalyst agglomerates are broken up by the ink preparation process and that a lower viscosity of the ink is beneficial for this process.

Apart from the differences in agglomerate size, both electrodes show a similar layered morphology. The direction of this layering was observed to be mostly parallel to the membrane. This implies that the layered morphology of the electrode is a consequence of the coating process which favors an in plane alignment of the CNTs or aggregates thereof due to their shape anisotropy.

However, TEM microscopy of the electrode structure (Figure 11.2) still shows a high amount of randomly aligned CNTs, demonstrating that the layering is rather a collective phenomena of CNT bundles with varying catalyst loading.

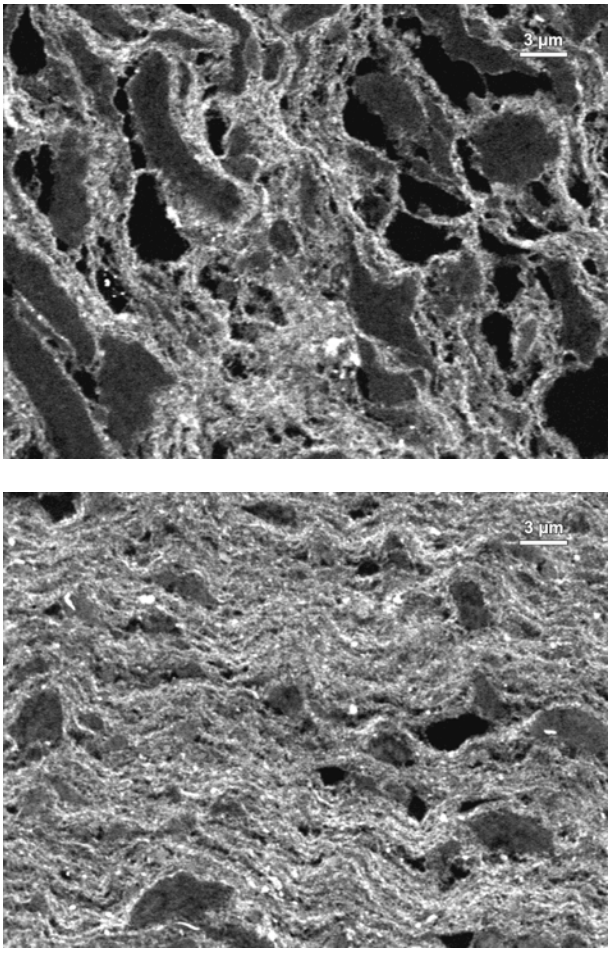

Figure 11.1. *BSE images of two electrode layers made of the same CNT-supported catalyst but with different dispersion of the catalyst in the ink.*
Top image: Poorly dispersed catalyst. Large agglomerates and pores dominate the electrode structure.
Bottom image: Agglomerates are much reduced in size and the catalyst appears to be more homogeneously distributed.

This view is also more consistent with the SEM images of the electrode layer (Figure 11.1), showing layer thicknesses of several hundred nanometer rather than 20-50 nm, corresponding to the diameter of a single tube.

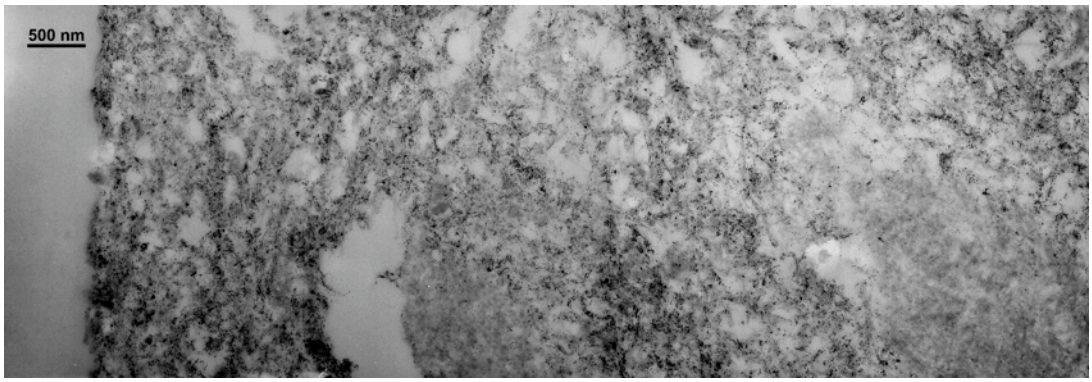

Figure 11.2. *TEM image of an ultra-thin-section through an electrode prepared of a Pt/RuO_2/CNT catalyst (molar Pt:RuO_2 ratio 1:1). The left side of the image shows a part of the membrane.*

11.2. Polymer Electrolyte Distribution

To examine the effect of the fibrous CNT network on the polymer electrolyte distribution an EDX mapping of fluorine was recorded of an electrode thin-section. The mapping is shown in Figure 11.3 along with the corresponding SE and BSE images as well as mappings for carbon (C), platinum (Pt) and ruthenium (Ru).

In the lower part of the image a piece of the membrane is visible. Due to the considerably higher fluorine signal of the membrane, a log-transform of the image was necessary to remap the fluorine signal of the electrode to discernible brightness values. The fluorine signal of the electrode is mostly uniform, displaying only voids, where pores are located in the electrode. Only in a small region close to the membrane, a slightly higher fluorine concentration can be observed. Although it cannot be ruled out completely, that the higher fluorine signal is caused by smearing of polymer electrolyte from the membrane into the electrode during sectioning, smearing seems unlikely. Even if smearing of the membrane should occur, the resultant polymer electrolyte film on the membrane would be only a few nanometer at most. A section thickness of about 200 nm provided and considering that the fluorine signal is collected from the complete volume, a thin film of smeared polymer electrolyte would hardly contribute to a noticeable change of the collected fluorine signal. Therefore, it seems more likely

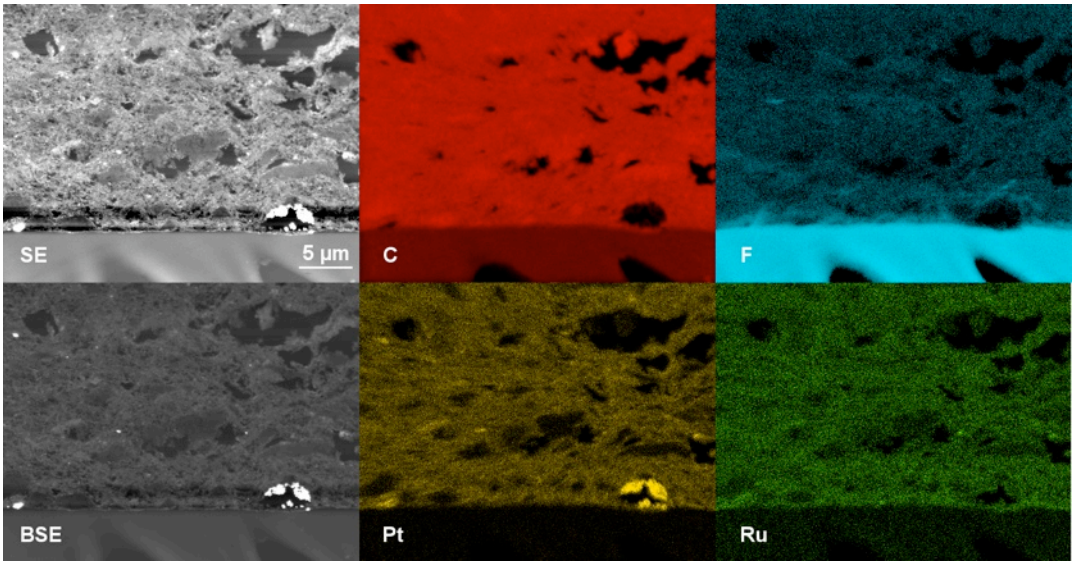

Figure 11.3. *Elemental maps of carbon (C), fluorine (F), platinum (Pt) and ruthenium (Ru) as well as corresponding SE and BSE micrographs of a Pt/RuO_2/CNT based electrode.*

that the higher fluorine signal is caused by segregation of the polymer electrolyte at the membrane electrode interface.

The observation, that the polymer electrolyte infiltrates the CNT network of the electrode almost homogeneously, could also be confirmed by TEM. Figure 11.4 shows a zero-loss filtered image of the electrode structure. The image shows that the CNT supported catalyst is largely embedded in a matrix of polymer electrolyte. However, still a significant number of pores, visible as light grey patches in the image, exist in the electrode layer. Compared to the electrode structures of the carbon black supported catalysts, characterized in chapter 8–11, the CNT supported catalyst seem to provide a more open network while at the same time displaying excellent connectivity to the polymer electrolyte. This demonstrates, that the CNT based catalysts indeed provide an electrode structure which should possess outstanding transport properties for protons, electrons and reactants.

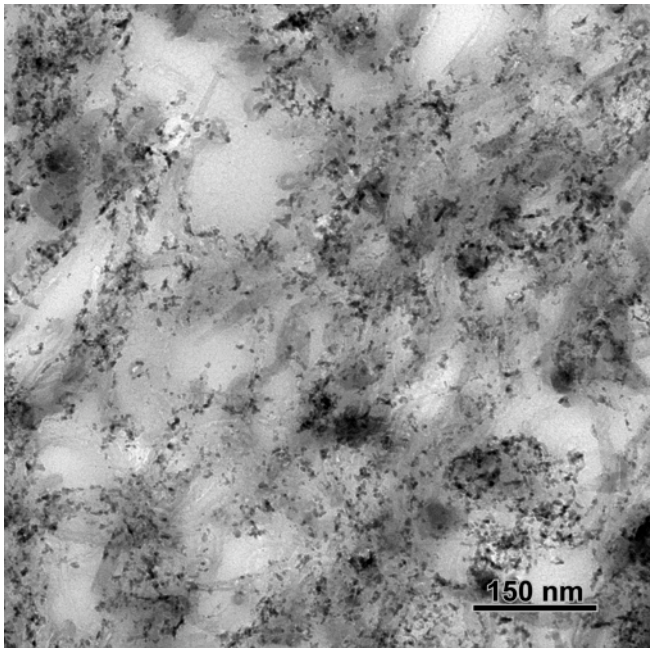

Figure 11.4. *Zeroloss filtered TEM image of a part of a Pt/RuO_2/CNT electrode. The CNT supported catalyst is almost completely covered by the polymer electrolyte.*

11.3. Conclusion

Depending on the catalyst concentration in the ink, the „core-shell"-like structure of the catalyst agglomerates was more or less strongly preserved in the electrode structure of the Pt/RuO_2/CNT catalysts. However, even in well dispersed electrodes remaining agglomerates were observed. In addition, the electrodes exhibited a layered structure, due to alternating layers of variably loaded CNT bundles.

The polymer electrolyte was rather uniformly dispersed in the complete electrode layer showing only a slight segregation effect near the membrane-electrode interface. TEM analysis showed a high interconnectivity between the different transport phases, which should provide excellent conditions for fast transport of protons, electrons and reactants.

Part 6

Final Conclusion & Outlook

12. Final Conclusion & Outlook

The electrode of a PEFC is a complex nanostructured composite material containing a supported catalyst, a polymer electrolyte and pores. The complexity of its structure, composed of amorphous organic and inorganic material as well as nanometer sized crystalline catalyst particles and pores, which arrange to larger agglomerated or aggregated structures in the micrometer range, makes its characterization a highly challenging task.

This work presented new approaches for the characterization of such complex composite structures based on ultra-microtomed electrode thin-sections and electron microscopy. Applying these methods to PEFC electrodes fundamental insight on their structure could be obtained, which may contribute to improve the current understanding of transport processes in the electrode.

On the experimental side several obstacles needed to be overcome to characterize the electrode including all its structural parts. These were:

- Weak contrast between the different structural parts composing the electrode.
- The sensitivity of the polymer electrolyte material towards radiation damage, causing fluorine loss when exposed to the electron beam of the microscope.
- The highly random nature of the electrode structure with structural features spanning a wide range of different length scales from a few nanometer up to several micrometer.

In order to resolve these issues, a computer assisted acquisition procedure for energy-filtered TEM (EF-TEM) was developed, which significantly enhances the capabilities of standard post-column imaging filters. To address the limited field of view of these instruments, the acquisition procedure was designed to acquire a sequence of shifted images covering an up to 10 times larger sample area. Shifting was realized by a virtual translation of the sample area by modifying the electron beam path through the beam and image deflection systems of the microscope. This novel approach allowed fast and highly accurate positioning of the image sample area and minimized beam exposure of the specimen therefore ef-

fectively reducing beam induced radiation damage of the specimen. Furthermore, an online drift monitoring and drift compensation system was implemented, which led to a significant reduction of artifacts caused by drift of the specimen. In addition, several image post-processing routines were developed to automatically align sets of shifted images and to compute elemental maps from energy filtered images according to the three window method.

Furthermore, contrasting methods commonly used for biological specimens were adapted to the characterization of PEFC electrodes and catalyst polymer electrolyte dispersions. By the use of these methods the following results about the structure of the electrode layer in PEFC fuel cells were obtained:

- The amount of polymer electrolyte found in the pores between the catalyst agglomerates is low for electrodes with a composition close to the reported optimum Nafion concentration,
- The polymer electrolyte in the pores increases significantly when the polymer electrolyte concentration is raised above this value indicating that the amount of polymer electrolyte which can be adsorbed in the catalyst agglomerates is limited.
- Further, it was demonstrated that the polymer electrolyte in the pores does not form a continuously dense coating layer on the surface of the agglomerates, but forms fibrillar and film like structures in the complete pore space.
- With the aid of fluorine mapping, polymer structures observed in partially infiltrated samples could be unambiguously identified as polymer electrolyte. In addition the fluorine maps of the electrode provided strong indication for infiltration of the catalyst agglomerate particles by the polymer electrolyte.

In addition to the polymer electrolyte loading, influences of the solvent and the catalyst support were studied. For the analysis of the influence of the solvent used during electrode preparation, electrode thin sections as well as catalyst polymer electrolyte dispersions were investigated by electron microscopy. It could be shown, that the colloids formed by the polymer electrolyte in weakly polar solvents possess a high shape stability, leading to porous aggregated poly-

mer electrolyte structures. In contrast to more polar solvents, where the electrolyte is in a well dispersed form, the bead like colloidal shape largely prevents penetration of the polymer electrolyte into the agglomerate particles.

Complementing the analysis of electrodes made of standard carbon black supported catalysts, the electrode structure of carbon nanotube supported catalysts developed in cooperation with a Chinese partner from Tsinghua University (Beijing) were investigated. The catalysts consisted of hydrous ruthenium oxide coated carbon nanotubes decorated with platinum particles. The structure of the electrodes prepared of these catalysts was considerably different than that of the carbon black supported catalysts. The carbon nanotubes in the electrode formed a significantly less dense network, which was well penetrated by the polymer electrolyte. Analysis of the electrode structure further revealed a strongly non uniform distribution of the platinum and ruthenium oxide. The non uniform distribution could be attributed to preferential deposition of platinum and ruthenium oxide on the outer parts of carbon nanotube agglomerates during catalyst synthesis. As this effect was not observed by standard TEM analysis of the catalysts, this result also highlights the importance of thin-section approach for catalyst development.

Outlook

This work provides major contributions to the field of materials characterization in general and PEFC fuel cell research in particular. Contributions to the field of materials characterization include:

- The development of an automated image acquisition system for EF-TEM which largely improves the characterization of beam sensitive materials and significantly extends the imageable sample area by a highly accurate virtual sample shift procedure.
- The development of an automated image alignment procedure compatible with the EF-TEM image acquisition system and image processing procedures to construct elemental maps from energy filtered images which effectively reduce image noise and artifacts caused by sample drift.

- The adaption of a negative staining technique used mainly in biology for the characterization of viruses, proteins and cell structures to catalyst and polymer electrolyte dispersions used in the preparation process of the electrodes.

Although these developments were motivated by the characterization of PEFC electrode structures, they may be easily transferred to other material systems, having similar complex composite structures or high beam sensitivity. Therefore, this part of the work provides a bridge to other fields of materials research like polymer compounds or biological and medicinal specimen characterization.

In the field of fuel cell research, the work addressed some fundamental questions concerning the distribution and structure of the polymer electrolyte in the electrode layer, its ability to penetrate into the catalyst agglomerate particles and interactions between the polymer electrolyte taking place in the liquid phase of the catalyst ink.

The work presented is of significant relevance to the scientific community, as, to the authors knowledge, it is the first to provide a complete analysis of the electrode structure involving all major structural parts: the catalyst/catalyst support network, the pore structure as well as the distribution and structure of the polymer electrolyte.

Although a direct correlation between the experimentally determined structures of the electrode and its mass or proton transport properties could not be established during this work, the findings on the electrode structure may significantly improve the understanding of transport processes in the electrode, including transport of ionic species, transport of reactants and transport of water, if used to refine models of the electrode structure. In this respect a collaboration with the Flow Physics and Computation Group from the Department of Mechanical Engineering at Stanford University (California) has been established, with the aim of developing more realistic three-dimensional electrode models based on the experimental data of this work.

Ultimately, these efforts may lead to improved electrode structures facilitating mass and proton transport and hence lead to more efficient fuel conversion in the cell.

BIBLIOGRAPHIE

(1) T. Akita, A. Taniguchi, J. Maekawa, Z. Sirorna, K. Tanaka, M. Kohyama, and K. Yasuda, *Analytical TEM study of Pt particle deposition in the proton-exchange membrane of a membrane-electrode-assembly*, Journal of Power Sources, vol. 159, **2006**, p. 461-467.

(2) P. Aldebert, B. Dreyfus, and M. Pineri, *Small-Angle Neutron-Scattering of Perfluorosulfonated Ionomers in Solution*, Macromolecules, vol. 19, **1986**, p. 2651-2653.

(3) E. Antolini, *Formation of carbon-supported PtM alloys for low temperature fuel cells: a review*, Materials Chemistry and Physics, vol. 78, **2003**, p. 563-573.

(4) G. Arabale, D. Wagh, M. Kulkarni, I. Mulla, S. Vernekar, K. Vijayamohanan, and A. Rao, *Enhanced supercapacitance of multiwalled carbon nanotubes functionalized with ruthenium oxide*, Chemical Physics Letters, vol. 376, **2003**, p. 207-213.

(5) A. Arico, G. Monforte, E. Modica, P. Antonucci, and V. Antonucci, *Investigation of unsupported Pt-Ru catalysts for high temperature methanol electro-oxidation*, Electrochemistry Communications, vol. 2, **2000**, p. 466-470.

(6) P.W. Atkins, *Physical Chemistry*, Oxford University Press, 6th rev. Edition, **1998**, p. 960.

(7) L. Austin, M. Ariet, R.D. Walker, G. Wood, and R. Comyn, *Simple-Pore and Thin-Film Models of Porous Gas Diffusion Electrodes*, Industrial & Engineering Chemistry Fundamentals, vol. 4, **1965**, p. 321-327.

(8) G. Ayala and J. Domingo, *Spatial size distributions: Applications to shape and texture analysis*, IEEE Transactions on Pattern Analysis and Machine Intelligence, vol. 23, **2001**, p. 1430-1442.

(9) V. Bagotzky, Y. Vassiliev, and O. Khazova, *Generalized scheme of chemisorption, electrooxidation and electroreduction of simple organic compounds on platinum group metals*, Journal of Electroanalytical Chemistry, vol. 81, **1977**, p. 229-238.

(10) D. Bernardi and M. Verbrugge, *A Mathematical-Model of the Solid-Polymer-Electrolyte Fuel-Cell*, Journal of the Electrochemical Society, vol. 139, **1992**, p. 2477-2491.

(11) H. Berthiaux, V. Mosorov, L. Tomczak, C. Gatumel, and U. Demeyre, *Principal component analysis for characterising homogeneity in powder mixing using image processing techniques*, Chemical Engineering and Processing, vol. 45, **2006**, p. 397-403.

(12) D. Blom, J. Dunlap, T. Nolan, and L. Allard, *Preparation of cross-sectional samples of proton exchange membrane fuel cells by ultramicrotomy for TEM*, Journal of the Electrochemical Society, vol. 150, **2003**, p. A414-A418.

(13) C. Bock, A. Collier, and B. MacDougall, *Active form of Ru for the CH_3OH electro-oxidation reaction*, Journal of the Electrochemical Society, vol. 152, **2005**, p. A2291-a2299.

(14) C. Bock, M. Blakely, and B. MacDougall, *Characteristics of adsorbed CO and CH_3OH oxidation reactions for complex Pt/Ru catalyst systems*, Electrochimica Acta, vol. 50, **2005**, p. 2401-2414.

(15) C. Bock and B. MacDougall, *Novel method for the estimation of the electroactive pt area*, Journal of the Electrochemical Society, vol. 150, **2003**, p. E377-E383.

(16) S. Palous and R. Buvet, *Reduction de l'oxygene aux electrodes de piles à combustibles à basse temperature .1. réduction à la ligne de contact triple - electrode-electrolyte-gaz*, Bulletin de la Societe Chimique de France, **1962**, p. 1602-&.

(17) L. Cao, F. Scheiba, C. Roth, F. Schweiger, C. Cremers, U. Stimming, H. Fuess, L.Q. Chen, W.T. Zhu, and X.P. Qiu, *Novel nanocomposite Pt/RuO2 center dot xH(2)O/carbon nanotube catalysts for direct methanol fuel cells*, Angewandte Chemie-International Edition, vol. 45, **2006**, p. 5315-5319.

(18) C. Chen and C. Tsao, *Characterization of electrode structures and the related performance of direct methanol fuel cells*, International Journal of Hydrogen Energy, vol. 31, März. **2006**, p. 391-398.

(19) Z. Chen, X. Qiu, B. Lu, S. Zhang, W. Zhu, and L. Chen, *Synthesis of hydrous ruthenium oxide supported platinum catalysts for direct methanol fuel cells*, Electrochemistry Communications, vol. 7, **2005**, p. 593-596.

(20) X. Cheng, L. Chen, C. Peng, Z. Chen, Y. Zhang, and Q. Fan, *Catalyst microstructure examination of PEMFC membrane electrode assemblies vs. time*, Journal of the Electrochemical Society, vol. 151, **2004**, p. A48-A52.

(21) X. Cheng, B. Yi, M. Han, J. Zhang, Y. Qiao, and J. Yu, *Investigation of platinum utilization and morphology in catalyst layer of polymer electrolyte fuel cells*, Journal of Power Sources, vol. 79, **1999**, p. 75-81.

(22) C. Chien and K. Jeng, *Effective preparation of carbon nanotube-supported Pt-Ru electrocatalysts*, Materials Chemistry and Physics, vol. 99, **2006**, p. 80-87.

(23) M. Chisaka and H. Daiguji, *Effect of glycerol on micro/nano structures of catalyst layers in polymer electrolyte membrane fuel cells*, Electrochimica Acta, vol. 51, **2006**, p. 4828-4833.

(24) S. Cho, E. Cho, I. Oh, H. Kim, H. Ha, S. Hong, and J. Ju, *Surface modified Nafion® membrane by ion beam bombardment for fuel cell applications*, Journal of Power Sources, vol. 155, **2006**, p. 286-290.

(25) G. Cody and A. Davis, *Direct Imaging of Coal Pore-Space Accessible to Liquid-Metal*, Energy & Fuels, vol. 5, **1991**, p. 776-781.

(26) F. Coloma, A. Sepulvedaescribano, and F. Rodriguezreinoso, *Heat-Treated Carbon-Blacks as Supports for Platinum Catalysts*, Journal of Catalysis, vol. 154, **1995**, p. 299-305.

(27) W. Conner and J. Falconer, *Spillover in Heterogeneous Catalysis*, Chemical Reviews, vol. 95, **1995**, p. 759-788.

(28) P.A. Cox, J.B. Goodenough, P.J. Tavener, D. Telles, and R.G. Egdell, *The electronic structure of Bi2-xGdxRu2O7 and RuO_2: A study by electron spectroscopy*, Journal of Solid State Chemistry, vol. 62, **1986**, p. 360-370.

(29) D.E. Curtin, R.D. Lousenberg, T.J. Henry, P.C. Tangeman, and M.E. Tisack, *Advanced materials for improved PEMFC performance and life*, Journal of Power Sources, vol. 131, **2004**, p. 41-48.

(30) W. Dmowski, T. Egami, K. Swider-Lyons, C. Love, and D. Rolison, *Local Atomic Structure and Conduction Mechanism of Nanocrystalline Hydrous RuO_2 from X-ray Scattering*, Journal of Physical Chemistry B, vol. 106, **2002**, p. 12677-12683.

(31) C. Du, P.F. Shi, X.Q. Cheng, and G.P. Yin, *Effective protonic and electronic conductivity of the catalyst layers in proton exchange membrane fuel cells*, Electrochemistry Communications, vol. 6, Mai. **2004**, p. 435-440.

(32) S. Dutta, S. Shimpalee, and J. Van Zee, *Three-dimensional numerical simulation of straight channel PEM fuel cells*, Journal of Applied Electrochemistry, vol. 30, **2000**, p. 135-146.

(33) D. Eder and A. Windle, *Morphology control of CNT-TiO2 hybrid materials and rutile nanotubes*, Journal of Materials Chemistry, vol. 18, **2008**, p. 2036-2043.

(34) D. Eder and A. Windle, *Carbon-inorganic hybrid materials: The carbon-nanotube/TiO2 interface*, Advanced Materials, vol. 20, **2008**, p. 1787-+.

(35) H. Ekström, B. Wickman, M. Gustavsson, P. Hanarp, L. Eurenius, E. Olsson, and G. Lindbergh, *Nanometer-thick films of titanium oxide acting as electrolyte in the polymer electrolyte fuel cell*, Electrochimica Acta, vol. 52, **2007**, p. 4239-4245.

(36) S. Escribano, P. Aldebert, and M. Pineri, *Volumic electrodes of fuel cells with polymer electrolyte membranes: electrochemical performances and structural analysis by thermoporometry*, Electrochimica Acta, vol. 43, **1998**, p. 2195-2202.

(37) P.J. Ferreira, G.J. la O', Y. Shao-Horn, D. Morgan, R. Makharia, S. Kocha, and H.A. Gasteiger, *Instability of Pt/C electrocatalysts in proton exchange membrane fuel cells - A mechanistic investigation*, Journal of the Electrochemical Society, vol. 152, **2005**, p. A2256-A2271.

(38) A. Fischer, J. Jindra, and H. Wendt, *Porosity and catalyst utilization of thin layer cathodes in air operated PEM-fuel cells*, Journal of Applied Electrochemistry, vol. 28, **1998**, p. 277-282.

(39) P. Flynn and S. Wanke, *Limitation of Transmission Electron-Microscope for Characterization of Supported Metal-Catalysts*, Journal of Catalysis, vol. 33, **1974**, p. 233-248.

(40) T. Frey and M. Linardi, *Effects of membrane electrode assembly preparation on the polymer electrolyte membrane fuel cell performance*, Electrochimica Acta, vol. 50, **2004**, p. 99-105.

(41) H. Gasteiger, S. Kocha, B. Sompalli, and F. Wagner, *Activity benchmarks and requirements for Pt, Pt-alloy, and non-Pt oxygen reduction catalysts for PEMFCs*, Applied Catalysis B-Environmental, vol. 56, **2005**, p. 9-35.

(42) H. Gasteiger, N. Markovic, P. Ross, and E. Cairns, *Methanol Electrooxidation on Well-Characterized Pt-Ru Alloys*, Journal of Physical Chemistry, vol. 97, **1993**, p. 12020-12029.

(43) Digital Micrograph, Vers. 3.4, Pleasanton, CA: Gatan, Inc.

(44) T.D. Gierke, G.E. Munn, and F.C. Wilson, *The morphology in nafion perfluorinated membrane products, as determined by wide- and small-angle x-ray studies*, Journal of Polymer Science: Polymer Physics Edition, vol. 19, **1981**, p. 1687-1704.

(45) S. Kimball, P. Mattis, N. Archibald, L. Barrancos, H. Breuer, S. Budig, J.S.O. Bueno, L. Clausen, et al., *Gimp - GNU Image Manipulation Program*; www.gimp.org.

(46) J. Giner and C. Hunter, *The Mechanism of Operation of the Teflon-Bonded Gas Diffusion Electrode: A Mathematical Model*, Journal of the Electrochemical Society, vol. 116, **1969**, p. 1124-1130.

(47) N. Giordano, P. Antonucci, E. Passalacqua, L. Pino, A. Arico, and K. Kinoshita, *Relationship between Physicochemical Properties and Electrooxidation Behavior of Carbon Materials*, Electrochimica Acta, vol. 36, **1991**, p. 1931-1935.

(48) P. Gode, F. Jaouen, G. Lindbergh, A. Lundblad, and G. Sundholm, *Influence of the composition on the structure and electrochemical characteristics of the PEFC cathode*, Electrochimica Acta, vol. 48, **2003**, p. 4175-4187.

(49) R.C. Gonzalez, R.E. Woods, and S.L. Eddins, *Digital Image Processing Using Matlab*, Prentice Hall, **2004**.

(50) J.B. Goodenough, A. Hamnett, B.J. Kennedy, R. Manoharan, and S.A. Weeks, *Methanol oxidation on unsupported and carbon supported Pt + Ru anodes*, Journal of Electroanalytical Chemistry, vol. 240, **1988**, p. 133-145.

(51) Y. Gu and W. Wong, *Nanostructure PtRu/MWNTs as anode catalysts prepared in a vacuum for direct methanol oxidation*, Langmuir, vol. 22, **2006**, p. 11447-11452.

(52) E. Guilminot, A. Corcella, F. Charlot, F. Maillard, and M. Chatenet, *Detection of Ptz+ ions and Pt nanoparticles inside the membrane of a used PEMFC*, Journal of the Electrochemical Society, vol. 154, **2007**, p. B96-B105.

(53) P.L. Hagans, K.E. Swider, and D.R. Rolison, *The chemical state of Ru in Pt-Ru direct methanol fuel cell anode electrocatalysts*, in: Proceedings of the Electrochemical Society (Electrode Materials and Processes for Energy Conversion and Storage IV), Pennington, NJ: Electrochemical Society, **1997**, pp. 86-105.

(54) C.H. Hamann and W. Vielstich, *Elektrochemie*, Weinheim, Germany: Wiley-VCH Verlag GmbH, **1998**.

(55) C.H. Hamann and W. Vielstich, *Untersuchung der kathodischen Sauerstoffreduktion mit der rotierenden Scheibe-Ring-Elektrode*, in: Elektrochemie, Weinheim, Germany: Wiley-VCH Verlag GmbH, **1998**, p. 343-345.

(56) A. Hamnett, *Mechanism and electrocatalysis in the direct methanol fuel cell*, Catalysis Today, vol. 38, **1997**, p. 445-457.

(57) J. Harris and D. Scheffler, *Routine preparation of air-dried negatively stained and unstained specimens on holey carbon support films: a review of applications*, Micron, vol. 33, **2002**, p. 461-480.

(58) J. Harris, C. Roos, R. Djalali, O. Rheingans, M. Maskos, and M. Schmidt, *Application of the negative staining technique to both aqueous and organic solvent solutions of polymer particles*, Micron, vol. 30, **1999**, p. 289-298.

(59) C. Hartnig, I. Manke, N. Kardjilo, A. Hilger, M. Gruenerbel, J. Kaczerowski, J. Banhart, and W. Lehnert, *Combined neutron radiography and locally resolved current density measurements of operating PEM fuel cells*, Journal of Power Sources, vol. 176, **2008**, p. 452-459.

(60) H. Haubold, T. Vad, H. Jungbluth, and P. Hiller, *Nano structure of NAFION: a SAXS study*, Electrochimica Acta, vol. 46, **2001**, p. 1559-1563.

(61) D. He, L. Yang, S. Kuang, and Q. Cai, *Fabrication and catalytic properties of Pt and Ru decorated TiO2\CNTs catalyst for methanol electrooxidation*, Electrochemistry Communications, vol. 9, **2007**, p. 2467-2472.

(62) F. Hofer, P. Warbichler, and W. Grogger, *Imaging of nanometer-sized precipitates in solids by electron spectroscopic imaging*, Ultramicroscopy, vol. 59, **1995**, p. 15-31.

(63) W.Y. Hsu and T.D. Gierke, *Ion transport and clustering in nafion perfluorinated membranes*, Journal of Membrane Science, vol. 13, **1983**, p. 307-326.

(64) J. Hwang, C. Chen, R. Savinell, C. Liu, and J. Wainright, *A three-dimensional numerical simulation of the transport phenomena in the cathodic side of a PEMFC*, Journal of Applied Electrochemistry, vol. 34, **2004**, p. 217-224.

(65) M. Hyun, S. Kim, B. Lee, D. Peck, Y. Shul, and D. Jung, *Effect of NaBH4 concentration on the characteristics of PtRu/C catalyst for the anode of DMFC prepared by the impregnation method*, Catalysis Today, vol. 132, **2008**, p. 138-145.

(66) J. Ihonen, F. Jaouen, G. Lindbergh, A. Lundblad, and G. Sundholm, *Investigation of mass-transport limitations in the solid polymer fuel cell cathode - II. Experimental*, Journal of the Electrochemical Society, vol. 149, **2002**, p. A448-a454.

(67) Y. Ishikawa, M. Liao, and C. Cabrera, *Oxidation of methanol on platinum, ruthenium and mixed Pt-M metals (M = Ru, Sn): a theoretical study*, Surface Science, vol. 463, **2000**, p. 66-80.

(68) T. Iwasita, *Electrocatalysis of methanol oxidation*, Electrochimica Acta, vol. 47, **2002**, p. 3663-3674.

(69) S. Iyer, D. Nandan, and B. Venkataramani, *Alkaline earth metal ion-proton-exchange equilibria on Nafion-117 and Dowex 50W X8 in aqueous solutions at 298+/-1K*, Reactive & Functional Polymers, vol. 29, **1996**, p. 51-57.

(70) C. Jaffray and G. Hards, *Precious metal supply requirements*, Handbook of Fuel Cells - Fundamentals Technologie and Applications, Chichester, England: John Wiley & Sons Ltd., **2003**, vol. 3, chap. 41, p. 509-513.

(71) F. Jaouen, G. Lindbergh, and G. Sundholm, *Investigation of mass-transport limitations in the solid polymer fuel cell cathode - I. Mathematical model*, Journal of the Electrochemical Society, vol. 149, **2002**, p. A437-a447.

(72) K. Jeng, C. Chien, N. Hsu, S. Yen, S. Chiou, S. Lin, and W. Huang, *Performance of direct methanol fuel cell using carbon nanotube-supported Pt-Ru anode catalyst with controlled composition*, Journal of Power Sources, vol. 160, **2006**, p. 97-104.

(73) S. Jiang, K. Xia, and G. Xu, *Effect of additives on self-assembling behavior of Nafion in aqueous media, Macromolecules*, vol. 34, **2001**, p. 7783-7788.

(74) Z. Jiao, X. Zhang, J. Cheng, X. Tao, and D. He, *Preparation and characterization of carbon nanotubes/ZnS composite*, Journal of Inorganic Materials, vol. 23, **2008**, p. 491-495.

(75) L.R. Jordan, A.K. Shukla, T. Behrsing, N.R. Avery, B.C. Muddle, and M. Forsyth, *Effect of diffusion-layer morphology on the performance of polymer electrolyte fuel cells operating at atmospheric pressure*, Journal of Applied Electrochemistry, vol. 30, **2000**, p. 641-646.

(76) J. Kim, H.Y. Ha, I.H. Oh, S.A. Hong, H.I. Lee, *Influence of the solvent in anode catalyst ink on the performance of a direct methanol fuel cell*, Journal of Power Sources, vol. 135, **2004**, p. 29–35.

(77) K.S. Kim and N. Winograd, *X-Ray photoelectron spectroscopic studies of ruthenium-oxygen surfaces*, Journal of Catalysis, vol. 35, **1974**, p. 66-72.

(78) H. Kim, I. de Moraes, G. Tremiliosi, R. Haasch, and A. Wieckowski, *Chemical state of ruthenium submonolayers on a Pt(111) electrode*, Surface Science, vol. 474, **2001**, p. L203-L212.

(79) I. Kim, J. Kim, Y. Lee, and K. Kim, *Synthesis and characterization of electrochemically prepared ruthenium oxide on carbon nanotube film substrate for supercapacitor applications*, Journal of the Electrochemical Society, vol. 152, **2005**, p. A2170-a2178.

(80) S. Kim, M. Khandelwal, C. Chacko, and M.M. Mench, *Investigation of the Impact of Interfacial Delamination on Polymer Electrolyte Fuel Cell Performance*, Journal of The Electrochemical Society, vol. 156, **2009**, p. B99-B108.

(81) S. Knights, K. Colbow, J. St-Pierre, and D. Wilkinson, *Aging mechanisms and lifetime of PEFC and DMFC*, Journal of Power Sources, vol. 127, **2004**, p. 127-134.

(82) C. Kong, D. Kim, H. Lee, Y. Shul, and T. Lee, *Influence of pore-size distribution of diffusion layer on mass-transport problems of proton exchange membrane fuel cells*, Journal of Power Sources, vol. 108, **2002**, p. 185-191.

(83) K. Kreuer, S. Paddison, E. Spohr, and M. Schuster, *Transport in proton conductors for fuel-cell applications: Simulations, elementary reactions, and phenomenology*, Chemical Reviews, vol. 104, **2004**, p. 4637-4678.

(84) S. Kumar and W.W. Adams, *Electron beam damage in high temperature polymers*, Polymer, vol. 31, **1990**, p. 15-19.

(85) J. Larminie and A. Dicks, *Fuel Cell Systems Explained*, Chichester, England: John Wiley & Sons, Ltd, **1999**.

(86) K. Lasch, G. Hayn, L. Jorissen, J. Garche, and O. Besenhardt, *Mixed conducting catalyst support materials for the direct methanol fuel cell*, Journal of Power Sources, vol. 105, **2002**, p. 305-310.

(87) K. Lasch, L. Jorissen, K. Friedrich, and J. Garche, *The function of ruthenium oxides in Pt-Ru catalysts for methanol electro-oxidation at low temperatures*, Journal of Solid State Electrochemistry, vol. 7, **2003**, p. 619-625.

(88) W. Lee, C. Ho, J.W. Van Zee, and M. Murthy, *The effects of compression and gas diffusion layers on the performance of a PEM fuel cell*, Journal of Power Sources, vol. 84, **1999**, p. 45-51.

(89) H. Lee, J. Park, D. Kim, and T. Lee, *A study on the characteristics of the diffusion layer thickness and porosity of the PEMFC*, Journal of Power Sources, vol. 131, **2004**, p. 200-206.

(90) A. Lehmani, S. Durand-Vidal, and P. Turq, *Surface morphology of Nafion 117 membrane by tapping mode atomic force microscope*, Journal of Applied Polymer Science, vol. 68, **1998**, S. 503-508.

(91) E. Leiva, C. Sanchez, W. Vielstich, A. Lamm, and H.A. Gasteiger, *Theoretical Aspects of some Prototypical Fuel Cell Reactions*, Handbook of Fuel Cells - Fundamentals Technologie and Applications, Chichester, England: John Wiley & Sons Ltd., **2003**, p. 93-131.

(92) W. Li, C. Liang, W. Zhou, J. Qiu, Z. Zhou, G. Sun, and Q. Xin, *Preparation and characterization of multiwalled carbon nanotube-supported platinum for cathode catalysts of direct methanol fuel cells*, Journal of Physical Chemistry B, vol. 107, **2003**, p. 6292-6299.

(93) H. Liu, C. Song, L. Zhang, J. Zhang, H. Wang, and D. Wilkinson, *A review of anode catalysis in the direct methanol fuel cell*, Journal of Power Sources, vol. 155, **2006**, p. 95-110.

(94) J. Liu, Z. Zhou, X. Zhao, Q. Xin, G. Sun, and B. Yi, *Studies on performance degradation of a direct methanol fuel cell (DMFC) in life test*, Physical Chemistry Chemical Physics, vol. 6, **2004**, p. 134-137.

(95) W. Liu, K. Ruth, and G. Rusch, *Membrane durability in PEM fuel cells*, Journal of new Materials for Elelctrochemical Systems, vol. 4, **2001**, p. 227-232.

(96) W. Liu, B. Wu, and C. Cha, *Surface diffusion and the spillover of H-adatoms and oxygen-containing surface species on the surface of carbon black and Pt/C porous electrodes*, Journal of Electroanalytical Chemistry, vol. 476, **1999**, p. 101-108.

(97) Y. Liu, X. Qiu, Y. Huang, W. Zhu, and G. Wu, *Influence of preparation process of MEA with meso-carbon microbeads supported Pt-Ru catalysts on methanol electrooxidation*, Journal of Applied Electrochemistry, vol. 32, **2002**, p. 1279-1285.

(98) M. Lo, I. Liao, and C. Huang, *Key issues in the preparation of DMFC electrocatalysts*, International Journal of Hydrogen Energy, vol. 32, **2007**, p. 731-735.

(99) J. Lobato, M. Rodrigo, J. Linares, and K. Scott, *Effect of the catalytic ink preparation method on the performance of high temperature polymer electrolyte membrane fuel cells*, Journal of Power Sources, vol. 157, **2006**, p. 284-292.

(100) J. Long, R. Stroud, K. Swider-Lyons, and D. Rolison, *How to make electrocatalysts more active for direct methanol oxidation - Avoid PtRu bimetallic alloys!*, Journal of Physical Chemistry B, vol. 104, **2000**, p. 9772-9776.

(101) B. Loppinet, G. Gebel, and C. Williams, *Small-angle scattering study of perfluorosulfonated ionomer solutions*, Journal of Physical Chemistry B, vol. 101, **1997**, p. 1884-1892.

(102) T. Maiyalagan, *Synthesis and electro-catalytic activity of methanol oxidation on nitrogen containing carbon nanotubes supported Pt electrodes*, Applied Catalysis B-Environmental, vol. 80, **2008**, p. 286-295.

(103) K. Malek, M. Eikerling, Q. Wang, T. Navessin, and Z. Liu, *Self-Organization in Catalyst Layers of Polymer Electrolyte Fuel Cells*, Journal of Physical Chemistry C, vol. 111, **2007**, p. 13627-13634.

(104) M. Mathias, J. Roth, J. Fleming, and W. Lehnert, *Diffuision media materials and characterisation*, Handbook of Fuel Cells - Fundamentals Technologie and Applications, Chichester, England: John Wiley & Sons Ltd., **2003**, vol.3, chap. 42, p. 517-537.

(105) K. Mauritz and R. Moore, *State of understanding of Nafion*, Chemical Reviews, vol. 104, **2004**, p. 4535-4585.

(106) J. McBreen, *Voltametric studies of electrodes in contact with ionomeric membranes*, Journal of the Electrochemical Society, vol. 132, **1985**, p. 1112-1116.

(107) D. McKeown, P. Hagans, L. Carette, A. Russell, K. Swider, and D. Rolison, *Structure of hydrous ruthenium oxides: Implications for charge storage*, Journal of Physical Chemistry B, vol. 103, **1999**, p. 4825-4832.

(108) P. Midgley and M. Weyland, *3D electron microscopy in the physical sciences: the development of Z-contrast and EFTEM tomography*, Ultramicroscopy, vol. 96, **2003**, p. 413-431.

(109) V. Mittal, H. Kunz, and J. Fenton, *Membrane degradation mechanisms in PEMFCs,* Journal of the Electrochemical Society, vol. 154, **2007**, p. B652-B656.

(110) R.B. Moore and C.R. Martin, *Procedure for preparing solution-cast perfluorosulfonate ionomer films and membranes*, Analytical Chemistry, vol. 58, **1986**, p. 2569-2570.

(111) C.F. Mora, A.K.H. Kwan, and H.C. Chan, *Particle size distribution analysis of coarse aggregate using digital image processing*, Cement and Concrete Research, vol. 28, **1998**, p. 921-932.

(112) S. Muerza, H. Berthiaux, S. Massol-Chaudeur, and G. Thomas, *A dynamic study of static mixing using on-line image analysis*, Powder Technology, vol. 128, **2002**, p. 195-204.

(113) P. Mukherjee and C. Wang, *Stochastic microstructure reconstruction and direct numerical simulation of the PEFC catalyst layer*, Journal of the Electrochemical Society, vol. 153, **2006**, p. A840-a849.

(114) J. Nordlund, A. Roessler, and G. Lindbergh, *The influence of electrode morphology on the performance of a DMFC anode,* Journal of Applied Electrochemistry, vol. 32, **2002**, p. 259-265.

(115) W. O'Grady, P. Hagans, K. Pandya, and D. Maricle, *Structure of Pt/Ru catalysts using X-ray absorption near edge structure studies*, Langmuir, vol. 17, **2001**, p. 3047-3050.

(116) H. Oh, J. Oh, Y. Hong, and H. Kim, *Investigation of carbon-supported Pt nanocatalyst preparation by the polyol process for fuel cell applications*, Electrochimica Acta, vol. 52, **2007**, p. 7278-7285.

(117) A. O'Mullane, S. Dale, T. Day, N. Wilson, J. Macpherson, and P. Unwin, *Formation of polyaniline/Pt nanoparticle composite films and their electrocatalytic properties*, Journal of Solid State Electrochemistry, vol. 10, **2006**, p. 792-807.

(118) M.T. Pareschi, M. Pompilio, and F. Innocenti, *Automated evaluation of volumetric grain-size distribution from thin-section images*, Computers & Geosciences, vol. 16, **1990**, p. 1067-1084.

(119) H. Park, Y. Cho, Y. Cho, I. Park, N. Jung, M. Ahn, and Y. Sung, *Modified Decal Method and Its Related Study of Microporous Layer in PEM Fuel Cells*, Journal of The Electrochemical Society, vol. 155, **2008**, p. B455-B460.

(120) K. Park and K. Seol, *Nb-TiO2 supported Pt cathode catalyst for polymer electrolyte membrane fuel cells*, Electrochemistry Communications, vol. 9, **2007**, p. 2256-2260.

(121) E. Passalacqua, F. Lufrano, G. Squadrito, A. Patti, and L. Giorgi, *Nafion content in the catalyst layer of polymer electrolyte fuel cells: effects on structure and performance*, Electrochimica Acta, vol. 46, **2001**, p. 799-805.

(122) J.W. Patrick, *Porosity in Carbons: Characterization and Applications*, New York: John Wiley & Sons Inc, chap. 10.2, **1995**, p. 260.

(123) U. Paulus, Z. Veziridis, B. Schnyder, M. Kuhnke, G. Scherer, and A. Wokaun, *Fundamental investigation of catalyst utilization at the electrode/solid polymer electrolyte interface - Part I. Development of a model system*, Journal of Electroanalytical Chemistry, vol. 541, **2003**, p. 77-91.

(124) M. Perry, J. Newman, and E. Cairns, *Mass transport in gas-diffusion electrodes: A diagnostic tool for fuel-cell cathodes*, Journal of the Electrochemical Society, vol. 145, **1998**, p. 5-15.

(125) Z. Porat u. a., *Electron-Microscopy Investigation of the Microstructure of Nafion Films*, Journal of Physical Chemistry, vol. 99, **1995**, p. 4667-4671.

(126) J. Prabhuram, T. Zhao, Z. Tang, R. Chen, and Z. Liang, *Multiwalled carbon nanotube supported PtRu for the anode of direct methanol fuel cells*, Journal of Physical Chemistry B, vol. 110, **2006**, p. 5245-5252.

(127) W.D. Pyrz and D.J. Buttrey, *Particle Size Determination Using TEM: A Discussion of Image Acquisition and Analysis for the Novice Microscopist.*, Langmuir, **2008**; doi:10.1021/la801367j.

(128) Z. Qi, M. Lefebvre, and P. Pickup, *Electron and proton transport in gas diffusion electrodes containing electronically conductive proton-exchange polymers*, Journal of Electroanalytical Chemistry, vol. 459, **1998**, p. 9-14.

(129) A. Rack, S. Zabler, B. Mueller, H. Riesemeier, G. Weldemann, A. Lange, J. Goebbels, M. Hentschel, and W. Goerner, *High resolution synchrotron-based radiography and tomography using hard X-rays at the BAMline (BESSY II)*, Nuclear Instruments & Methods in Physics Research Section, vol. 586, **2008**, p. 327-344.

(130) L. Reimer, *Scanning Electron Microscopy: Physics of Image Formation and Microanalysis*, Springer, **1998**, p. 87-90.

(131) C. Reiser, L. Bregoli, T. Patterson, J. Yi, J. Yang, M. Perry, and T. Jarvi, *A reverse-current decay mechanism for fuel cells*, Electrochemical and Solid State Letters, vol. 8, **2005**, p. A273-A276.

(132) K. Reuter and M. Scheffler, *Surface core-level shifts at an oxygen-rich Ru surface: O/Ru(0001) vs. RuO_2(110)*, Surface Science, vol. 490, **2001**, p. 20-28.

(133) S. Rieberer and K. Norian, *Analytical Electron-Microscopy of Nafion Ion-Exchange Membranes*, Ultramicroscopy, vol. 41, **1992**, p. 225-233.

(134) S.P. Rigby and K.J. Edler, *The Influence of Mercury Contact Angle, Surface Tension, and Retraction Mechanism on the Interpretation of Mercury Porosimetry Data*, Journal of Colloid and Interface Science, vol. 250, **2002**, p. 175-190.

(135) D. Rochefort, P. Dabo, D. Guay, and P. Sherwood, *XPS investigations of thermally prepared RuO_2 electrodes in reductive conditions*, Electrochimica Acta, vol. 48, **2003**, p. 4245-4252.

(136) J. Rodríguez-Carvajal, *Recent developments of the program FULLPROF*, Newsletter of the Commission on Powder Diffraction, vol. 26, **2001**, p. 12-19.

(137) D. Rolison, P. Hagans, K. Swider, and J. Long, *Role of hydrous ruthenium oxide in Pt-Ru direct methanol fuel cell anode electrocatalysts: The importance of mixed electron/proton conductivity*, Langmuir, vol. 15, **1999**, p. 774-779.

(138) L. Rubatat, G. Gebel, and O. Diat, *Fibrillar structure of Nafion: Matching Fourier and real space studies of corresponding films and solutions*, Macromolecules, vol. 37, **2004**, p. 7772-7783.

(139) A. Saab, F. Garzon, and T. Zawodzinski, *Determination of ionic and electronic resistivities in carbon/polyelectrolyte fuel-cell composite electrodes*, Journal of the Electrochemical Society, vol. 149, **2002**, p. A1541-a1546.

(140) C. Sánchez, E. Leiva, W. Vielstich, A. Lamm, and H.A. Gasteiger, *Catalysis by UPD metals,* in: Handbook of Fuel Cells - Fundamentals Technologie and Applications, Chichester, England: John Wiley & Sons Ltd., **2003**, p. 47-61.

(141) R. Satija, D. Jacobson, M. Arif, and S. Werner, *In situ neutron imaging technique for evaluation of water management systems in operating PEM fuel cells*, Journal of Power Sources, vol. 129, **2004**, p. 238-245.

(142) Linda C. Sawyer and David T. Grubb, in: *Polymer Microscopy*, London, England: Chapman and Hall, **1987**, Chap. 5, 30.

(143) A. Schmid, *Die Diffusionsgaselektrode*, Helvetica Chimica Acta, vol. 7, **1924**, p. 370-373.

(144) M. Schulze, M. Lorenz, N. Wagner, and E. Gulzow, *XPS analysis of the degradation of Nafion*, Fresenius Journal of Analytical Chemistry, vol. 365, Okt. **1999**, p. 106-113.

(145) M. Schulze, M. von Bradke, R. Reissner, M. Lorenz, and E. Gulzow, *Characterization of polymers in PEFC-electrodes with EDX and XPS*, Fresenius Journal of Analytical Chemistry, vol. 365, Okt. **1999**, p. 123-132.

(146) H. Yu, J. Schumacher, M. Zobel, and C. Hebling, *Analysis of membrane electrode assembly (MEA) by environmental scanning electron microscope (ESEM)*, Journal of Power Sources, vol. 145, **2005**, p. 216-222.

(147) E. Seddon and K. Seddon, *The Chemistry of Ruthenium*, Amsterdam: Elsevier, **1984**, p. 71.

(148) Y. Shao, G. Yin, Y. Gao, and P. Shi, *Durability study of Pt/C and Pt/CNTs catalysts under simulated PEM fuel cell conditions*, Journal of the Electrochemical Society, vol. 153, **2006**, p. A1093-a1097.

(149) J. Shim and J. Lee, *Development of electrode structure and analysis of electrode pore distributions in phosphoric acid fuel cells*, Materials Chemistry and Physics, vol. 63, **2000**, p. 133-138.

(150) S.J. Shin, J.K. Lee, H.Y. Ha, S.A. Hong, H.S. Chun and I.H. Oh, *Effect of the catalytic ink preparation method on the performance of polymer electrolyte membrane fuel cells*, Journal of Power Sources, vol. 106, **2002**, p. 146-152.

(151) S. Shimpalee, U. Beuscher, and J. Van Zee, *Analysis of GDL flooding effects on PEMFC performance*, Electrochimica Acta , vol. 52, **2007**, p. 6748-6754.

(152) A. Sirk, J. Hill, S. Kung, and V. Birss, *Effect of redox state of PtRu electrocatalysts on methanol oxidation activity*, Journal of Physical Chemistry B, vol. 108, **2004**, p. 689-695.

(153) Z. Siroma, N. Fujiwara, T. Ioroi, S. Yamazaki, K. Yasuda, and Y. Miyazaki, *Dissolution of Nafion (R) membrane and recast Nafion (R) film in mixtures of methanol and water*, Journal of Power Sources, vol. 126, **2004**, p. 41-45.

(154) J. Song, S. Suzuki, H. Uchida, and M. Watanabe, *Preparation of High Catalyst Utilization Electrodes for Polymer Electrolyte Fuel Cells*, Langmuir, vol. 22, **2006**, p. 6422-6428.

(155) T.E. Springer, T.A. Zawodzinski, M.S. Wilson, and S. Gottesfeld, *Characterization of Polymer Electrolyte Fuel Cells Using AC Impedance Spectroscopy*, Journal of The Electrochemical Society, vol. 143, **1996**, p. 587-599.

(156) R. Stroud, J. Long, K. Swider-Lyons, and D. Rolison, *Transmission electron microscopy studies of the nanoscale structure and chemistry of Pt50Ru50 electrocatalysts*, Microscopy and Microanalysis, vol. 8, **2002**, p. 50-57.

(157) W. Sugimoto, H. Iwata, K. Yokoshima, Y. Murakami, and Y. Takasu, *Proton and electron conductivity in hydrous ruthenium oxides evaluated by electrochemical impedance spectroscopy: The origin of large capacitance*, Journal of Physical Chemistry B, vol. 109, **2005**, p. 7330-7338.

(158) E. Szajdzinska-Pietek, S. Schlick, and A. Plonka, *Self-Assembling of Perfluorinated Polymeric Surfactants in Nonaqueous Solvents - Electron-Spin-Resonance Spectra of Nitroxide Spin Probes in Nafion Solutions and Swollen Membranes*, Langmuir, vol. 10, **1994**, p. 2188-2196.

(159) J. Tang, K. Jensen, M. Waje, W. Li, P. Larsen, K. Pauley, u. a., *High performance hydrogen fuel cells with ultralow Pt loading carbon nanotube thin film catalysts*, Journal of Physical Chemistry C, vol. 111, **2007**, p. 17901-17904.

(160) H. Tang, S. Wang, M. Pan, and R. Yuan, *Porosity-graded micro-porous layers for polymer electrolyte membrane fuel cells*, Journal of Power Sources, vol. 166, **2007**, p. 41-46.

(161) S. Thomas, X. Ren, and S. Gottesfeld, *Influence of ionomer content in catalyst layers on direct methanol fuel cell performance*, Journal of The Electrochemical Society, vol. 146, **1999**, p. 4354-4359.

(162) E.A. Ticianelli, *A Modeling Approach to the Characterization of the Limiting Polarization Behavior of Gas-Diffusion Electrodes*, Journal of Electroanalytical Chemistry, vol. 387, **1995**, p. 1-10.

(163) S. Trasatti, *Physical Electrochemistry of Ceramic Oxides*, Electrochimica Acta, vol. 36, **1991**, p. 225-241.

(164) W. Tu, W. Liu, C. Cha, and B. Wu, *Study of the powder/membrane interface by using the powder microelectrode technique I. The Pt-black/Nafion (R) interfaces*, Electrochimica Acta, vol. 43, **1998**, p. 3731-3739.

(165) M. Tucker, M. Odgaard, P. Lund, S. Yde-Andersen, and J.O. Thomas, *The pore structure of direct methanol fuel cell electrodes*, Journal of the Electrochemical Society, vol. 152, **2005**, p. A1844-A1850.

(166) M. Uchida, Y. Aoyama, N. Eda, and A. Ohta, *New Preparation Method for Polymer-Electrolyte Fuel-Cells*, Journal of the Electrochemical Society, vol. 142, **1995**, p. 463-468.

(167) M. Uchida, Y. Fukuoka, Y. Sugawara, N. Eda, and A. Ohta, *Effects of microstructure of carbon support in the catalyst layer on the performance of polymer-electrolyte fuel cells*, Journal of the Electrochemical Society, vol. 143, **1996**, p. 2245-2252.

(168) M. Uchida, Y. Aoyama, N. Eda, and A. Ohta, *Investigation of the microstructure in the catalyst layer and effects of both perfluorosulfonate ionomer and PTFE-Loaded carbon on the catalyst layer of polymer electrolyte fuel cells*, Journal of the Electrochemical Society, vol. 142, **1995**, p. 4143-4149.

(169) M. Uchida, Y. Fukuoka, Y. Sugawara, H. Ohara, and A. Ohta, *Improved preparation process of very-low-platinum-loading electrodes for polymer electrolyte fuel cells*, Journal of the Electrochemical Society, vol. 145, **1998**, p. 3708-3713.

(170) H. Villullas, F. Mattos-Costa, and L. Bulhoes, *Electrochemical oxidation of methanol on Pt nanoparticles dispersed on RuO_2*, Journal of Physical Chemistry B, vol. 108, **2004**, p. 12898-12903.

(171) R. Viswanathan, G. Hou, R. Liu, S. Bare, F. Modica, G. Mickelson, C. Segre, N. Leyarovska, and E. Smotkin, *In-situ XANES of carbon-supported Pt-Ru anode electrocatalyst for reformate-air polymer electrolyte fuel cells*, Journal of Physical Chemistry B, vol. 106, **2002**, p. 3458-3465.

(172) C. Wagner, A. Naumkin, A. Kraut-Vass, J. Allison, C. Powell, and J. Rumble Jr, *NIST X-ray Photoelectron Spectroscopy Database, Version 3.5*; National Institute of Standards and Technology, Gaithersburg, **2003**, http://srdata.nist.gov/xps/.

(173) M. Waje, X. Wang, W. Li, and Y. Yan, *Deposition of platinum nanoparticles on organic functionalized carbon nanotubes grown in situ on carbon paper for fuel cells*, Nanotechnology, vol. 16, **2005**, p. S395-S400.

(174) S. Wang, G. Sun, Z. Wu, and Q. Xin, *Effect of Nation (R) ionomer aggregation on the structure of the cathode catalyst layer of a DMFC*, Journal of Power Sources, vol. 165, **2007**, p. 128-133.

(175) C. Wang, M. Waje, X. Wang, J. Tang, R. Haddon, and Y. Yan, *Proton exchange membrane fuel cells with carbon nanotube based electrodes*, Nano Letters, vol. 4, **2004**, p. 345-348.

(176) X. Wang, M. Waje, and Y. Yan, *CNT-based electrodes with high efficiency for PEMFCs*, Electrochemical and Solid State Letters, vol. 8, **2005**, p. A42-a44.

(177) X. Wang, W. Li, Z. Chen, M. Waje, and Y. Yan, *Durability investigation of carbon nanotube as catalyst support for proton exchange membrane fuel cell*, Journal of Power Sources, vol. 158, **2006**, p. 154-159.

(178) X. Wang, H. Zhang, J. Zhang, H. Xu, Z. Tian, J. Chen, H. Zhong, Y. Liang, and B. Yi, *Microporous layer with composite carbon black for PEM fuel cells*, Electrochimica Acta, vol. 51, **2006**, p. 4909-4915.

(179) G. Wang, P. Mukherjee, and C. Wang, *Direct numerical simulation (DNS) modeling of PEFC electrodes - Part I. Regular microstructure*, Electrochimica Acta, vol. 51, **2006**, p. 3139-3150.

(180) G. Wang, P. Mukherjee, and C. Wang, *Direct numerical simulation (DNS) modeling of PEFC electrodes - Part II. Random microstructure*, Electrochimica Acta, vol. 51, **2006**, p. 3151-3160.

(181) C. Wang, *Fundamental models for fuel cell engineering*, Chemical Reviews, vol. 104, **2004**, p. 4727-4765.

(182) E.W. Washburn, *The Dynamics of Capillary Flow*, Physical Review, vol. 17, **1921**, p. 273.

(183) M. Watanabe, M. Tomikawa, and S. Motoo, *Experimental-Analysis of the Reaction Layer Structure in a Gas-Diffusion Electrode*, Journal of Electroanalytical Chemistry, vol. 195, **1985**, p. 81-93.

(184) A. Weber and J. Newman, *Modeling transport in polymer-electrolyte fuel cells*, Chemical Reviews, vol. 104, **2004**, p. 4679-4726.

(185) J. Wee, K. Lee, and S. Kim, *Fabrication methods for low-Pt-loading electrocatalysts in proton exchange membrane fuel cell systems*, Journal of Power Sources, vol. 165, **2007**, p. 667-677.

(186) Z. Wei, S. Wang, B. Yi, J. Liu, L. Chen, W. Zhou, W. Li, and Q. Xin, *Influence of electrode structure on the performance of a direct methanol fuel cell*, Journal of Power Sources, vol. 106, **2002**, p. 364-369.

(187) F. Will, *Electrochemical Oxidation of Hydrogen on Partially Immersed Platinum Electrodes .1. Experiments and Interpretation.*, Journal of The Electrochemical Society, vol. 110, **1963**, p. 145-151.

(188) Williams D.B.; Carter, C..B. in: *Transmission Electron Microscopy*, New York: Springer Science+Business Media, **1996,** vol. 1, Chap. 4, p. 61-63.

(189) M. Wilson and S. Gottesfeld, *Thin-Film Catalyst Layers for Polymer Electrolyte Fuel-Cell Electrodes*, Journal of Applied Electrochemistry, vol. 22, **1992**, p. 1-7.

(190) P. Wiseman, F. Capani, J. Squier, and M. Martone, *Counting dendritic spines in brain tissue slices by image correlation spectroscopy analysis*, Journal of Microscopy-Oxford, vol. 205, **2002**, p. 177-186.

(191) G. Wu and B. Xu, *Carbon nanotube supported Pt electrodes for methanol oxidation: A comparison between multi- and single-walled carbon nanotubes*, Journal of Power Sources, vol. 174, **2007**, p. 148-158.

(192) G. Wu, Y. Chen, and B. Xu, *Remarkable support effect of SWNTs in Pt catalyst for methanol electro oxidation.*, Electrochemistry Communications, vol. 7, **2005**, p. 1237-1243.

(193) J. Xie, F. Garzon, T. Zawodzinski, and W. Smith, *Ionomer segregation in composite MEAs and its effect on polymer electrolyte fuel cell performance*, Journal of the Electrochemical Society, vol. 151, **2004**, p. A1084-A1093.

(194) J. Xie, K. More, T. Zawodzinski, and W. Smith, *Porosimetry of MEAs made by "Thin film decal" method and its effect on performance of PEFCs*, Journal of the Electrochemical Society, vol. 151, **2004**, p. A1841-a1846.

(195) J. Xie, D. Wood, D. Wayne, T. Zawodzinski, P. Atanassov, and R. Borup, *Durability of PEFCs at high humidity conditions*, Journal of the Electrochemical Society, vol. 152, **2005**, p. A104-a113.

(196) J. Xie, D. Wood, K. More, P. Atanassov, and R. Borup, *Microstructural changes of membrane electrode assemblies during PEFC durability testing at high humidity conditions*, Journal of the Electrochemical Society, vol. 152, **2005**, p. A1011-a1020.

(197) R. Xu, C. Wu, and H. Xu, *Particle size and zeta potential of carbon black in liquid media*, Carbon, vol. 45, **2007**, p. 2806-2809.

(198) W. Yan, C. Soong, F. Chen, and H. Chu, *Effects of flow distributor geometry and diffusion layer porosity on reactant gas transport and performance of proton exchange membrane fuel cells*, Journal of Power Sources, vol. 125, **2004**, p. 27-39.

(199) L. Yang, C. Bock, B. MacDougall, and J. Park, *The role of the WOx ad-component to Pt and PtRu catalysts in the electrochemical CH_3OH oxidation reaction*, Journal of Applied Electrochemistry, vol. 34, **2004**, p. 427-438.

(200) E. Yoo, T. Okada, T. Kizuka, and J. Nakamura, *Effect of carbon substrate materials as a Pt-Ru catalyst support on the performance of direct methanol fuel cells*, Journal of Power Sources, vol. 180, **2008**, p. 221-226.

(201) K. Yoshizawa, K. Ikezoe, Y. Thsaki, D. Kramer, E. Lehmann, and G. Scherer, *Analysis of gas diffusion layer and flow-field design in a PEMFC using neutron radiography*, Journal of the Electrochemical Society, vol. 155, **2008**, p. B223-B227.

(203) Z. Zhan, J. Xiao, D. Li, M. Pan, and R. Yuan, *Effects of porosity distribution variation on the liquid -water flux through gas diffusion layers of PEM fuel cells*, Journal of Power Sources, vol. 160, **2006**, p. 1041-1048.

(204) L. Zhao and L. Gao, *Coating multi-walled carbon nanotubes with zinc sulfide*, Journal of Materials Chemistry, vol. 14, **2004**, p. 1001-1004.

LIST OF ABBREVIATIONS AND SYMBOLS

AFC	Alkaline Fuel Cell
AFM	Atomic Force Microscopy
BE	Binding Energy
BET	Brunauer-Emmer-Teller
BSE	Backscattered Electron
CNT	Carbon Nanotube
CV	Cyclic Voltammetry
DMFC	Direct Methanol Fuel Cell
EDX	Energy Dispersive X-ray spectroscopy
EELS	Electron Energy Loss Spectroscopy
EF-TEM	Energy Filtered Transmission Electron Microscopy
EFI	Energy Filtered Imaging
EW	Equivalent Weight
FFT	Fast Fourier Transform
GDL	Gas Diffusion Layer
HOR	Hydrogen Oxidation Reaction
MEA	Membrane Electrode Assembly
MPL	Microporous Layer

MWNT	Multi Walled Carbon Nanotube
NHE	Normal Hydrogen Electrode
ORR	Oxygen Reduction Reaction
PAFC	Phosphoric Acid Fuel Cell
PEFC	Polymer Electrolyte Fuel Cell
PFSI	Perfluorosulfonated ionomer
PTA	Phospho-Tungstic-Acid
PTFE	Polytetrafluoroethylene
SDS	Sodium Dodecyl Sulfate
SE	Secondary Electron
SEM	Scanning Electron Microscopy
STP	Standard Temperature and Pressure
SWNT	Single Walled Carbon Nanotube
TEM	Transmission Electron Microscopy
TFE	Tetrafluoroethylene
XPS	X-ray Photoelectron Spectroscopy
XRD	X-ray Diffraction

A	Power law coefficient
	Hamaker constant
c	Concentration of a species

D	Diffusion coefficient
d	Particle diameter
E	Electron Energy Loss Energy
ΔE^{0}_{rev}	Reversible cell potential at standard conditions
F	Faraday constant
I_{post}	Post-edge image intensity
I_{pre1}	First pre-edge image intensity
I_{pre2}	Second pre-edge image intensity
j	Current density
j_0	Exchange current density
n	Number of charge carriers
Q	Chemical reaction quotient
r	Power law decay factor
R	Ideal gas constant
T	Temperature in Kelvin
Y	Fitting parameter for XRD particle size determination
ΔG_a	Activation energy for anodic charge transfer process
ΔG_c	Activation energy for cathodic charge transfer process
$\Delta\varphi$	Change of electrode potential
α	Charge transfer coefficient

ε	Porosity
	Volume fraction
ζ	Tortuosity coefficient
η	Electrode overpotential
θ	Bragg diffraction angle
λ	Wavelength
σ	Conductivity
σ_0	Specific conductivity

LIST OF FIGURES & TABLES

Figure 6.4. *TEM micrograph of an ultra-thin section through a fuel cell electrode. Neither pores nor polymer electrolyte can be distinguished due to infiltration of the electrode by the embedding resin.*

Figure 6.5. *SE (left) and BSE (right) image of a thin-section through a MEA. In the SE image the darker outer parts of the upper electrode indicate regions where the embedding resin has penetrated into the electrode. (The bright hexagonal structure is due to the supporting copper grid.)*

Figure 6.6. *SEM images of an MEA showing inhomogeneous distribution of secondary pores and platinum agglomeration near the interface. Low magnification SE image of the complete MEA section (left). Upper electrode: platinum on carbon black, 40 vol. % Nafion. Lower electrode: PtRu black. Magnified part of the upper electrode layer (right).*

Figure 6.7. *SEM image of an electrode made of a Pt/C catalyst and 40 vol. % Nafion (left). Thresholded version of the image highlighting the pores in the structure (right).*

Figure 6.8. *Pore size distribution obtained by image analysis of Figure 6.7.*

Figure 6.9. *TEM micrograph of an ultra-thin section through a fuel cell electrode containing 40 vol. % Nafion.*

Figure 6.10. *Original grey-level TEM image of a part of the electrode shown in Figure 6.9.*

Figure 6.11. *Same image as in Fig. 6.10 but with the grey-level information remapped to a color palette to improve the visibility of faint contrast changes.*

Figure 6.12. *Auto-correlation image of the electrode image displayed in Fig. 6.9. The auto-correlation reveals to preferential directions almost perpendicular to each other.*

Figure 6.13. *Radial correlation functions obtained by integration of the auto-correlation image shown in Figure 6.12.*

Figure 6.14. *Pore size distribution curve expressed in terms of the fractional pore area determined by analysis of SEM images.*

Figure 6.15. *Photomontage of several TEM images. Polymer electrolyte colored in blue. MEA 40 vol. % Nafion.*

Figure 6.16. *Photomontage of several TEM images. Polymer electrolyte colored in blue. MEA 50 vol. % Nafion.*

Figure 6.17. *Photomontage of several TEM images. Polymer electrolyte colored in blue. MEA 60 vol. % Nafion.*

Figure 9.6. *Left graph: Cyclic voltammograms of the catalyst in 1 M $HClO_4$, before (solid line ——) and after (dashed line - - -) exposure to 1 M methanol solution for 1 hour.*
Right graph: Cyclic voltammograms of pure hydrous RuO_2 in 1 M $HClO_4$, as prepared (solid line ——), after exposure to 2 M methanol solution (dashed line - - -), and sample annealed at 70 °C (dotted line ····).
All cyclic voltammograms were recorded at a scan rate of 50 mV s^{-1}.

Figure 9.7. *CO stripping voltammograms of gas diffusion electrodes. Pt/$RuO_2 \cdot xH_2O$ catalyst (——solid line) and a commercial PtRu/C (20 wt. % on Vulcan XC-72R) catalyst (--- dashed line) for comparison.*

Figure 9.8. *DMFC half-cell measurement for methanol oxidation. Pt/RuO_2 xH_2O electrode (—— solid line),*
PtRu/C (20 wt. % on Vulcan XC-72R) catalyst (--- dashed line). Measurements were carried out at 50 °C with the cathode used as dynamic hydrogen electrode.

Figure 9.9. *Current-voltage curves for methanol oxidation in a DMFC full-cell arrangement. The curve of the hydrous Pt/RuO_2 catalyst is shown in comparison to an MEA prepared with a standard PtRu black catalyst (Johnson Matthey). Both measurements were carried out at 50 °C with 1 M methanol fed at 6 ml min^{-1} and an air flow of 500 ml min^{-1} (STP).*

Figure 10.1. *TEM image of a Pt/RuO_2/CNT catalyst having a Pt:Ru ratio of 1:2 with platinum deposited by $NaBH_4$ reduction. The platinum particles are poorly distributed on the CNT support and have a high tendency for agglomeration.*

Figure 10.2. *TEM image of a Pt/RuO_2/CNT catalyst prepared by $NaBH_4$ reduction having a Pt:Ru ratio of 1:0.5. The platinum particles are about 4-5 nm in size and strongly facetted.*

Figure 10.3. *Ru 3p XPS spectra for a ethylene glycol reduced Pt/RuO_2/CNT catalyst and for an as-prepared and partially reduced Pt/RuO_2 catalyst prepared by $NaBH_4$ reduction.*

Figure 10.4. *TEM image of the pure Pt/CNT catalyst showing strong preferential deposition of platinum on single tubes (left); Pt/RuO_2/CNT catalysts (Pt:Ru ratio of 2:1) with significantly more uniform dispersion of the platinum particles (right).*

Figure 10.5. *High resolution TEM image of a single carbon nano tube coated with RuO_2 and platinum (Pt:Ru ratio of 2:1). The carbon nano tube contains a large number of growth defects. The image suggests that platinum deposition occurs preferentially at defect sites.*

LEBENSLAUF

Name	Scheiba
Vorname	Frieder
Geburtstag	24.08.1977
Geburtsort	Mainz

Schulausbildung

1984-1988	Grundschule, Weiler b. Bingen
1988-1997	Stefan-George-Gymnasium, Bingen

Zivildienst

1997-1998	Landesforschungsanstalt für Wein- und Gartenbau, Geisenheim

Studium

1998-2001	Studium der Materialwissenschaft an der Technischen Universität Darmstadt
2001-2002	Austauschsemester (ERASMUS) an der École Nationale de Chimie et de Physique de Bordeaux
2002-2004	Fortsetzung des Studiums der Materialwissenschaft an der Technischen Universität Darmstadt
05/2004	Diplom-Ingenieur Materialwissenschaft
2004-2008	Wissenschaftlicher Mitarbeiter im Fachgebiet Strukturforschung (Prof. H. Fueß) und des Fachgebietes Erneuerbare Energien (Junior Prof. C. Roth) des Instituts für Materialwissenschaften der TUD

Sonstiges

06/1997	Auszeichnung des Verbandes der Chemischen Industrie als bester Chemieschüler des Abiturjahrgangs
01/1999-12/1999	Finanzvorstand bei AIESEC Darmstadt
07/2002-09/2002	Praktikum bei der Robert-Bosch GmbH, Stuttgart
10/2002-06/2003	Externer Werksstudent bei der Robert-Bosch GmbH, Stuttgart

LIST OF PUBLICATIONS

(1) F. Scheiba, N. Benker, U. Kunz, C. Roth, and H. Fuess, *Electron microscopy techniques for the analysis of the polymer electrolyte distribution in proton exchange membrane fuel cells*, Journal of Power Sources, vol. 177, **2008**, p. 273-280.

(2) F. Scheiba, M. Scholz, L. Cao, R. Schafranek, C. Roth, C. Cremers, X. Qiu, U. Stimming, and H. Fuess, *On the suitability of hydrous ruthenium oxide supports to enhance intrinsic proton conductivity in DMFC anodes*, Fuel Cells, vol. 6, **2006**, p. 439-446.

(3) L. Cao, F. Scheiba, C. Roth, F. Schweiger, C. Cremers, U. Stimming, H. Fuess, L.Q. Chen, W.T. Zhu, and X.P. Qiu, *Novel nanocomposite Pt/RuO2 center dot xH(2)O/carbon nanotube catalysts for direct methanol fuel cells*, Angewandte Chemie-International Edition, vol. 45, **2006**, p. 5315-5319.

(4) M. Michel, F. Ettingshausen, F. Scheiba, A. Wolz, and C. Roth, *Using layer-by-layer assembly of polyaniline fibers in the fast preparation of high performance fuel cell nanostructured membrane electrodes*, Physical Chemistry Chemical Physics, vol. 10, **2008**, p. 3796-3801.

(5) C. Roth, N. Benker, M. Mazurek, F. Scheiba, and H. Fuess, *Pt-Ru fuel cell catalysts subjected to H2, CO, N2 and air atmosphere: An X-ray absorption study*, Applied Catalysis a- General , vol. 319, **2007**, p. 81-90.

(6) C. Roth, N. Benker, M. Mazurek, F. Scheiba, and H. Fuess, *Development of an in-situ cell for X-ray absorption measurements during fuel cell operation*, Advanced Engineering Materials, vol. 7, **2005**, p. 952-956.

(7) I. Kinski, F. Scheiba, and R. Riedel, *Advances in Gallium Oxonitride Ceramics: A New Class of Materials in the System Ga-O-N*, Advanced Engineering Materials, vol. 7, **2005**, p. 921-927.

EIDESSTATTLICHE ERKLÄRUNG

Hiermit erkläre ich, dass ich die vorliegende Arbeit selbständig und ohne Benutzung anderer als der angegebenen Hilfsmittel angefertigt habe. Alle Stellen, die wörtlich oder sinngemäß aus veröffentlichten und nicht veröffentlichten Schriften entnommen wurden, sind als solche kenntlich gemacht. Die Arbeit ist in gleicher oder ähnlicher Form oder auszugsweise im Rahmen einer anderen Prüfung noch nicht vorgelegt worden.

(Ort und Datum) (Unterschrift des Verfassers)